Engineered microvessels for improved integration with host coronary circulation and for the generation of pre-vascularized cardiac constructs

Meredith Ann Redd

A dissertation

submitted in partial fulfillment of the

requirements for the degree of:

Doctor of Philosophy

University of Washington

2017

Reading Committee:

Dr. Ying Zheng, Chair

Dr. Charles Murry

Dr. Marta Scatena

Program Authorized to Offer Degree:

Department of Bioengineering

University of Washington

Abstract

Engineered microvessels for improved integration with host coronary circulation and for the generation of pre-vascularized cardiac constructs

Meredith Ann Redd

Chair of the Supervisory Committee:

Ying Zheng, Ph.D., Assistant Professor

Department of Bioengineering

Engineered cardiovascular tissues are at the forefront of regenerative medicine research and have the potential to redefine the treatment of heart disease in the United States and worldwide. There are many challenges associated with tissue engineering such as mimicking native structure, pre-vascularization, tissue maturation, and functional integration with the host. The following dissertation addresses many of these challenges, with a particular focus on improving vascularization methods and promoting host integration following *in vivo* transplantation. Pre-vascularization of engineered cardiac constructs is essential for the survival of the tissue, but requires precise control of structural and geometric features which is technically very challenging. Here, we engineered cardiac constructs with patterned vasculature by optimizing cardiomyocyte

culture conditions for compatibility with our previously established method to fabricate 3D perfusable microvessels in native collagen matrix. While collagen-based cardiac constructs have previously been generated in our lab and in others, we found that human stem cell derived cardiomyocytes are unable to form functional constructs in dense collagen matrix, which is required to maintain vessel patency during fabrication. However, when co-cultured with matrix-remodeling stromal cells, we observed synchronous electrical wave propagation, force generating contractions, and markedly improved cellular maturation as well as uniaxial alignment. With these co-culture conditions in dense collagen, we were able to incorporate patterned endothelialized channels and generated pre-vascularized cardiac tissue constructs. This work represented an important achievement, but looking forward, tissue engineering strategies will ultimately require efficient host integration to have therapeutic success. Additionally, the ability to generate all of the required cell types (i.e. cardiomyocytes, stromal cells, and endothelial cells) from a single cell source would be more suitable for clinical applications by enabling patient-specific or autologous construct formation with human induced pluripotent stem cell technology. Towards this end, we generated human stem cell derived endothelial cells (hESC-ECs) and characterized them both *in vitro* and *in vivo*. hESC-ECs were used to make engineered microvessels and were found to retain structural and functional characteristics of mature endothelial cells, including patent lumen formation with intact junctions and non-thrombogenic blood interactions. To determine whether our pre-patterned and perfusable hESC-EC vascular networks were able to improve host integration following *in vivo* implantation, we developed a novel method to image vascular perfusion *ex vivo* of grafts implanted on

injured rat myocardium for five days. Compared to unpatterned controls, patterned vascular networks showed improved vascular perfusion dynamics with flow velocities comparable to those in healthy myocardial regions. To our knowledge, this was the first demonstration of improved graft perfusion through the use of patterned vasculature in the heart. Taken together, this research demonstrated the successful use of a patterned vascular system for the generation of pre-vascularized cardiac constructs and for improved graft perfusion dynamics. Collectively, this work has many implications in the field of cardiovascular tissue engineering with particular regard to maintaining cardiac structure during vascular incorporation, host integration strategies, and perfusion assessment methods.

Table of Contents

List of Figures

Acknowledgements

Chapter 1.

Introduction

The field of cardiovascular tissue engineering aims to address the burgeoning health problem of heart failure which continues to be the leading cause of death worldwide. Over the years, significant technological advancements have been made towards understanding how to culture heart muscle cells (cardiomyocytes) in 3D to generate contractile tissues with the potential to replace damaged heart muscle. The therapeutic application of engineered cardiac tissues, however, remains out of reach due to the challenging nature of reproducing the complex structure and function of the heart in a dish. In addition to the organization and electromechanical integration of cardiomyocytes, incorporation of a functional vascular component is essential but has proven to be quite challenging, due in part to fabrication limitations as well an incomplete understanding of the biochemical cues and physical forces that guide vascular development. The following introduction reviews the structure, function, and developmental origins of the coronary vasculature and associated endothelial cells followed by a review of ischemic heart disease, current myocardial regenerative approaches, and tissue vascularization techniques.

1.1 *Coronary Vasculature*

The heart is one of the most metabolically demanding organs in the body [1] and as such contains an extensive vascular network to maintain its viability. Nearly every heart muscle cell (cardiomyocyte) is in direct contact with one or more capillaries in order to provide sufficient oxygen and nutrients [2,3]. In fact, the number of endothelial cells in the

native myocardium outnumbers cardiomyocytes three to one [4]. The myocardium itself is highly organized with dense unidirectional myofibril alignment and correspondingly dense vasculature that parallels the alignment within the myocardium (Fig 1.1) [2]. This structure is essential to sustain the heart muscle, which must pump continuously throughout a lifetime. Coronary physiology and pathophysiology has substantial impact on myocardial function during development and in the adult heart, and is therefore an essential aspect of heart disease and heart regeneration that must be considered.

The coronary vasculature is a network of arteries, capillaries, and veins that provides direct nutrient and oxygen supply to the myocardium. Coronaries originate from the root of the aorta and branch into two main conduits, the right coronary artery and the left coronary artery [5]. Additional branches extend from these main arteries and fully encompass the left and right epicardial surfaces, while further subdivisions into major arteries and expansive capillary beds penetrate the myocardium and flank nearly every myocyte within the compact ventricles [5]. Venous return of deoxygenated blood occurs through coronary veins that collectively merge into the coronary sinus which then
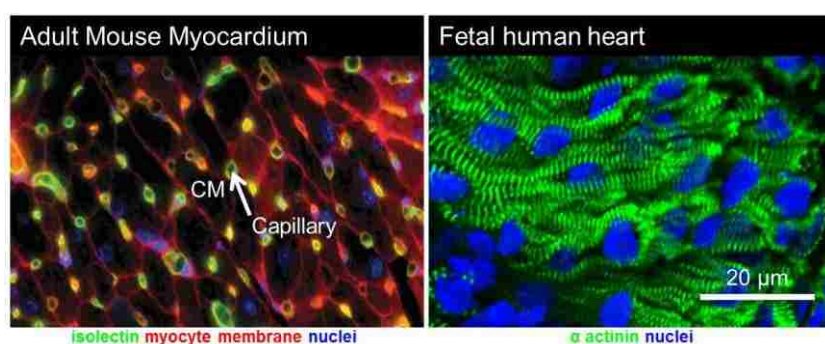
Figure 1.1 – Myocardial structure and coronary vasculature. Left: Adapted from Hsieh et, al. *Ann Rev Physio* 2006 [2]. Right: Immunofluorescent confocal image of fetal human heart.

returns blood directly to the right atrium [5]. The precise patterning and hierarchical division of coronary vessels is a fundamental event that occurs during embryonic development of the heart [5]. Although there is considerable variation in the exact

structure and pattern of the coronary arteries within the human population, misregulation during development that leads to improper coronary vessel formation and patterning has vast implications in myocardial structure and function [5]. While vasculogenic mechanisms and their driving signaling pathways in other developing organs have been extensively studied, the origins of coronary vessels and the mechanisms driving their specification and patterning remain to be fully elucidated with much associated debate and controversy.

Lineage tracing experiments in mice embryos and in chick-quail chimera embryos established the view that coronary arteries arise from migrating epicardial cells that undergo epicardial to mesenchyme transition (EMT), and later differentiate into vascular endothelial cells, smooth muscle cells, and fibroblasts [6–9]. Mesoderm derived epithelial cells that originate from the proepicardial organ, an outgrowth of the dorsal body wall independent of the primitive looped heart tube, are thought to migrate towards and encompass the heart forming a primitive epicardium, or proepicardium [10]. A subset of these epithelial cells migrates into the subepicardial space and undergoes EMT [6,7,11]. This newly formed population of mesenchyme cells is thought to then migrate into the myocardium and differentiate into vascular endothelial cells which undergo de novo lumen formation and assemble into large coronary arteries as well as a subepicardial capillary plexus [5,6]. Extensive remodeling of these epithelial-derived coronary vessels continues throughout development, and the final connection between the coronary endothelium and the aorta is thought to occur via vessel growth towards the aorta accompanied by local apoptotic events that finally establishes a connection with systemic circulation [12]. This model leads to several interesting lines of questioning. The

first is how the coronary arteries and veins assemble in such a way that they are adjacent to each other, yet connect to systemic circulation in different areas: the arteries at the base of the aorta and the veins at the right atrium. The second is how fate specification of the mesenchymal derived cells in the heart is determined prior to migration from the epicardium.

A more recent study suggests that rather than epicardial origins, the coronary arteries may primarily arise from dedifferentiated venous endothelial cells that sprout and migrate from the sinous venous of the primitive heart tube towards the myocardium, and secondarily from blood islands that bud into the myocardium from the endocardium and later connect with the newly formed coronary plexus [13,14]. Coronary arteries derived from the sinous venous could help explain how the final venous connection to systemic circulation is established since the sinous venous later gives rise to the coronary sinus, the main conduit in charge of venous return to the right atrium. Despite these conflicting theories, there is a large body of literature with multiple lineage-tracing studies that points towards epicardial origins of the coronary arteries. Furthermore, epicardial failure to undergo EMT results in no coronary artery formation [15]. However, additional studies have shown that failure to initiate vascular smooth muscle cell differention leads to defects in coronary vessels presumably due to a lack of vessel stabilization resulting in regression [16]. It is therefore possible, that epicardial migration followed by EMT is required for stabilizing the newly formed coronary vessels, but the endothelial cells themselves may not originate from the same epithelial lineage. To further confound the development mysteries of the coronary vascular system, vascular mural cells and endothelial cells typically originate from distinct lineages, but recent evidence suggests

that endocardial ECs in the developing myocardium may contribute to the rise of a subset of PDGFβ+ mural cells [17] suggesting that at least in some cases, the plasticity between cell fate and developmental origin may be more complex than originally believed. The discrepancy and remaining ambiguity regarding the origins of the endothelial cells that make up the coronary vasculature will likely be resolved with additional fate mapping and lineage tracing experiments in a variety of model systems. In the mean-time, these lineage tracing studies have implications in the field of heart regeneration. Namely, the development of better differentiation protocols to generate distinct cell types and the ability to stimulate both myocyte proliferation and vascular growth and stabilization would improve our understanding of myocardial development and help guide vascular regeneration strategies.

1.2 *Endothelial Cells: Pathophysiology and Response to Shear Stress*

The endothelial cells that line the inner lumens of the entire cardiovascular system form a single cell barrier that under quiescent conditions is largely non-thrombogenic and non-adhesive for the macromolecules and cellular components of the blood [18]. The endothelium contains lateral cell-cell junctions, such as VE-cadherin, PECAM, Claudin-5, ZO1, etc. that function to modulate cell adhesion and permeability [19]. Additional vascular adhesion complexes are located on the luminal and basal endothelial cell surfaces and function to structurally stabilize the vascular lining as well as control the adhesion of circulating leukocytes and platelets [18]. The expression, regulation, and function of both endothelial junction proteins and vascular adhesion molecules are highly dependent on the activation state of the endothelium.

A quiescent endothelium is characterized by internalized Von Willebrand Factor stored in Weibel-Palade bodies [20], sustained NO production and release [21], contact inhibited growth [19], and intact junctional complexes [22]. Endothelial activation, however, is characterized by release of VWF granules [20], disorganized junctions [22], reduced NO bioavailability [23], and increased reactive oxygen signaling [24]. These changes typically result in increased endothelial proliferation and migration as well as thrombosis and activation of inflammatory pathways. Physiologically, an activated endothelium is often found at sites of angiogenesis, atherosclerotic lesions, regions of inflammation, and in other vascular diseases [18]. Furthermore, in an activated state, increased expression of endothelial adhesion molecules such as P-selectin, E-selectin, ICAM-1, and VCAM-1 as well as increased expression of chemoattractants such as IL-8 and MCP-1 leads to greater leukocyte recruitment and increased transluminal migration towards sites of inflammation [22,25–27]. The mechanisms regulating the activation of these genes can be broken up into two main categories: humoral factors (cytokines and bacterial endotoxins), and biomechanical forces (shear stress, cyclic strain, and hydrostatic pressure) [18]. Although the key players, and signaling pathways involved in endothelial activation are becoming clearer, a better understanding of the interplay between pathways remains to be fully understood and could have vast implications in the study and treatment of vascular diseases.

One of the most important aspects of endothelial biology and vascular engineering is the study of how endothelial cells respond to biomechanical forces. Endothelial cells are in direct contact with blood flow at all levels of the vascular hierarchy and respond directly to changes in hemodynamic forces in order to regulate

vascular tone, platelet adhesion, and other signaling mechanisms that govern tissue responses to increased flow [28,29]. A fundamental understanding of fluid shear stress is therefore important when discussing the cardiovascular system. In most regions of the vasculature, blood flow can be approximated as steady incompressible laminar flow through a circular tube, more commonly known as Poiseuille flow. Although Poiseulle fluid dynamics is often used to describe blood flow, it is important to keep in mind several distinctions that make the mechanics of blood flow slightly more complex: (1) blood is a non-Newtonian fluid, (2) flow is pulsatile in many regions of the vasculature, and (3) the vessel wall is compliant [30]. The following equations are adequate approximations for regions where blood flow resembles steady continuous flow through a cylindrical pipe. However, regions with slow flow, bifurcations, or arches have more complex fluid profiles and typically require numerical analysis and modeling to evaluate flow and the resulting shear stresses. Nevertheless, if we assume Poiseuille flow, the Navier-Stocks equation to describe the motion of fluid reduces to a form that has a solution (eq. 1) [31].

(1) $\frac{\delta P}{\delta z} = \mu \left[\frac{1}{r} \frac{\delta}{\delta r} \left(r \frac{\delta v_z}{\delta r} \right) \right]$

Solving this equation yields a velocity profile that is parabolic with the maximum velocity located at the center of the vessel, and a velocity of zero at the wall. This zero wall velocity is referred to as the no slip condition which creates a frictional force between the fluid and the wall known as shear stress [31]. The magnitude of fluid shear stress is linearly proportional to the velocity gradient and can further be derived from Poiseuille's Law (eq. 2) where τ_s is the frictional force per unit area on the inner vessel wall, μ is the blood viscosity, Q is the volumetric blood flow rate, and R is the radius of the vessel [32].

(2) $\tau_s = \frac{4\mu Q}{\pi R^3}$

By the time blood flow reaches the microcirculation, pulsatile flow is thought to generally dampen out, however pulsatile flow is still observed in capillaries in some situations [33]. In the heart, the physical contraction of the myocardium during systole compresses the coronary vessels and blood flow is restricted. Instead, most coronary flow occurs during diastole as the heart relaxes and blood vessels are allowed to dilate [34]. Throughout the cardiovascular system, the magnitude of wall shear stress varies depending on the hierarchical location within the vascular tree. Veins, for example, are exposed to minimal shear on the order of 1-6 dynes/cm^2, while a normal artery may experience anywhere from 10 - 70 dynes/cm^2 [32]. Maintaining these physiological shear stress levels is essential for endothelial quiescence. Arteries subjected to low shear (< 4 dynes/cm^2) with separated and disturbed flow have long been associated with atherosclerosis through the creation of lesion prone arterial regions, while sustained arterial shear greater than 15 dynes/cm^2 has been shown to induce endothelial quiescence and the expression of atheroprotective genes [32,35].

Progress has been made towards understanding how fluid forces elicit endothelial responses, but the exact biomechanical mechanisms remain to be fully understood. There is some evidence that membrane bound endothelial proteins, such as VEGFR2, PECAM-1, and VE-cadherin, comprise a mechanosensory complex that initiates endothelial signaling cascades through PECAM-1 mediated tension on the cytoskeleton during exposure to fluid shear stress [36]. Sensing mechanisms such as these ultimately result in modified expression of a number of key endothelial genes that govern vascular homeostasis, endothelial-pericyte interactions, and tissue-specific cross-talk [37]. More

recently, it was discovered that different endothelial cells throughout the body (e.g. human umbilical vein endothelial cells vs. lymphatic endothelial cells) respond optimally at different levels of shear stress which correlate to the physiological levels of fluid shear that they are exposed to *in vivo* [38,39]. The expression of key endothelial genes, such as VEGFR3 [39], as well as specific signaling pathways, such as Wnt signaling [40], have been shown to modulate endothelial sensitivity to flow and may play a role in determining the optimal level of shear for a given endothelial population.

Endothelial response to shear is essential for maintaining a quiescent endothelium and facilitating normal healthy responses to physiological stimuli. In pathological conditions, endothelial dysfunction is associated with increased inflammation, thrombosis, and the development of atherosclerotic plaques. In addition to complications associated with vascular disease, the development of atherosclerotic lesions poses an additional threat in the form of increased risk of stroke or heart attack.

1.3 *Ischemic Heart Disease and Regenerative Medicine*

Cardiovascular disease is the leading cause of morbidity and death worldwide with coronary heart disease and ischemia accounting for the majority of cases [41]. With the exception of whole heart transplantation for which there is stunning lack of available donor hearts, current treatments are only palliative. Many are able to slow the progression of the disease and improve patient quality of life, but none are able to completely restore function and prevent heart failure. As the prevalence of heart failure continues to rise and the supply of donor hearts for transplantation remains infrequent, there is a burgeoning clinical need for new and innovative approaches [42]. A myocardial

Infarction (MI) is caused by a blockage in one or more of the coronary arteries resulting in temporary occlusion of the blood flow to downstream regions of the myocardium [43]. During an event such as this, up to 25% of cardiomyocytes, the force generating cell in the heart, may die [44]. Cell death in conjunction with substantial vascular death [45] results in a highly ischemic and necrotic region that promotes myofibroblast differentiation and ECM production [46]. Initial ECM synthesis and remodeling helps stabilize the infarct and prevents ventricular dilation, but the lingering persistence of the myofibroblast in the infarct results in adverse remodeling that limits the ability of the region to heal and functionally recover. Indeed, within two weeks following an MI injury, much of the healthy myocardial muscle is replaced by collagenous scar tissue that results in an increase in stiffness, thinning of the left ventricular wall, and an overall decline in both systolic and diastolic function (Fig 1.2) [45].
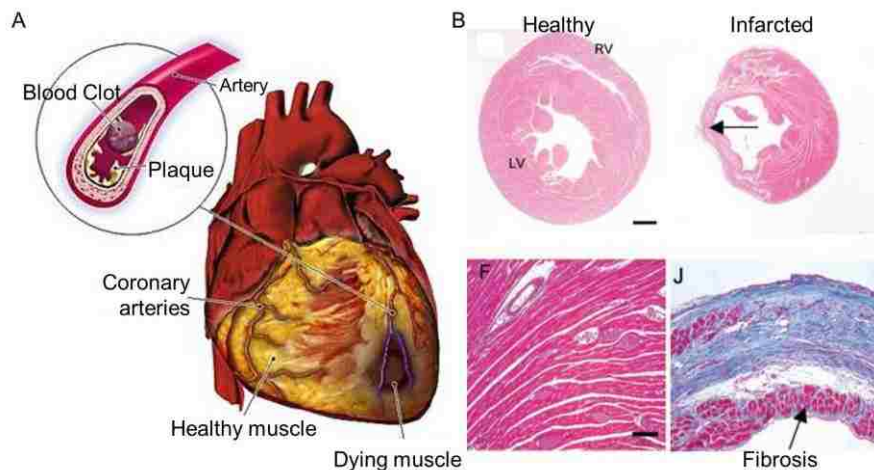
Figure 1.2 – Myocardial infarction and pathological remodeling. (A) Graphic of ischemic heart disease (B) Histological sections of healthy and 4 weeks post infarction. Adapted from Virag et. al. *Am J Path* 2003 [45]

Cell-based therapies for the treatment of MI have emerged as promising methods to replace damaged myocardium with healthy, viable tissue [44,47]. Clinical trials that delivered cell types such as endothelial progenitor cells (EPCs) [48,49], bone marrow

derived mononuclear stem cells (BMMNCs) [50,51], and skeletal myoblasts [52,53] have demonstrated safety and feasibility of cell transplantation although the benefits observed in these studies are now widely attributed to paracrine mechanisms that reduce inflammation, increase proliferation, and stimulate angiogenesis rather than truly regenerating the myocardium [54]. Cell transplantation studies with human stem cell derived cardiomyocytes, however, have the potential to physically remuscularize the heart. Transplantation in infarcted murine hearts has shown considerable engraftment, electrical coupling with the host myocardium, and modest functional improvement [55–58]. Furthermore, our lab recently demonstrated substantial remuscularization of infarcted non-human primate hearts with intramyocardial delivery of stem cell derived cardiomyocytes [59]. Despite seminal gains towards pushing stem cell derived cardiomyocytes towards the clinic, these studies bring to light key outstanding challenges that remain and must be addressed.

Complete functional recovery following transplantation with stem cell derived cardiomyocytes has yet to be achieved. Despite encouraging progress, limitations persist such as inadequate contractile and electrical maturation of the cells as well as poor survival and long term retention of transplanted cells [44]. Studies have shown that greater than 50% of administered cells are lost within the first day, and by week 12, cell survival is down to around 15% [60]. While pro-survival techniques such as heat shock the day before implantation can lessen this loss [61], retention is still a major issue.

Cardiomyocytes differentiated from embryonic stem cells (ESCs) or induced pluripotent stem cells (iPSCs) exhibit immature pro-arrhythmic electro-physiological properties [62] and inadequate structural assembly of contractile machinery [63]. Recent *in*

vitro experiments have demonstrated that the electrical and structural maturation of cardiomyocytes can be promoted in 2D culture with the presence of non-myocytes [64], long term culture [65], and increased substrate stiffness [66]. Similar improved maturation can be achieved by culturing cardiomyocytes in three dimensional engineered tissues [67]. Microarray analysis of cardiomyocytes showed that cells cultured in 3D obtained a more physiologically mature and ventricular-like phenotype compared to 2D culture [68]. Thus, cardiac tissue engineering has drawn considerable research interest as a promising approach for heart regeneration.

1.4 *Cardiac Tissue Engineering*

An organized scaffold pre-cultured with cells *in vitro* has the potential to structurally and functionally mature the tissue prior to implantation and to improve graft retention after transplantation. A seminal study by Eschenhagen and Zimmermann generated engineered heart tissue with neonatal rat cardiomyocytes in type I collagen gel, and found that after one to two weeks in culture, these constructs were synchronously and rhythmically contracting [69]. Since then, our lab and others have successfully generated contractile cardiac tissues from stem cell derived cardiomyocytes in a variety of scaffolding materials such as collagen, fibrin, and synthetic biodegradable polymers [70–72]. Furthermore, *in vitro* culture of these tissues with physiological external forces can be used to increase construct maturation. For example, mechanical stimulation with cyclic stress applied to engineered cardiac constructs has been shown to induce cardiomyocyte alignment, improve electrophysiological properties, and increase force production [70,73]. Similarly, electrical stimulation of constructs generated with stem cell

derived cardiomyocyte leads to increased myofibril organization and faster conduction velocity [74,75]. Taken together, these studies demonstrate the importance of applying physiological cues to promote adequate structural and functional maturation of the tissue.

As tissue engineering approaches become more sophisticated, the challenge will be to integrate all the necessary components and stimuli into one package capable of achieving structural alignment, synchronous electrical activation, and contractile force generation. Furthermore, the aforementioned studies are limited to generating constructs on the order of 50 to 200 µm thick due to diffusion limitations through the tissue [69]. Capillary structure is vital for the survival and function of metabolically active cardiomyocytes. In the adult heart, capillaries are spaced every 20 µm to provide nutrients and oxygen to each cardiomyocyte [76]. Thus, vascular incorporation is vital for the survival of engineered cardiac tissue *in vitro* and for systemic integration with the host upon implantation. Despite this major need, vascularization with high capillary density and interconnected perfusable lumens has not been achieved.

1.5 *Tissue Vascularization and Engineered Microvessels*

Over the last decade, it has become relatively commonplace to generate cardiac tissues with vascular structures by combining multiple cell types within the tissue scaffold. Specifically, the combination of myocytes, endothelial cells, and mural support cells such as mesenchymal stem cells or fibroblasts results in the formation of *de novo* lumens *in vitro* as well as modest incorporation with host vasculature *in vivo* [70,77–80]. The formation of vascular structures and integration with the host has been further

improved by tuning additional construct properties, such as matrix composition [81,82], geometric pore design [83], release of biochemical factors [84–86], microchannels for guided tubulogenesis [74,87,88] and interstitial pressure gradients [89]. Nonetheless, these methods continue to rely on the self-assembly of endothelial cells into lumens which lack interconnectivity or a hierarchical branching architecture. These methods are therefore unlikely to provide sufficient blood flow to the graft without additional patterning or substantial arteriogenesis and remodeling.

The incorporation of perfusable vascular structures in engineered cardiac grafts is a challenging endeavor that requires precise control of structural and geometric features. These vascular structures must support nutrient permeability into the bulk matrix of the construct, while maintaining physiological endothelial function. In addition to supplying nutrients, endothelial networks initiate a variety of signaling cascades important for normal cardiac development and function through dynamic gene expression profiles. Endothelial derived factors, such as neuregulin [92,93], nitric oxide synthase (eNOS) [94], endothelin [95,96], PDGF [97], and transcription factor KLF2 [90,91] are known to play important roles in the interactions between endothelial cells and cardiomyocytes. Exposure to these factors has been shown to influence cardiomyocyte development and maturation [90,91], proliferation [92], survival [92,97], force generation [95], and even sub-type specification [93]. In native tissue, the endothelium is constantly exposed to changes in blood flow to which it responds by modulating gene expression and factor secretion through shear responsive pathways [28,98]. Ideal approaches for tissue vascularization will therefore be able to recapitulate the hemodynamic environment of the coronary vasculature while still maintaining characteristics that are essential for

myocardial function: matrix stiffness, myofibril maturation and alignment, electrical propagation, and force generation. For this goal to be realized, methods must be established to promote the precise control of vascular structure formation and patterning during construct formation.
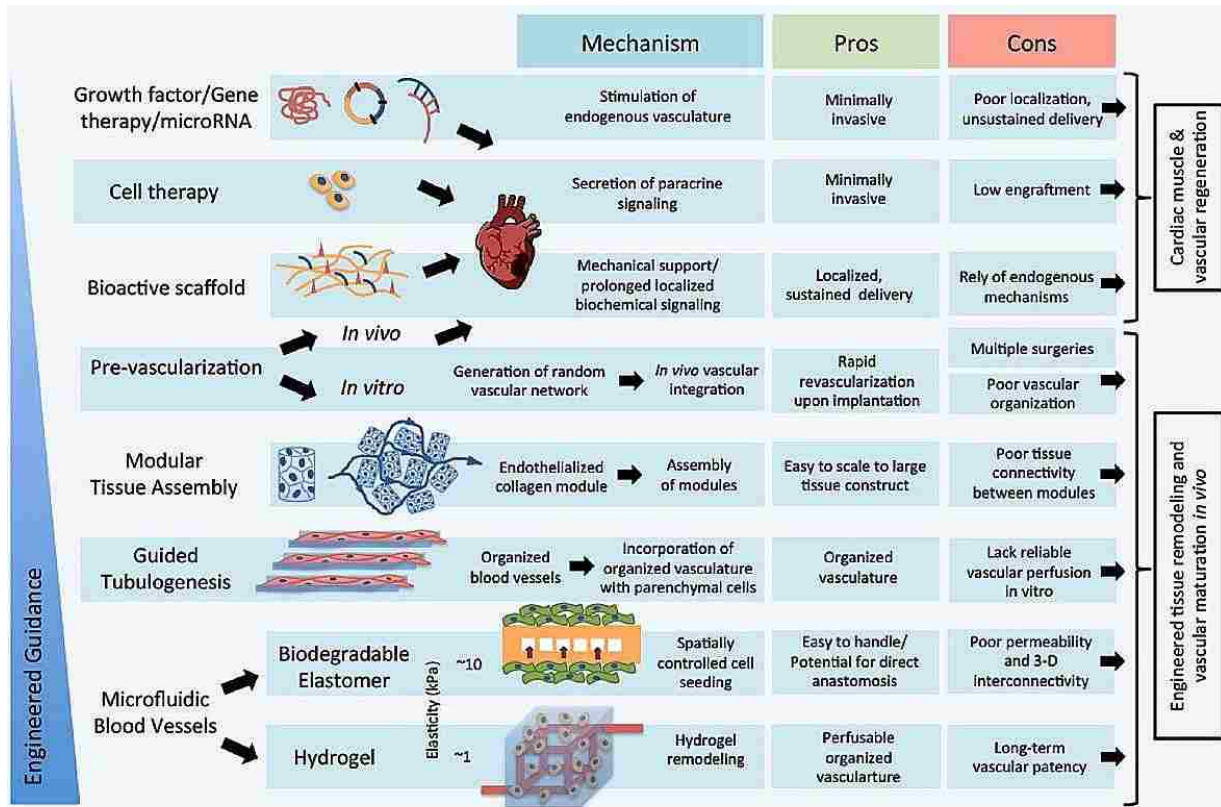
Figure 1.3 – Pre-vascularization strategies in cardiac tissue engineering. Adapted from Montgomery et. al. *J Cardiovasc Pharmacol Ther* 2014 [101].

Approaches that generate sacrificial vascular templates by utilizing 3D printed networks [99], or aligned and branched alginate fibers [100] have been employed to achieve structural control of micro-features within hydrogels. The 3D printed approach patterned carbohydrate glass layer by layer into a three dimensional interconnected structure and

then embedded the network within a hydrogel matrix. Once the printed network was dissolved away, endothelial cells were seeded through the network which led to the creation of perfusable vasculature structures [99]. A similar sacrificial casting approach was employed with alginate fibers to generate branched microvessels, but this technique was limited to 2D planar structures [100]. Figure 1.3 provides an overview on common vascularization strategies. As vascular engineering techniques such as these emerge, the challenge becomes how to incorporate these strategies with the inclusion of parenchyma cells, such as cardiomyocytes or cardiac engineering. Gel remodeling must occur during construct fabrication for cardiomyocytes to be able to establish necessary cell-cell contacts, but this process often destroys the fabricated channel structure preventing the formation of vascular structures [101]. For cardiac tissue vascularization to be achieved, we must develop strategies that promote the formation of compact cardiac tissue with synchronous contractions while maintaining the integrity and structure of patterned vasculature.

Our lab has developed a vascular engineering strategy to form micro-templated engineered microvessels in native dense type I collagen [102,103]. Engineered microvessels are fabricated with a two-step injection molding technique that utilizes patterned microfabricated wafers generated with standard soft lithography methods (Fig 1.4). Microvessels generated in this way have endothelialized 3D luminal geometry, defined network structure, the capacity for multi-cellular proximity, and are fully perfusable with the ability to sustain constant laminar flow. We have previously demonstrated that engineered microvessels display important physiologic behaviors. The endothelium are generally quiescent and do not initiate clot formation unless

exposed to endothelial activation factors such as phorbol-12-myrisate-13-acetate (PMA) [102]. Endothelial cells in this system form stable PECAM-1 (CD31) and VE-cadherin junctions and undergo angiogenesis when exposed to the appropriate stimuli. Furthermore, the incorporation of additional cell types within the interstitial collagen is easily achieved enabling the study of multi-cellular interactions with the patterned vasculature [102,104,105].
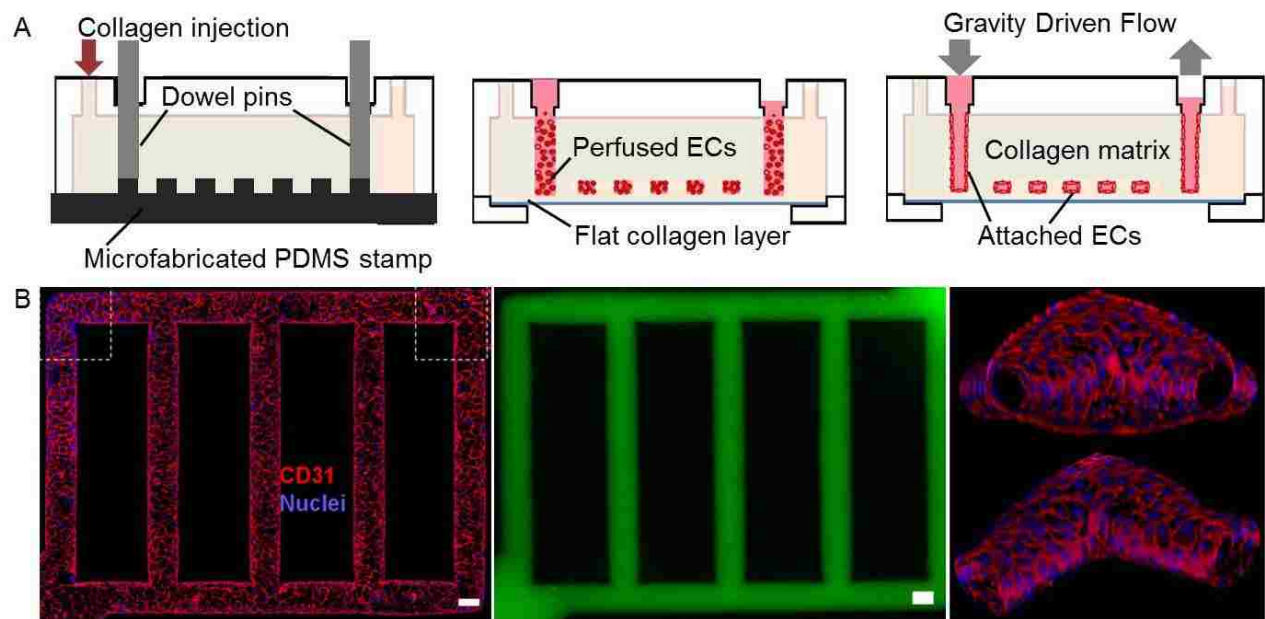
Figure 1.4 – Engineered microvessels: fabrication and characterization. (A) Schematic of injection molding process to generate patterned microvessels. (B) (Left) Lumen formation with PECAM-1/CD31 junctions (red). (Middle) Fluorescent dextran perfusion. (Right) 3D view to demonstrate patency. Adapted from Zheng et. al. *PNAS* 2012 [102]

1.6 *Host Integration and Assessing Vascular Perfusion*

The incorporation of patterned vasculature is essential for the future success of engineered cardiac tissues. In addition to supporting viability *in vitro*, vascular

integration with host myocardium must be achieved to maintain tissue viability post implantation. The tri-cell seeded constructs mentioned in the previous section have been shown to connect with host vasculature in the heart after 1-2 weeks of implantation [70,72]. To promote faster integration, prior organization of endothelial cells has been shown to lead to blood flow at early as 3 and 5 days post implantation [87], and prior organization combined with direct anastomosis resulted in immediate perfusion of the engineered vasculature   [106]. The benefit of organized vasculature and direct anastomosis has yet to be tested in the heart, however, which may present additional technical complications due to the size scale of the arteries available for surgical connection and the beating motion of the heart. Thus far, the extent of integration between the host and engineered vasculature has primarily been assessed through histological means such as the detection of vessels containing red blood cells and intravenous perfusion of lectins, or with non-quantitative blood flow imaging methods. While informative, these approaches are not able to assess the dynamics of blood flow or distinguish the source of vascular infiltration (i.e. myocardial vs. other surrounding tissue such as chest wall adhesions) [72,107]. To more accurately assess integration between grafts and myocardial-originating vessels, a recent study used retrograde aortic perfusion of lectins to visualize vessels and found that tri-cell seeded grafts were poorly perfused from the myocardium after one week (Fig 1.5A) [107]. Moving forward, it will be necessary to measure flow rate to ensure vascular function is achieved.

Optical coherence tomography (OCT) has emerged as a useful tool both in research applications and in the clinic to visualize vascular flow. Clinically, it is commonly used as an invasive method to obtain intracoronary images of vascular

stenosis, stent placement, neointimal thickening, etc. [108], while research labs have adapted the technology to obtain high resolution 2D scans of vasculature in tissues such as the eye (Fig 1.5B) [109], the brain [110], and skin [111]. More recent advances in the technology and data processing algorithms were able to extract relative flux information from the OCT angiograms [112]. Other vascular imaging techniques such as ultrasound microbubbles [113] and micro-computed tomography (μ-CT) [114] have been used to image vasculature but are limited by poor resolution of the microcirculation. As more advanced methods to generate pre-vascularized tissues emerge, it is clear that better, more quantitative methods to assess vascular function will be necessary to determine the relative efficacy of each approach.
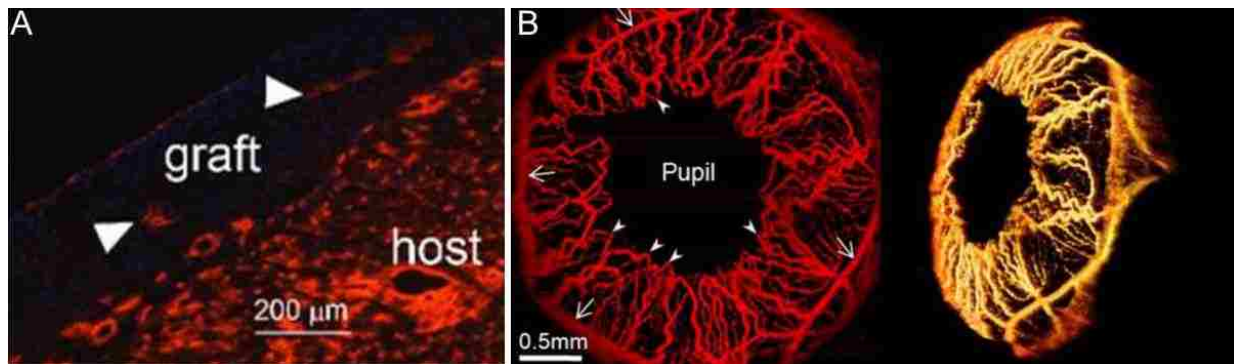
Figure 1.5. Vascular perfusion imaging. (A) Confocal image adapted from Coulombe et. al. *IEEE* 2014 of retrograde lectin perfusion [107]. (B) Example of OCT angiogram projection (left) and 3D view (right) of mouse eye. Image adapted from Choi et. al. *Optics Letter* 2014 [109]

1.7 *Dissertation Overview and Significance*

The research presented in this dissertation sought to address the challenges described throughout Chapter 1 and improve vascular engineering strategies in the context of engineered cardiac tissues and host integration. Chapters 2 through 4 describe the rationale, scientific methods, and results of the following three specific aims:

AIM 1: The design and optimization of pre-vascularized biomimetic cardiac tissues through the incorporation of stromal cells in dense collagen (chapter 2).

AIM 2: Characterization of stem cell-derived endothelial cells as a vascular cell source for regenerative therapies (chapter 3).

AIM 3: Host integration of patterned vasculature with real time assessment of vascular perfusion using optical microangiography (OMAG) (chapter 4).

The work contained in the following three chapters has many implications to the field of cardiac regeneration and vascular integration. The results of aim 1 provided insight into the required cellular and matrix conditions for cardiac remodeling to occur. Our findings could help guide future studies in disease modeling, such as the study of myocardial responses to adverse remodeling and fibrosis. Furthermore, the ability to incorporate microstructures in cardiac constructs using dense collagen matrix will enable more precise control of structural features for future pre-vascularization techniques. In addition to providing vascular templates, better control of structural features could be used for other applications such as embedding patterned micro- or nanogrooves in 3D that could be used to induce alignment. Our results detailed in aim 2 provide functional

evidence that endothelial cells differentiated from stem cells are a viable vascular cell source. In addition to their ability to form highly vascularized constructs, the use of these cells in conjunction with stem cell derived cardiomyocytes could be used to generate pre-vascularized tissue constructs made entirely from an autologous cell source with induced pluripotent stem cell technology. The results presented in aim 3 represent, to our knowledge, the first real-time evaluation of *in vivo* integration and perfusion of patterned vasculature in the context of myocardial disease. This work represents seminal progress for the advancement of engineered myocardial tissue towards clinical applications.

Chapter 2.

The design and optimization of pre-vascularized biomimetic cardiac tissue through the incorporation of stromal cells in dense collagen

This chapter has been published in the following manuscript: [105]

Note: maiden name – Roberts

- **Roberts, M.A.**, et. al. Stromal Cells in Dense Collagen Promote Cardiomyoctye and Microvascular Patterning in Engineered Human Heart Tissue (2016). *Tissue Engineering: Part A* 22(7-8): 633-644. PMID: 26955856.

2.1 Abstract

Current cardiac and vascular engineering approaches independently create aligned contractile tissue or perfusable vasculature, but a combined vascularized cardiac tissue remains to be achieved. In this aim, we sought to incorporate a patterned microvasculature into engineered heart tissue, which balances the competing demands from cardiomyocytes to contract the matrix versus the vascular lumens that need structural support. Low density collagen hydrogels (1.25 mg/ml) permit human embryonic stem cell-derived cardiomyocytes (hESC-CMs) to form a dense contractile tissue but cannot support a patterned microvasculature. Conversely, high collagen concentrations (density ≥ 6 mg/mL) support a patterned microvasculature, but the hESC-CMs lack cell-cell contact, limiting their electrical communication, structural maturation, and tissue-level contractile function. When co-cultured with matrix-

remodeling stromal cells, however, hESC-CMs structurally mature and form anisotropic constructs in high density collagen. Remodeling requires the stromal cells to be in close proximity with hESC-CMs. Additionally, co-cultured cardiac constructs in dense collagen generate measurable active contractions (on the order of 0.1 mN/mm^2) and can be paced up to 2 Hz. Patterned microvascular networks in these high-density co-cultured cardiac constructs remain patent through two weeks of culture, and hESC-CMs show electrical synchronization. The ability to maintain microstructural control within engineered heart tissue enables generation of more complex features, such as cellular alignment and a vasculature. Successful incorporation of these features paves the way for the use of large scale engineered tissues for myocardial regeneration and cardiac disease modeling.

2.2 Rationale

Transplantation with human stem cell derived cardiomyocytes (hESC-CM) has shown promise in a number of animal models to regenerate and remuscularize damaged heart tissue [55,59,71,115,116]. The tissue engineering approach has also drawn substantial research interest because three-dimensional structural control and tissue maturation prior to implantation is possible [117]. Many groups have had considerable success forming contractile cardiac constructs within native soft biological hydrogels, such as fibrin [118,119], collagen [70,120,121], and decellularized heart matrix [122], as well as in scaffold free conditions [80,123]. Engineering large scale cardiac tissues, however, continues to be hindered by a lack of vasculature and poor structural and functional maturation of stem cell-derived cardiomyocytes.

Vasculature and blood flow are critical in not only supplying nutrients and oxygen, but also in modulating cardiomyocyte maturation [94], subtype specification [93], and ischemic protection [92]. In engineered cardiac tissues, vascular structures have been generated by combining myocytes, endothelial cells, and a mural cell population, such as mesenchymal stem cells or fibroblasts [70,80,123]. Under these conditions, *de novo* lumens and cord-like structures form and integrate to some degree with host circulation when implanted [78–80]. These "tri-cellular" constructs were further shown to have increased active twitch force [124] suggesting the importance of paracrine signals from non-myocytes. Despite these advancements, the vascular structures that are formed from this type of approach continue to lack an orderly branching hierarchy, and graft-host integration is slow relative to the immediate perfusion needs of the construct [101,107]. An ideal construct would have both perfusable vasculature that recapitulates the hemodynamic environment of coronary vessels and appropriate characteristics for myocardial function such as a compliance-matched matrix, myofibril maturation and alignment, electrical propagation, and force generation.

In this aim, we developed a cardiac tissue construct that has sufficient mechanical strength to support fabrication and patency of a perfusable vascular network, and optimized cellular composition to promote cardiomyocyte survival, organization, and maturation. We showed that although dense collagen (≥ 6 mg/mL) is required for microchannel fabrication, it does not support cardiomyocyte structure and function. We demonstrated that co-culturing with a stromal cell population promoted matrix remodeling and cardiomyocyte alignment, and allowed for the formation of a functional vascularized cardiac tissue in dense collagen. Our work represents an important step

towards generating perfusable vascularized cardiac tissues *in vitro*, and suggests a key role for stromal cells in matrix organization and cardiac maturation.

2.3 Scientific Methods

2.3.1 Cell Culture

Spontaneously beating cardiomyocytes (SV1) were generated from high density monolayers of RUES2 human embryonic stem cells (hESCs) using a combination of activin A, BMP4 and small molecule Wnt activation/inhibition as described previously [115] and in Appendix A. For a subset of experiments, cardiomyocytes were generated from transgenic RUES2 hESCs that constitutively express GCaMP3, a fluorescent calcium reporter. ZFN-mediated targeting was used to construct this line as previously described [116]. Cardiomyocyte cultures averaged 64.1 ± 19.3% cardiac troponin T (cTnT) positive by flow cytometry, and this preparation is referred to as "cardiomyocytes" or hESC-CM throughout the manuscript. Four different stromal cells were used in this study, including two human bone marrow derived stromal cell lines (HS27a and HS5) [125], human dermal fibroblasts (Lonza), and primarily isolated human fetal heart perivascular cells. See Appendix A additional methods for more detail on cardiomyocyte differentiation and stromal cell culture.

2.3.2 Cardiac construct formation and culture

Tissue molds were fabricated via molding of uncured polydimethylsiloxane (PDMS) (Dow Corning Sylgard 184 silicone elastomer) into a laser-etched acrylic negative template with 17 x 3 mm wells containing 1 mm diameter posts at each end to provide

uniaxial strain (Fig 2.1A). The molded PDMS was baked at 65°C for at least one hour and then peeled away for autoclave sterilization. Immediately prior to construct formation, the PDMS wells were treated with a hand held corona treater (Electrotechnic Products, Inc., BD-20) to make surfaces hydrophilic. Cells were mixed with pre-neutralized collagen gel (2.5 or 10 mg/mL, see Appendix A for additional information on collagen stock preparation) to achieve final collagen concentration of 1.25 or 6 mg/mL, respectively. Final cell-gel mixtures of 60 μL were pipetted into each well and allowed to gel for 45 minutes at 37°C. After gelation, constructs were given RPMI-B27 (with insulin) and fed every other day for 14 days. All co-cultured constructs were made with a 1:1 cell density ratio of cardiomyocytes to stromal cells. Final cardiomyocyte density in all constructs was ~16 x 10^6 per mL.

Constructs for sharp boundary experiments were made by two step gelation: first, a stainless steel block was placed in one half of the well to allow the cardiomyocyte-only side to undergo 30 minutes of gelation, then the block was removed and the co-culture mixture (cardiomyocytes and HS27a stromal cells in liquid collagen) was added, followed by an additional 30 minute gelation period. All constructs were cultured for 14 days, fixed, histologically processed and stained (additional methods in Appendix A). Constructs were fixed while under constant strain in the tissue molds.

2.3.3 Contractile force generation analysis

Functional analysis was carried out on constructs after two weeks of maturation as previously described [70] (additional methods in Appendix A). In brief, construct sections were stretched in 5% increments up to 20 - 25% of their total length, and their resulting

passive tension and spontaneous active force traces were recorded and analyzed using customized LabView software. Stress-strain relationships were recorded for each construct at basal conditions with no electrical stimulation. After that, the constructs were stimulated at max stretch (25%) at 1, 1.5, 2, and 3 Hz using a field stimulator with 5V and 40ms pulse duration. The spontaneous beating rate of each construct was determined by taking the inverse of time between active contractions at maximum stretch in unstimulated preparations.

2.3.4 *Microvessel fabrication*

GCaMP3 hESC-CMs (16×10^6 per mL, final) and stromal cells (16×10^6 per mL, final) were mixed with dense collagen (6 mg/mL final concentration). Microfeatures were embedded in the cell-containing gel using techniques of injection molding and soft lithography as previously described [102]. Collagen with density less than 4 mg/mL fails to maintain mechanical integrity for the microstructures. The final constructs have dimensions of 8 x 17 x 1 mm and parallel posts flanking the construct to provide uniaxial strain. A patterned network was molded into the top device by using a microfabricated PDMS stamp with channel dimensions 125 µm x 125 µm on the bottom surface of the top device. After gelation, the devices were assembled together to create an enclosed microfluidic network. The network was seeded with 10 µL human umbilical vein endothelial cell (HUVECs, passage 5) suspension at a density of 10×10^6 per mL in endothelial growth medium (EGM, Lonza). After 1 hour of attachment under static conditions, EGM was perfused through the microvessels under gravity-driven flow through attached reservoirs (initial pressure of 1 cm H_2O, replenished every 12 hours).

Constructs were additionally submerged in a 3:1 mixture of cardiomyocyte media (RPMI 1640 basal medium with B27 Supplement (Invitrogen) containing insulin) and EGM. At day 7 and 14 of culture, GCaMP3 fluorescence was observed and recorded with a Canon HD video camera (HF S20) to assess cardiomyocyte function and tissue-level electrical properties. After 14 days, the constructs were fixed and stained for cardiac troponin T (cTnT; 1:100; mouse anti-human; Fisher) to label cardiomyocytes and CD31 (1:25; rabbit anti-human; Abcam) to label endothelial cells, followed by imaging *in situ* with confocal fluorescence microscopy. All antibodies and solutions were perfused through the network and used to submerge the construct.

2.3.5 Statistics

Single variable analysis between two samples was compared by Student's t-test assuming unequal variance. Unless otherwise noted, at least 3 biological replicates were performed with 2-3 technical replicates in each. The number of biological replicates was used to determine significance. Results are presented as mean ± SEM. For all results, significance was defined as $*p < 0.05$, $** p<0.01$.

Additional methods are included in Appendix A.

2.4 Results

2.4.1 Cardiomyocytes alone in dense collagen do not form functional cardiac tissue.

The incorporation of perfusable microvessels in collagen-based constructs requires the use of dense collagen to maintain structural integrity of the fabricated channels [126]. To

evaluate the influence of collagen density on the structure and function of cardiac constructs in a higher throughput manner, we used rectangular wells (Fig 2.1A) to generate cardiac tissue constructs under uniaxial strain with human stem cell-derived cardiomyocytes (hESC-CMs) in both low (1.25 mg/mL) and high (6 mg/mL) collagen concentrations (initial complex moduli of 81.0 ± 14.8 Pa and 281.8 ± 17.1 Pa, respectively, see additional methods in appendix A). After two weeks in culture, hESC-CMs in 1.25 mg/mL remodeled the collagen gel and formed compact tissues, with cross-sectional areas of 0.133 ± 0.038 mm^2 (Fig 2.1A, iv; 2.1B, i). In 6 mg/mL collagen, hESC-CMs were unable to compact the matrix, which resulted in isolated cell islands and a lack of cell-cell contact (Fig 2.1B, ii). The cross sectional area of the constructs was 1.247 ± 0.142 mm^2, nearly 10 fold higher than in low density collagen (Fig 2.1C). The greater degree of compaction in low density collagen led to a final cell density of $1.2 \pm 0.4 \times 10^6$ per mm^3, approximately 20 fold higher than in 6 mg/mL (Fig 2.1D). In addition, hESC-CMs showed markedly different morphology in collagen of different densities. In collagen of 1.25 mg/mL, cardiomyocytes expressed alpha actinin robustly throughout the construct in a striated pattern, indicating sarcomere formation in the majority of cells (Fig 2.1E, i). In collagen of 6 mg/mL, regions of striated alpha actinin expression were visible, but these regions were sparse and isolated (Fig 2.1E, ii). To evaluate electrical synchronization of the tissues, we performed fluorescent imaging of calcium transients. In collagen of 1.25 mg/mL, there was synchronous excitation and contraction throughout the whole constructs (SV2). In collagen of 6 mg/mL, electrical activation events were isolated with no propagation, indicating the cardiomyocytes were alive and able to undergo spontaneous excitation, but were not connected or electrically

synchronized (SV3). Collectively, these results suggest that cardiomyocytes in dense collagen retained necessary molecular and structural components for electromechanical function, but were unable to organize into an integrated tissue.

Figure 2.1. Cardiac constructs with hESC-CMs in low and high density collagen. (A) Micropost culture system: An acrylic negative template (i) used to generate PDMS molds with posts at each end (ii) which was then seeded with collagen pre-mixed with hESC-CMs (iii). Construct remodeling and compaction after 2-3 days (iv). (B) Hemotoxylin and eosin (H&E) staining of constructs in (i) 1.25 mg/mL and (ii) 6 mg/mL collagen after culture for 14 days. (C-D) Final cross sectional area (C) and cellularity (D) of constructs – D14 (*p<0.05; N=4-7 biological replicates). (E) Confocal images of sarcomeric α actinin and nuclei in (i) 1.25 mg/mL and (ii) 6 mg/mL collagen at 40X (top panel) and x3 optical zoom (bottom panel). Scale bars: 50 µm.

2.4.2 Stromal cell co-culture promotes cardiomyocyte organization and matrix remodeling in both low and high density collagen.

Stromal cells have been shown to be critical for matrix synthesis and remodeling during normal development and cardiac regeneration [80,127]. In a normal adult mammalian heart, stromal and fibroblast populations contribute to approximately half of the total cell number [127,128]. To improve the structure and function of our cardiac constructs, we co-cultured cardiomyocytes with human stromal cells (bone marrow-derived HS27a line [125]) in both low and high density collagen. In both collagen matrices, co-cultured constructs were significantly more organized, with higher cellularity and greater alignment (Fig 2.2). hESC-CMs had more organized striated alpha actinin and a larger degree of alignment in co-cultured constructs compared to those in cardiomyocyte-only constructs (Fig 2.2A, ii; 2.2B, ii, 2.2E). Co-culture increased expression and organization of matrix proteins, predominately fibronectin and collagen IV, both of which appeared to align along the direction of axial strain and cellular elongation (Fig 2.2A, iii-iv; 2.2B, iii-iv). The matrix constituents heparin sulfate, laminin, and versican were not detected in these co-cultured constructs by immunohistochemistry (data not shown). In dense collagen particularly, co-culture led to a significant improvement in tissue compaction and homogeneity with a nearly 60% decrease in cross sectional area (Fig 2.2C) and a 6-fold increase in cell density (Fig 2.2D) compared to cardiomyocyte-only conditions. Myofibrils showed significantly enhanced alignment along the direction of uniaxial strain for the co-culture conditions in both low and high collagen matrix (Fig 2.2E). Cardiomyocyte sarcomere length also increased significantly with co-culture in high density collagen (Fig 2.2F), indicating greater myofilament organization and maturation.

These findings suggest that stromal cells promote matrix synthesis and remodeling required for hESC-derived cardiomyocytes to elongate and structurally mature.
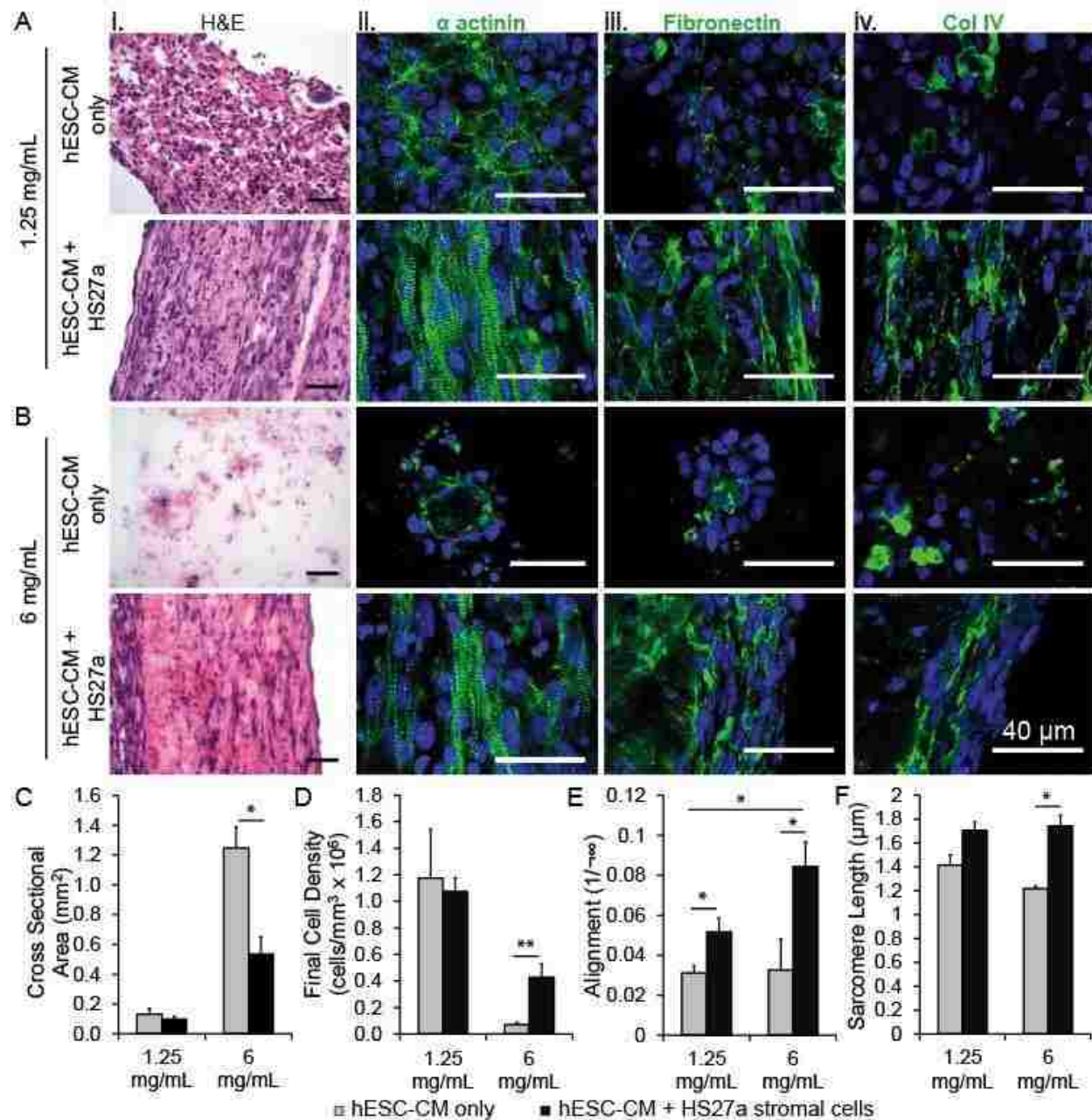
Figure 2.2. Co-culture with HS27a stromal cells in cardiac constructs. (A-B) Histological sections of (A) 1.25 mg/mL and (B) 6 mg/mL collagen. (top: hESC-CM only; bottom: co-cultured); H&E (i), sarcomeric α actinin (ii), fibronectin (iii), and collagen IV (iv). (C-F) Quantitative comparison of (C) final cross sectional area, (D) final cell density, (E) cardiomyocyte alignment, and (F) sarcomere length (*p<0.05; **p<0.01; N=2-4 biological replicates). Scale bars: 40μm.

2.4.3 Co-cultured dense collagen constructs are electromechanically functional

An essential requirement for engineering functional myocardial tissue is its ability to propagate an electrical signal followed by whole construct contraction and force generation. Co-cultured constructs with hESC-CMs and stromal cells in 6 mg/mL collagen showed calcium wave propagation and contraction throughout the whole construct, indicating sufficient cell-cell contacts and maturation of hESC-CMs (SV4).
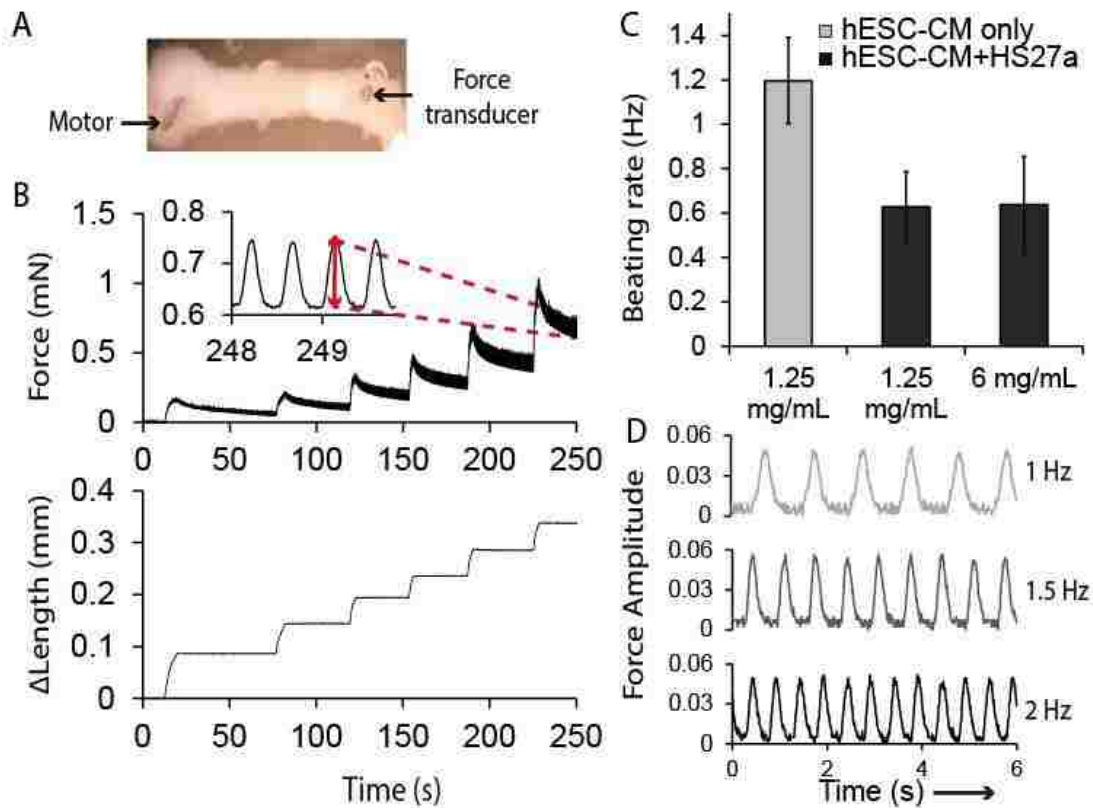
Figure 2.3. Functional characterization of co-cultured constructs. (A) Construct mounted between force transducer and motor. (B) Force trace displaying passive tension and active twitch force during incremental step-wise length increases for a co-cultured construct in 6 mg/mL collagen. Inset: enlarged view at maximum strain ($\epsilon = 0.25$). (C) Spontaneous beating rate at 37°C (D) Sample stimulation traces at $\epsilon = 0.25$ of co-cultured constructs in 6 mg/mL. (N=3 biol. rep.)

We further mounted the constructs between a force transducer and a motor (Fig 2.3A) and measured the length dependence of force generation for each construct by

stretching incrementally with 5-10% steps and recording twitch force at each length step (Fig 2.3B). All constructs produced increasing twitch force with increased strain, demonstrating the tissue-level correlate of the Frank-Starling relationship, where increased length triggers increased active and passive force (Fig 2.4A - C). Co-cultured constructs in 6 mg/mL collagen produced a peak active force of 0.1 mN/mm^2, which is comparable to co-cultured constructs generated in low collagen (Fig 2.4D) as well as previously reported values for collagen-based engineered cardiac tissue [70,117,129].
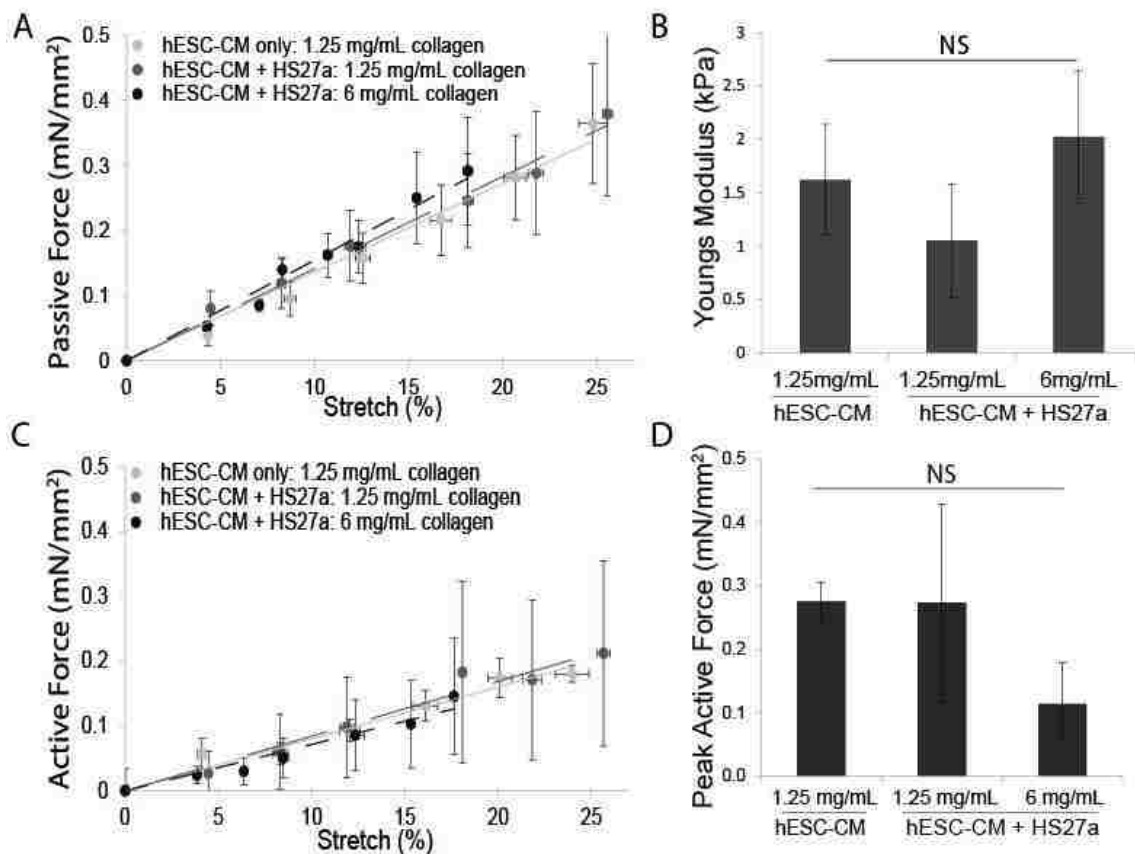
Figure 2.4 – Passive and active force characterization. (A) Passive tension vs. increased strain (B) Young's modulus (slope of passive tension vs. strain). No significant differences for three measurable conditions. (C) Representative Frank-Starling curves depicting linearly increasing length dependent active contractions of all construct groups. (D) Peak active force of constructs (at 25% stretch) after 14 days of culture. Differences are not significant.

A functional engineered cardiac construct is expected to follow a range of stimulation frequencies in order to electrically synchronize with the host during future therapeutic applications. We measured the spontaneous beating rate of cardiac constructs since automaticity is a key indicator of cardiac subtype and electrophysiological maturation [93,130,131]. In constructs with cardiomyocyte-only conditions in 1.25 mg/mL collagen, the average spontaneous beating rate is 1.2 Hz. Co-culture conditions resulted in a slight decrease of spontaneous beating rate to approximately 0.6 Hz in both 1.25 and 6 mg/mL collagen, although the decrease is not statistically significant (Fig 2.3C). Importantly, all three groups, including co-cultured constructs in dense collagen, were able to reliably follow an electrical stimulation pace up to 2 Hz (Fig 2.3D) while maintaining the same magnitude of force generation (Fig 2.5). In response to 3 Hz stimulation, all construct groups were unable to follow the pace consistently. These findings are consistent with previous studies showing that fibroblasts reduce the intrinsic beating frequency of cardiomyocytes and non-myocytes play a role in modulating the electrophysiological maturation of stem cell derived cardiomyocytes during differentiation [64,132].
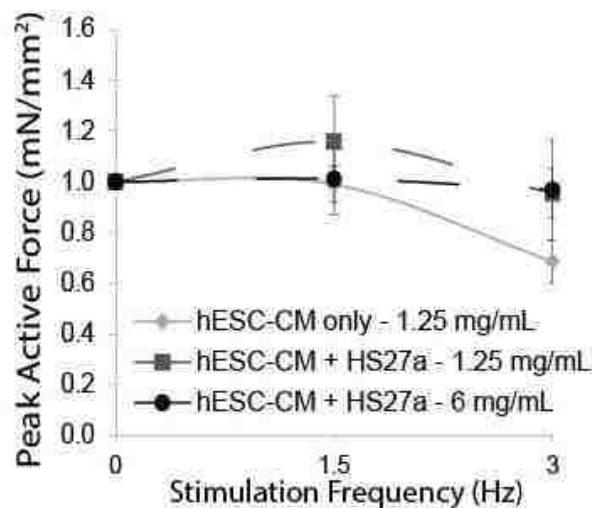
Figure 2.5 – Force-frequency relationship of construct groups. An increase in stimulation frequency to 3Hz resulted in downward trend of force generation in hESC-CM only constructs (light grey solid curve). Constructs co-cultured with HS27a stromal cells are able to maintain comparable force with electrical stimulation at 1.5 and 3 Hz compared to unstimulated.

2.4.4 *The type of stromal cells in co-cultured constructs influences their interactions with cardiomyocytes and matrix remodeling*

Different populations of "stromal cells" or "fibroblasts" have drastic differences in their phenotype, gene expression, and signaling [133]. To understand how stromal cells from different sources affect remodeling and cellular alignment in cardiac constructs, we generated cardiac constructs by co-culturing cardiomyocytes with four different fibroblast or stromal cell lines in low density collagen for 4 days. These stromal cells included two immortalized human bone marrow derived stromal cell lines (named HS27a and HS5 [125]), primary human dermal fibroblasts (hDF), and primary isolated fetal human heart NG2+/PDGFRβ+ cells (FHH). HS27a and HS5 have been extensively characterized and while both lines secrete a plethora of ECM proteins, they have distinct functions due to differing expression of matrix proteases and cytokines [125,134,135]. hDF are known to secrete vast amounts of extracellular matrix and matrix degradation proteins normally and during wound healing [136]. FHH cells were selected based on their expression of pericyte markers NG2 and PDGFRβ, suggesting a more pericyte-like function of vascular stabilization [137,138]. When these different stromal cells were co-cultured with cardiomyocytes in collagen constructs, distinct differences were observed regarding cellular and matrix alignment. Compared to constructs with cardiomyocyte-only conditions, HS27a and hDF co-cultured constructs showed greatly improved cardiomyocyte alignment and matrix synthesis (Fig 2.6A-C), similar to results shown in Figure 2. However, the HS5 and FHH co-cultured constructs had no improvement in cardiomyocyte structure and organization and no evident cellular or matrix alignment (Fig 2.6D-E). Furthermore, co-culturing with HS5 resulted in poor construct integrity with
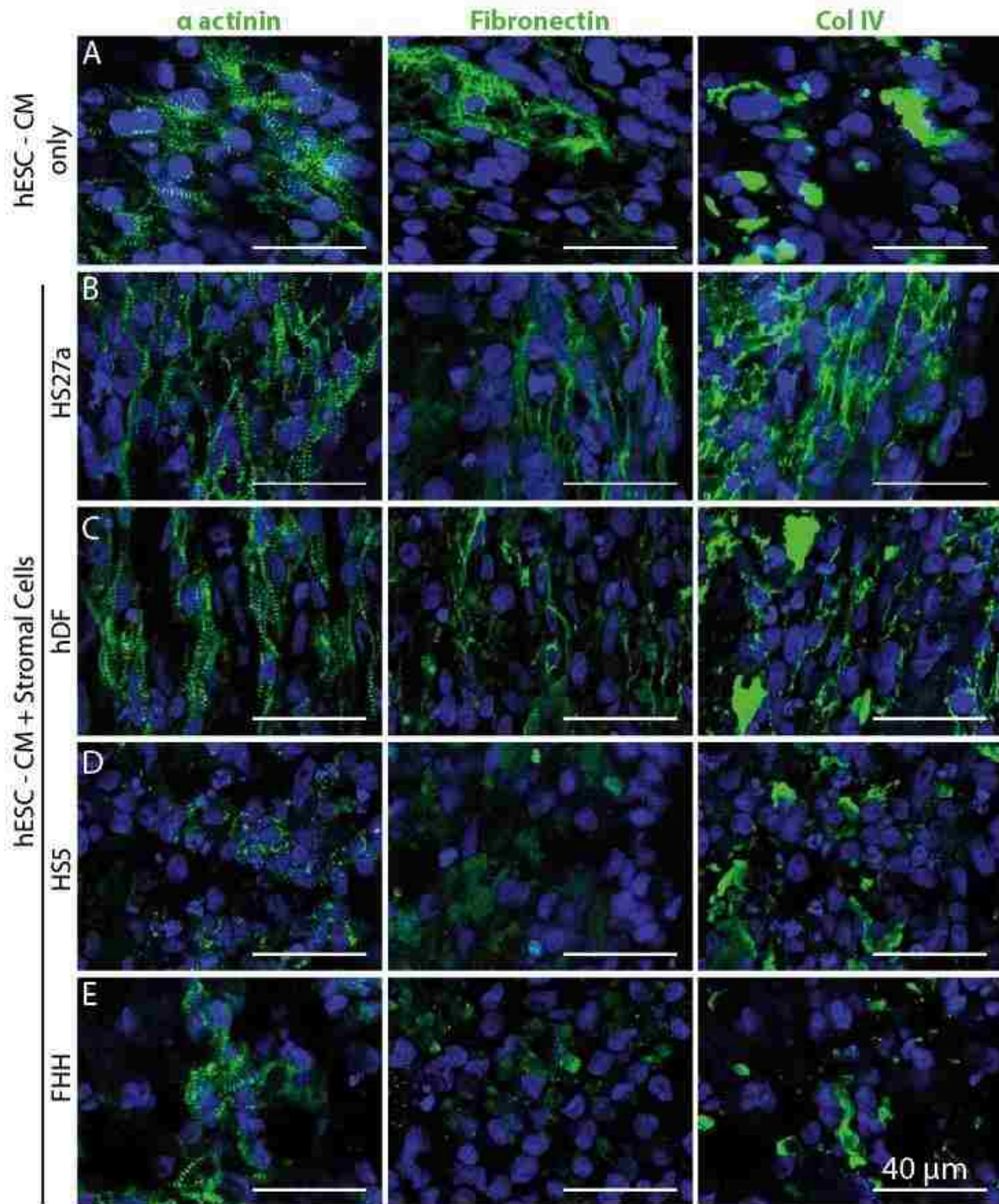
Figure 2.6 – The effect of stromal cell type on cardiac remodeling. Immunofluorescent images of α actinin (left), fibronectin (middle), and collagen IV (right) in (A) hESC-CMs only or with (B-E) co-culture conditions. (B) bone marrow derived HS27a stromal cells, (C) human dermal fibroblasts (hdF), (D) bone marrow derived HS5 stromal cells, and (E) fetal human heart NG2+/PDGFRβ+ cells (FHH). All constructs here were generated in 1.25 mg/mL collagen and processed after 4 days of culture. N=3-4 biological replicates (each with 2-3 technical replicates).

a breakdown of matrix and structure after approximately 4 days in culture. Compared to cardiomyocyte only constructs, co-cultured constructs had upregulated mRNA expression of fibronectin (FN1) and type I collagen (Col1A2) with the most pronounced increases seen in HS27a and hDF co-cultured constructs (Fig 2.7). Taken together, these results suggest that HS27a and hDF promote matrix remodeling that is suitable for promoting cardiomyocyte growth and organization.
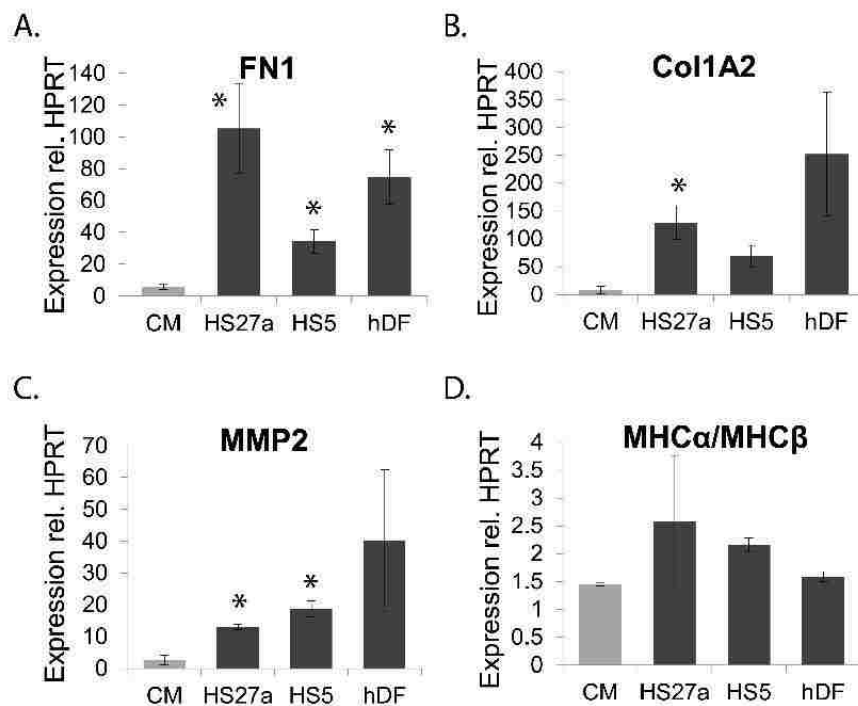
Figure 2.7 – Gene expression analysis after co-culture with different stroma cell types. Expression (relative to HPRT) of matrix proteins (A) FN1, (B) Col1A2, (C) matrix metalloproteinase 2 (MMP2), and (D) cardiac maturation markers (MHCα, MHCβ; expressed as a ratio of the two subunits) were evaluated.

2.4.5 Cardiomyocyte alignment requires close proximity to stromal cells.

To understand how stromal cells provide cues for cardiomyocyte alignment and maturation, we generated a composite construct in 6 mg/mL collagen with a sharp boundary between two halves: one half containing only cardiomyocytes and the other half co-cultured with HS27a stromal cells (Fig 2.8A). After 14 days of culture, stromal cells remained in the co-cultured half region with minimal migration (Fig 2.8B, i-ii).
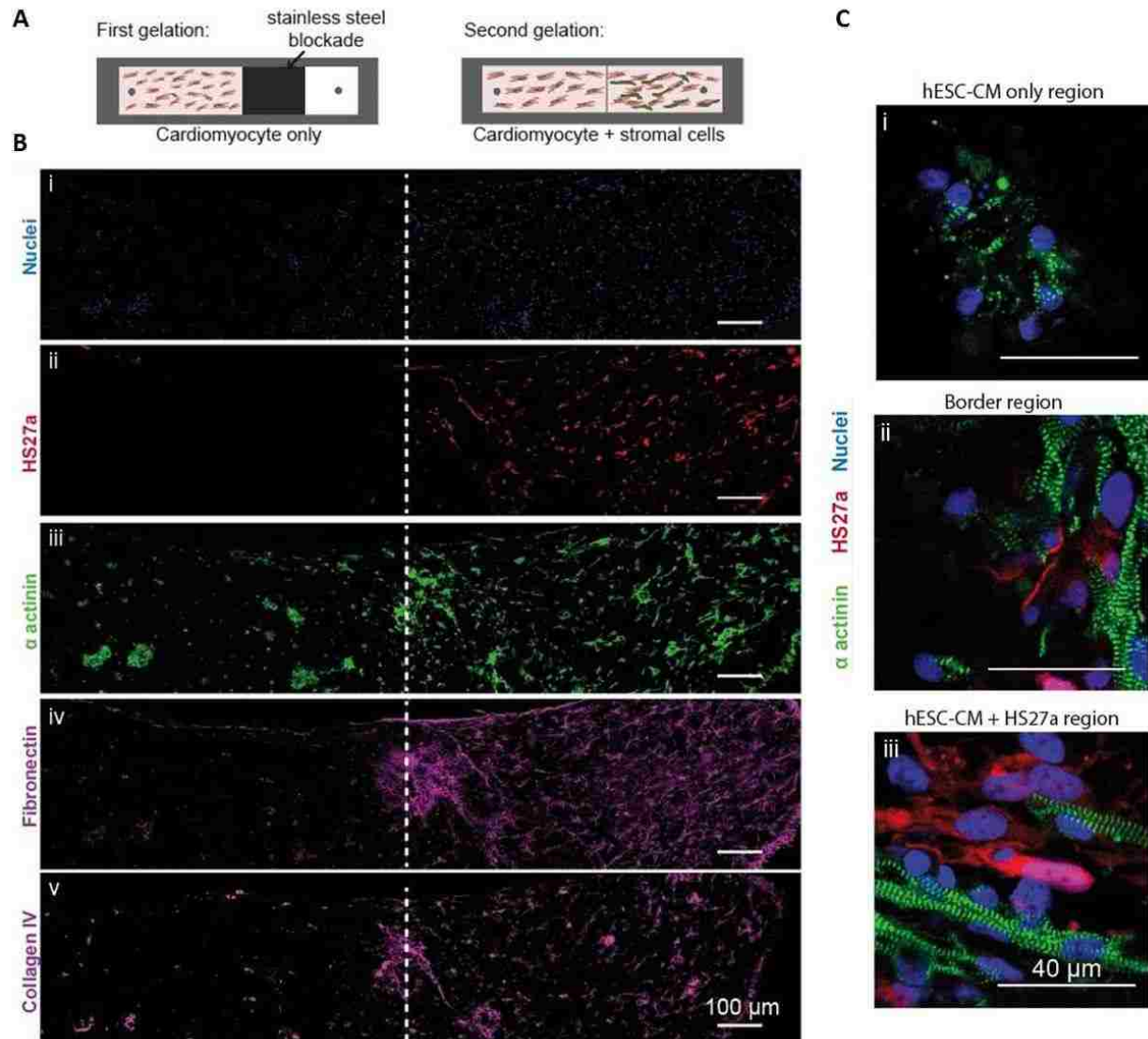
Figure 2.8 – Boundary experiment between hESC-CM only and co-cultured constructs. (A) Schematic of construct generation using a two-step gelation process. (B) Large view confocal immunofluorescence images of serial cryosections near the stromal cell interface (white dotted line): (i) Hoechst staining (ii) HS27a stromal cells (marked with red fluorescent protein), (iii) α actinin, (iv) fibronectin, and (v) collagen IV. (C) Higher magnification image of (i) cardiomyocyte only region, (ii) the border region, and (iii) the co-cultured region. N=3 biological replicates.

Consistent with the stand-alone construct conditions, the co-cultured half of the construct had higher and more integrated cellularity (Fig 2.8B, i-ii) with stronger and more uniform alpha actinin expression in cardiomyocytes compared to the

cardiomyocyte only region (Fig 2.8B; iii). More organized matrix proteins such as fibronectin and collagen IV (Fig 2.8B; iv-v) were deposited in the co-cultured half of the construct. Further away from the boundary between the two halves, the cardiomyocytes displayed similar structural organization as the two distinct culture conditions shown above: disarrayed sarcomere striations in cardiomyocyte only conditions (Fig 2.8C, i) compared to robust sarcomere formation and cellular alignment in the direction of uniaxial strain in co-cultured region (Fig 2.8C, iii). At the boundary between the two halves, cardiomyocyte alignment sharply declined between the stromal and non-stromal regions (Fig 2.8C, ii). This suggests that close proximity of stromal cells was required for proper matrix remodeling and cardiomyocyte structural organization in 3D constructs, and paracrine factors alone were not sufficient to induce such effects.

2.4.6 Engineered microvasculature within functional cardiac constructs

The ability to generate cardiac constructs in a dense collagen matrix allowed us to embed microchannels within the construct to form patterned vasculature. We modified our previous soft lithographic injection molding technique for engineering microvessels [102] and generated 3D functional cardiac tissue with embedded endothelialized channels. Namely, the system was miniaturized to lessen cardiomyocyte demand and facilitate higher throughput testing. Consequently, the device is now open on the top and bottom to allow for sufficient media around constructs; and horizontal posts located just outside of both the inlet and outlet created uniaxial strain (Fig 2.9 and Fig 2.10A). Constructs generated using this fabrication method and optimized co-culture conditions had intact network geometry immediately after fabrication. We then perfused endothelial cells
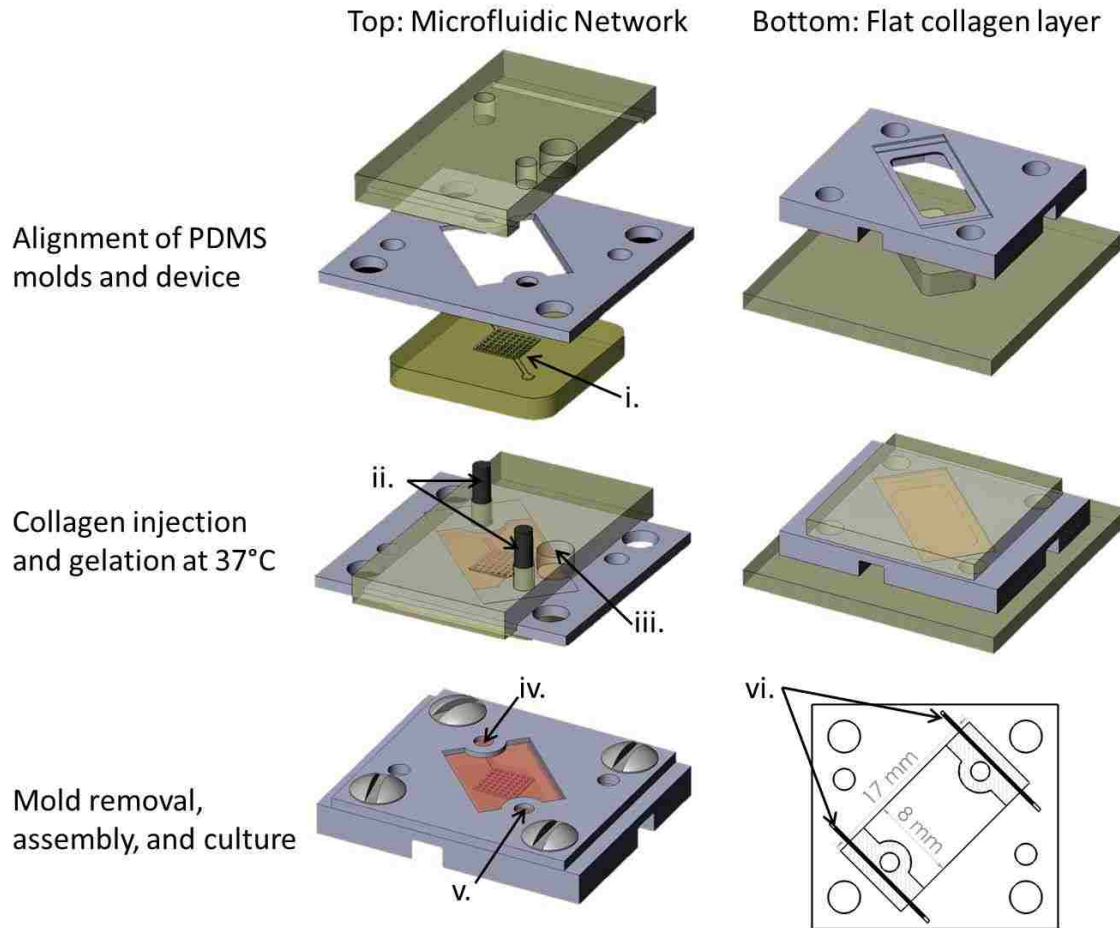
Figure 2.9 – Cardiac construct with engineered µV: design schematic. Re-designed injection molding process optimized for microvessel fabrication within cardiac constructs.

through the network and observed attachment on the microchannels within one hour after seeding, with complete attachment overnight (Fig 2.10A). The structural integrity of the network was maintained throughout 14 days of culture, and attached endothelial cells formed CD31+ junctions within the patterned network (Fig 2.10B; i). The interstitial space between the patterned channels contained dense populations of both stromal cells and cardiomyocytes (Fig 2.10B; ii-iii). Cardiomyocyte morphology was elongated with uniform distribution of cTnT positive cells throughout the interstitial collagen space (Fig 2.10B-C, ii). Endothelial sprouts were observed to extend from the patterned

network into the bulk of the construct (Fig 2.10C; i arrowheads). Importantly, we found that throughout the remodeling process and two week culture, the endothelial-lined channels were able to maintain their patency (Fig 2.10D; i). Stromal cells, and in some places the cardiomyocytes, followed the vasculature and elongated along the longitudinal direction of the microvessels (Fig 2.10D; i) and the endothelial sprouts (Fig
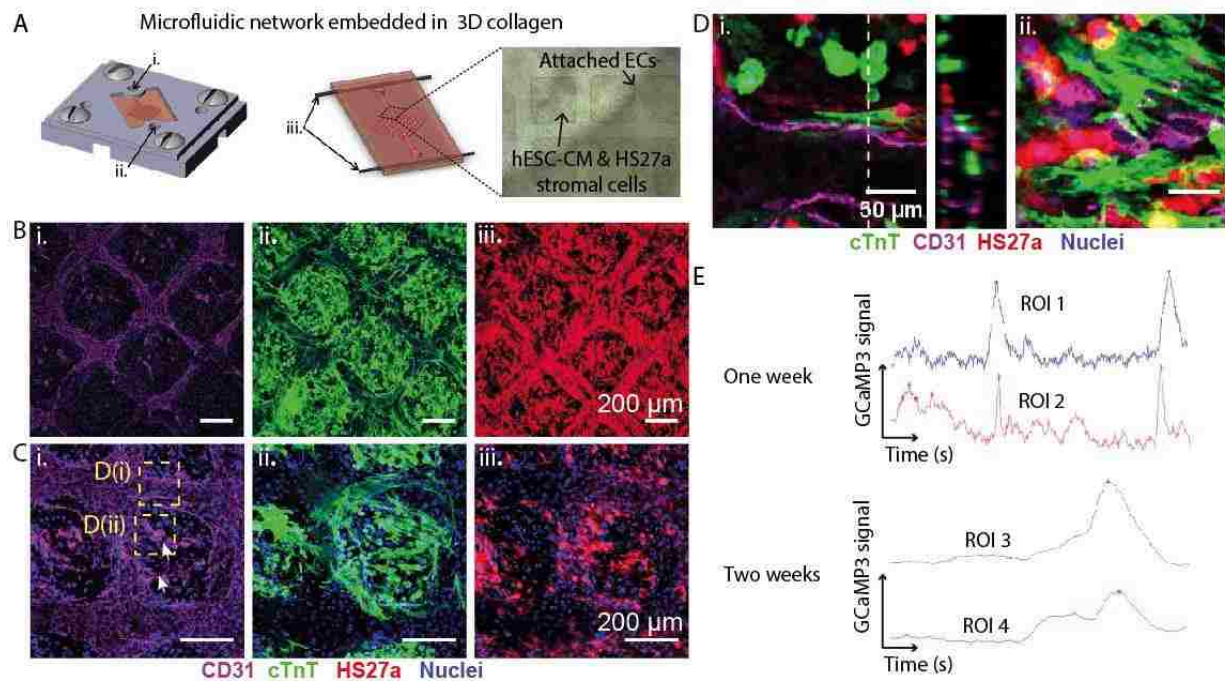
Figure 2.10 – Successful incorporation of patterned vasculature in cardiac construct. (A) Fabrication of microfluidic device with embedded microchannel in cardiomyocyte embedded collagen matrix: (i) inlet, (ii) outlet, (iii) horizontal posts for uniaxial strain (see methods for more detail). (B) Z-stack projection images of (i) CD31, (ii) cTnT, and (iii) HS27a stromal cells. (C) Z-stack projection images at a higher magnification view showing (i) endothelial sprouts, (ii) elongated CM and (iii) interstitial HS27a stromal cells (D) Zoomed in regions (i) and (ii) from C (i) with cross section view of patterned channel (middle panel). (E) Sample GCaMP3 traces after one and two weeks of culture for two regions of interest.

2.10D; ii). In comparison, control constructs generated using the same device but without an endothelialized microvessel had poor cardiac morphology with a lack of structural organization of both cells and constructs (not shown). To evaluate the function

of cardiac constructs with patterned vasculature, we performed calcium imaging using GCaMP3 fluorescence after one and two weeks in culture and analyzed the traces at two distinct regions of interest to assess electrical synchronization throughout the construct. We observed synchronous electrical wave propagation after just one week in culture, and increased synchronization between two identified regions of the construct after two weeks of culture with much of the background signal from isolated electrical activity gone (Fig 2.10E; SV5). These data demonstrate that our optimized cellular and matrix conditions enables the generation of functional cardiac constructs with endothelialized microchannels and potentially fully vascularized cardiac tissue.

2.5 Discussion

In recent years, many methods of generating perfusable, interconnected networks of vessels have emerged as viable approaches to vascularization of engineered tissue. For example, 3D printing of sacrificial vascular networks into a three dimensional grid [99], the generation of aligned branched microvessels with alginate fibers embedded in the matrix [100], and microfabricated vessels [102] are all exciting approaches with vast implications in microvascular engineering and promising potential for the generation of pre-vascularized tissues. However, success has been limited in combining these vascular fabrication techniques with standard 3D cardiac tissue cultures. This limitation stems in part from incompatible matrix and mechanical conditions that do not provide favorable conditions for both cardiac function and incorporation of vasculature. The formation of compact cardiac tissue with synchronous contractions requires remodeling to occur so that the cells may form proper cell-cell junctions and establish electrical

communication, but this remodeling tends to collapse embedded channels due a lack of mechanical support [101].

In this study, we used co-culture with cardiomyocytes and stromal cells in dense collagen and successfully demonstrated that we can promote cardiomyocyte organization and function and simultaneously maintain the mechanical integrity of microvessels in 3D cardiac constructs. The additional stromal cells promoted significant matrix remodeling, which presumably was through the combination of ECM synthesis and proteolytic degradation via synthesis and release of matrix metalloproteinases [139]. We showed that cardiomyocytes aligned along the same direction as the matrix proteins, which was also the direction of uniaxial strain applied on the 3D constructs. Previous studies have shown that fibroblast and stromal cell populations remodel matrix and induce matrix alignment in response to uniaxial strain [140–142]. These aligned matrix proteins possibly serve as the topographical cues for the cardiomyocytes to align and mature [64,143]. Results from our composite constructs demonstrated that paracrine signaling through soluble factors was unlikely to be the predominate mechanism at hand. Rather the close proximity and interactions between stromal cells and cardiomyocytes promoted cardiomyocyte organization in co-cultured constructs. This further supports the suggested mechanism that local stromal cell-induced matrix synthesis and remodeling allows for adjacent cardiomyocytes to initiate cell-ECM contact, undergo elongation, and structurally mature.

Stromal cells from different origins showed different capacities to facilitate sufficient matrix alignment and cardiac construct formation. Co-culture with both human dermal fibroblasts and marrow derived HS27a stromal cells led to remodeling and cardiac

structural maturation while co-culture with HS5 stromal cells and NG2+/PDGFRβ+ fetal human heart cells did not. Human dermal fibroblasts are known to be highly proficient at remodeling matrix, particularly in three dimensional cultures [144]. HS27a and HS5, although both originated from the human bone marrow, appeared to have drastic differences in their ability to remodel matrix and support cardiac morphology. HS27a has been shown to have much higher expression of stromal cell-derived factor 1, regulators of G protein signaling, and tissue inhibitors of matrix metalloproteases, than HS5 [135]. In addition, unlike HS5 stromal cells, HS27a stromal cells strongly express the Notch surface ligand Jagged1 [134,135] whose signaling is known to play an important role during cardiac repair, namely by inducing cardiomyocyte proliferation and growth [145,146]. HS5 stromal cells, however, express much higher levels of inflammatory cytokines, such as IL-6 and IL-8, compared to HS27a [125,134,135]. Prolonged exposure to such inflammatory signals can have adverse effects in the heart such as myocardial hypertrophy and are known predictors of heart failure [147–149]. Our use of different stromal and fibroblast lines revealed that not all stromal cells are compatible with cardiac construct formation. Instead, specific stromal cell lines are required to produce sufficient matrix deposition and assembly to elicit alignment and a beneficial response of the cardiomyocytes. Fibroblasts, and particularly dermal fibroblasts, are well known to adapt to external forces and play a key role in modulating mechanical tensions within the tissue through ECM remodeling, cytoskeletal rearrangement, and cellular contraction [150]. Indeed, this characteristic of dermal fibroblasts has already been utilized for a wide range of tissue engineering applications where matrix remodeling and organization are required [151,152]. Our finding that the immortalized HS-27a stromal cells

are similarly effective is advantageous for their use in optimizing engineered tissues. Moving forward, the use of cardiac or stem cell derived fibroblasts would allow researchers to match the sources of each input cell type to better mimic a cardiac environment.

In addition to cellular alignment and global improvement in cardiac structure, co-culture with stromal cells led to myofilament maturation within the cardiomyocytes. Cardiomyocyte only constructs had sarcomere lengths ranging from 1.2 - 1.4 µm which is characteristic of immature thick filaments and sarcomeres. In co-culture conditions, cardiomyocytes had sarcomere lengths that ranged from 1.7 µm to 1.8 µm, more similar to that of a mature adult-like cardiomyocyte [65,153]. Although structural maturation was observed, the magnitude of force production was still <1% of adult cardiac tissue which generates a twitch force on the order of 100 mN/mm^2 [154]. This could be attributed to the functional immaturity of stem cell derived cardiomyocytes and to the relatively low density of cardiomyocytes in the constructs. Longer term culture [65] and higher cellular densities could potentially further promote the functional maturation of hESC-CMs and engineered cardiac tissue.

Optimized cellular and matrix culture conditions enabled us to successfully generate microvessels in 3D cardiac tissues. We demonstrated vascular patency and cardiac function in constructs for up to two weeks: the vasculature displayed remodeling capability and cardiomyocytes developed proper cardiac morphology and function with necessary cell-cell contacts. We showed that endothelial cells sprout outward from the patterned vasculature into the surrounding matrix, suggesting the potential of our platform to generate a fully vascularized constructs with patterned small arteriole

conduits as well as capillaries. This sprouting and endothelial outgrowth may be the result of the crosstalk between endothelial cells and cardiomyocytes/stromal cells and possible hypoxic gradients generated towards the distal regions of the constructs. The sprouting and endothelial outgrowth may also vary for different sources of endothelial cells, and an alternative endothelial cell source could be incorporated into the microvessel to promote additional angiogenesis [155]. Our vascularized cardiac tissue provides a useful system to understand the effects of endothelial cells, hydrodynamic stresses, and transport processes on cardiomyocyte maturation and function. We hypothesize that the presence of planar perfusable vessels in the cardiac tissue will guide additional vascular connections within the surrounding construct and further promote integration to the host vasculature once implanted. This study provided a proof-of-principle demonstration of engineered cardiac tissue with patterned vasculature. Additional studies will be pursued to further characterize the impact of the microvascular network on cardiomyocytes in terms of survival, thickness of viable construct, cardiac morphology, and function. The current system could be further modified to pattern multi-layered 3D vasculature throughout the construct by stacking layers of microvessels together or using alternative microfabrication techniques such as 3D printing. As these approaches mature, pre-vascularized cardiac tissue can be made in large scale and potentially used for the treatment of ischemic heart disease.

Chapter 3.

Characterization of stem cell-derived endothelial cells as a vascular cell source for regenerative therapies

Parts of this chapter have been published in the following manuscripts: [155,156]

Note: maiden name – Roberts

- Palpant, N.J., Pabon, L., **Roberts, M.A.**, et. al. Inhibition of β-catenin signaling respecifies anterior-like endothelium into beating human cardiomyocytes. *Development* 142(18): 3198-3209. PMID: 26153229.

- Palpant, N.J., Pabon, L., Friedman, C.E., **Roberts, M.A.**, et. al. Generating high-purity cardiac and endothelial derivatives from patterned mesoderm using human pluripotent stem cells. *Nature Protocols* 12(1): 15-31. PMID: 27906170.

3.1 Abstract

The most commonly used endothelial cell source for tissue vascularization is human umbilical vein endothelial cells (HUVECs). Due to their relatively low abundance and propensity to die *in vivo*, we sought to identify a more suitable cell source for the generation of patterned vasculature. We developed a protocol to differentiate two populations of endothelial cells, arising from the anterior or posterior mesoderm, from pluripotent stem cells (hESC-ECs) and assessed their endothelial function in 2D and in 3D vascular platforms. We found that both cell populations undergo tubulogenesis, form angiogenic sprouts, and form stable microvessels with luminal geometry and endothelial

junctions in our soft lithographic engineered microvessel (μV) platform. One of the key findings of this study was that anterior-derived endothelial cells were more angiogenic than posterior ECs under flow conditions. To expand off this angiogenic potential, we generated highly vascularized constructs by incorporating additional anterior hESC-ECs in the collagen matrix to promote anastomosis between angiogenic sprouts and the interstitial tubulogenic ECs. Endothelial lumens that formed in the collagen matrix integrated with the patterned μV by incorporating directly onto the vessel wall and by forming anastomotic connections with angiogenic sprouts. We demonstrated that these anastomotic connections are perfusable and that the presence of the patterned μV improves lumen formation in terms of vascular density and average lumen size. Finally, to assess the suitability of hESC-ECs for transplantation, we assessed the thrombogenicity of the cells through exposure to whole blood, and found that hESC-EC-μVs are non-thrombogenic with physiological endothelial-platelet interactions. Collectively, this data illustrates that hESC-ECs are a suitable cell source for vascular engineering with definite endothelial morphology and function, high angiogenic potential, and non-thrombogenic platelet interactions.

3.2 Rationale

In addition to the importance of structural patterning and organization of endothelial cells (ECs), identifying alternatives to HUVECs (human umbilical vein endothelial cells) as the EC source will be vital for the translation of vascularization strategies [101]. HUVECs are a commonly used endothelial cell source due to their mature endothelial phenotype and ease of availability. However, vessel instability, poor survival *in vivo*, and

immune incompatibility issues have led many researchers to begin looking elsewhere for endothelial sources [157]. Furthermore, the ability to generate tissues from patient-specific or autologous cell sources through the use of iPSC technology would be a great advantage in the future application of regenerative medicine therapies, drug screens and disease modeling.

Through collaboration with Dr. Nathan Palpant during his time as a post-doctoral fellow in the Murry lab, we generated two distinct populations of endothelial cells by modulating Activin A and BMP4 signaling to mimic the spatial expression of these molecules in the developing embryo during mesoderm specification [155]. Dr. Palpant showed that treatment with high Activin/low BMP4 or low Activin/high BMB4 results in progenitor populations that resemble the anterior or posterior mesoderm, respectively. The polarization of the mesoderm is characterized in part by elevated NFATC1 in the anterior region and elevated HAND1 in the posterior mesoderm, an expression pattern also observed in our differentiated cell preparations. Furthermore, expression of NFATC1 is associated with the developing endocardium which ultimately gives rise to multiple cardiac lineages, including many vascular endothelial cells of the coronary circulation [13,158]. Taken together, these data suggests that our endothelial differentiation protocols, in particular for anterior-derived endothelial cells, gave rise to endothelial cells with similar developmental origins of the coronary vasculature.

The overall goal of this aim was to characterize the endothelial functions of stem cell derived endothelial cells and determine whether they are a viable option as a vascular cell source. To assess endothelial function, we evaluated hESC-EC ability to undergo tubulogenesis and angiogenesis in three-dimensional collagen-based assays.

We then generated engineered µVs with hESC-ECs and assessed junction formation, lumen patency, angiogenic sprouting, and endothelial-blood interactions. To further improve the overall vascularity of the µVs, we incorporated additional hESC-ECs in the interstitial collagen to induce tubulogenesis and anastomosis with the patterned µV.

3.3. Scientific Methods

3.3.1 Generation of wt, GFP-, and mTm- human stem cell derived endothelial cells

Unless otherwise specified, experiments used cells derived from wildtype or genetically modified RUES2 (Rockefeller University, NIH 0013) human embryonic stem cells (hESCs) that contained a dual-reporter (mTmG-2a-Puro) transgene [159]. All undifferentiated cells were maintained in colonies on Matrigel (BD Biosciences) coated plates with mouse embryonic fibroblast conditioned media (MEF-CM) supplemented with 5 ng/mL human basic fibroblast growth factor (hbFGF) (Peprotech) [115]. To generate a stable GFP stem cell line, mTmG-2a-Puro hESCs were treated with 5 µM de-salted Cre recombinase (TAT-Cre, Excellgen) for 24 hours to induce recombination and excision of TdTomato followed by two 24 hour doses of 5 ng/mL puromycin (InvivoGen) to purify the recombined population. GFP-expressing cells were expanded and analyzed for GFP purity using flow cytometry on unfixed and unstained cells. Untreated cells stably express tdTomato red fluorescent protein (mTm). Endothelial cells were differentiated as previously described [155,156]. Single cell suspensions of mTm- and GFP-expressing hESCs were obtained using enzymatic dissociation and re-plated at a density of 105K cells per cm^2 in MEF-CM + 5 ng/mL bFGF and 1 µM CHIR-99021 (Cayman Chemical). When the plated cells reached about 80% confluent monolayer,

they were fed with day 0 induction media: Activin A (R&D, 100 ng/mL - anterior ECs, 50 ng/mL – posterior ECs) in RPMI (Gibco, with L-glutamine) + B27 supplement (ThermoFisher, without insulin) and 1X Matrigel. 18 hours post induction, the cells were fed with BMP4 (R&D, 5 ng/mL – anterior ECs, 40 ng/mL – posterior ECs) and 1 µM CHIR-99021 in RPMI + B27 (without insulin). 24 hours later, the media was changed to endothelial induction media: Stempro34 (Invitrogen) containing 200 ng/mL VEGF (Peprotech), 5 ng/mL bFGF, 10 ng/mL BMP4, $4x10^{-4}$ M monothioglycerol (Sigma), 50 µg/mL Ascorbic Acid (Sigma), 2 nM L-Glutamine (Invitrogen) and pen-strep (Invitrogen). The cells remained in endothelial induction conditions for 72 hours, with no media changes. At the end of 72 hours (differentiation day 5), endothelial progenitor cells were harvested for re-plating and flow cytometry analysis. The cultures were fed with fresh Stempro (with L-glutamine and pen-strep) 1 - 2 hours prior to re-plating to improve survival and attachment. Cells were then enzymatically harvested to obtain a single cell suspension and re-plated in 0.2% gelatin coated tissue culture flasks with endothelial growth media (EGM, Lonza) containing 20 ng/mL VEGF (Peprotech), 20 ng/mL bFGF, and 1 µM CHIR-99021. An aliquot of day 5 days were stained with CD34 - APC FACs antibody (BD 555824, 1:4) and analyzed with flow cytometry to determine differentiation efficiency of endothelial progenitors. Re-plated cells were maintained in EGM with CHIR-99021, bFGF, and VEGF (EGM + Factors). In all experiments, hESC-ECs were harvested at differentiation day 12 – 14 and then used to generate engineered microvessels. Aliquots of differentiated cells were stained with CD31 – PE FACs antibody (BD 555446, 1:4) and analyzed with flow cytometry to determine endothelial purity. All staining for flow cytometry was done on live cells. Aliquots were washed in

PBS containing 5% FBS, resuspended in DMEM media (Corning) with conjugated antibody, and kept in the dark on ice for 45 min. Stained cells were washed and analyzed immediately with FACs Canto II cell analysis instrument and FlowJo Software.

3.3.2 Endothelial morphology and marker analysis in 2D.

Day 14 cells were grown to confluency overnight after re-plating at 100K/cm^2 on 0.2% gelatin coated coverslips. For comparison, passage 5 Human Umbilical Vein Endothelial Cells (HUVECs – Lonza #CC-2517) were plated at the same time and analyzed concurrently. Cells were fixed and stained for CD31, Ki67, and Von Willebrand Factor. Briefly, fixed cells were blocked in 2% BSA and 0.5% Triton X-100 in PBS for one hour followed by an overnight incubation with primary antibodies (Rb pAb to hCD31 (abcam 28364), Ms pAb to VECadherin (abcam 7047), and Rb pAb to Ki67 (abcam 16667)). Samples were washed with PBS and incubated with secondary antibodies for 1 hour at room temperature (Alexa Fluor 488 Phalloidin (Invitrogen A12379), Sh pAb to Von Willebrand Factor (abcam 8822), Alexa Fluor goat anti-mouse 647 (Invitrogen A21235), Alexa Fluor goat anti-rabbit 568 (Invitrogen A11011)) and counterstained with Hoechst 33342 (Sigma B2261). Images were acquired on a Nikon TiE inverted widefield fluorescence microscope. Proliferation was quantified by manually counting the percentage of Ki67 positive cells in anterior, posterior, and HUVEC populations.

3.3.3 Tubulogenesis and angiogenesis assays

Type I collagen was extracted from rat tails as previously described [102] and dissolved in 0.1% acetic acid at a concentration of 15mg/mL and stored at 4°C. Before use, collagen

gel was neutralized and diluted to its final concentration with 1M NaOH (20 mM final), EGM, and 10X M199 (Sigma M0650). *Tubulogenesis*: The gel was then mixed with day 14 cells at a density of $2x10^6$ cells/mL (final collagen concentration: 2mg/mL), pipetted into 4mm diameter well (10uL volume) of angiogenesis µ slides (Ibidi), and allowed to gel for 20 minutes at 37°C. Cultures were fed with EGM supplemented with 20ng/mL VEGF, 20ng/mL bFGF, and 1uM Chiron (EGM + factors) for 2 days, fixed, and stained for CD31 and Phalloidin. *Angiogenesis*: Day 14 endothelial cells were seeded on top of acellular 2mg/mL collagen disks (4mm D x 2mm H) at a density of 400 k/mL and fed with EGM + factors for 3 days. Samples were fixed and stained for phalloidin and CD31. Three dimensional z stack images of both angiogenesis and tube formation assays were acquired on a Nikon A1R confocal microscope. Maximum intensity projections and orthogonal views were obtained using Fiji software. Angiogenic sprouting was quantified by manually counting the number of sprouts extending downward from the monolayer and the average length of sprouts. The number of sprouts was normalized to the surface area of the monolayer (n: 3 biological replicates).

3.3.4 *Fabrication and culture of engineered microvessels*

A detailed protocol microvessel generation using injection modeling and soft lithography was previously published [102,103]. Briefly, collagen was neutralized and diluted to 6 mg/mL on ice as described earlier in this chapter. For experiments containing hESC-ECs in the bulk collagen, the cells were added after the collagen was neutralized at a density of 3×10^6 per mL, and the volume of EGM was adjusted accordingly to compensate for the additional volume of cells. Specially designed devices that contain
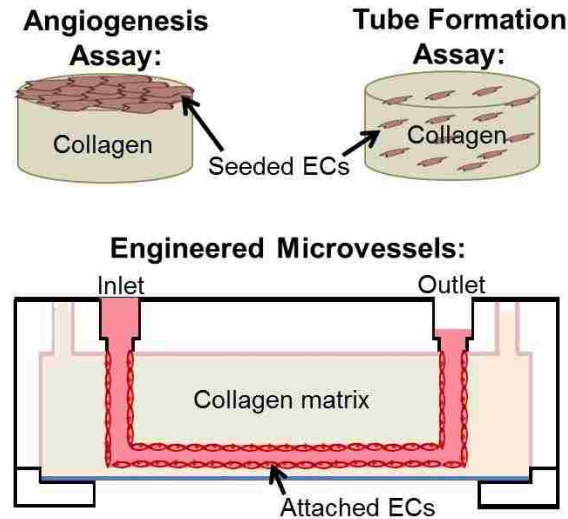
Figure 3.1 – Schematic of endothelial functional assays

holes for collagen injection, inlet, and outlet were used during injection molding, assembly, and microvessel culture. The microchannels were created by molding liquid 6 mg/mL collagen (acellular (µV only) or hESC-EC containing (µV+SA)) around a microfabricated polydimethylsiloxane (PDMS) stamp that contains vessel network geometry: 3 x 3 structure with 100 µm feature height was used to generate the network pattern. After gelation, the channel was enclosed with a separately generated flat layer of collagen to create embedded microfluidic channels surrounded by native collagen matrix on all sides. Day 14 mTm-hESC-ECS were seeded in the channel by perfusing at a density of 10×10^6 per mL. The cells were allowed to circumferentially attach overnight in static conditions followed by culture under gravity driven flow for 4 or 7 days with EGM + factors media. Gravity driven flow is generated by replacing the media at the device inlet every 12 hours for the duration of the culture period. These culture conditions generate sheer stresses on the order of $0 - 10$ dyne per cm^2 with a time average of 0.1 dyne per cm^2 and the highest sheer application immediately after media

replacement [102]. Basic schematics of the three endothelial function assays used in this chapter are illustrated in Figure 3.1.

3.3.5 Analysis of in situ *microvessel immunofluorescence and bead perfusion*

Engineered vessels were perfusion-fixed after 4 or 7 days in culture with 3.7 % formaldehyde (Sigma) for 20 minutes followed by 3x 20 min PBS washes. Samples were blocked in 2% BSA (Sigma) and 0.5% Triton X-100 (Sigma) in PBS for one hour followed by an overnight incubation with the following primary antibodies at 4°C: rabbit pAb to hCD31 (abcam 28364, 1:25), mouse pAb to VECadherin (abcam 7047, 1:50), rabbit pAb to DsRed (abcam 16667, 1:100), and goat pAb to GFP (abcam 5450, 1:400). One hour incubation with the following secondary antibodies, conjugated primary antibodies, and nuclei counterstains was performed at room temperature: sheep pAb to Von Willebrand Factor (abcam 8822, 1:100), donkey anti-goat Alexa Fluor 488 (Invitrogen A11055, 1:100), donkey anti-mouse Alexa Fluor 647 (Invitrogen A31571, 1:100), donkey anti-rabbit Alexa Fluor 594 (Invitrogen A21207, 1:100), and Hoechst 33342 (Sigma, 1:250). Three dimensional z stack images were acquired on a Nikon A1R confocal microscope with all image post processing and quantification done with ImageJ software. GFP-hESC-EC density and lumen size were quantified in μV + SA devices by applying a threshold to maximum intensity projections of the GFP channel followed by ImageJ particle analysis (particles less than 20 μm^2 in size excluded to account for background) within the specified distance ranges from the microvessels: [0 - 300 μm], [300 - 600 μm], and [600 - 900 μm]. Endothelial sprouts were quantified with either DsRed stained microvessels (μV + SA) or CD31 stained microvessels (μV only)

to determine sprouting from the patterned microvessel since GFP-hESC-ECs also express CD31. Sprouts were manually counted and their lengths and diameter measured using 3D orthogonal views and z-stack images in ImageJ. The number of sprouts was normalized to the surface area of the endothelium. After all confocal images were collected, vessels were perfused with 1.0 µm red fluorescent beads (Thermo Fisher F13083, 1×10^{10} beads per mL, 580/605) diluted 1:30 in PBS. Brightfield and fluorescent time series were collected with no delay at 10X magnification on a Nikon high resolution wide-field microscope. Bead velocity was quantified with ImageJ using manual particle tracking in both sprouts and the patterned microchannel (D > 100 µm). Perfusion area was quantified by measuring the total area of perfused beads in large images that were manually stitched together with ImageJ software from smaller 10X. For each vessel, the stitched image encompassed a field of view twice the area of the original pattern boundary.

3.3.6 *Whole blood perfusion and analysis of platelet accumulation*

Fresh blood (in 0.129 M sodium citrate) was obtained through Puget Sound Blood Center under University of Washington Institutional Review Board (IRB) approved protocols from consenting healthy donors. The blood was labeled with FITC-conjugated CD41a antibody (BD 555466) for 20 min at room temperature to label platelets followed by immediate perfusion through the PBS-washed live microvessels at sheer stresses between 10 and 30 dyne per cm^2 for 15 to 30 minutes. All blood perfusion experiments were done in mTm-hESC-EC seeded microvessels that were cultured for 4 days. Brightfield and fluorescent no delay time series were collected at 10X magnification on a

Nikon high resolution wide-field microscope to visualize red blood cell movement and platelet accumulation of the vessel walls. Platelet adhesion was quantified by measuring the area of CD41+ signal over time and normalizing to vessel wall surface area.

3.4 Results

***3.4.1** Anterior and posterior derived ECs display proper endothelial morphology*. Previous work by Dr. Palpant demonstrated that anterior and posterior derived endothelial cells exhibited marker expression consistent with endothelial development. Day 5 cells were greater than 90% CD34+/KDR+ purity and greater than 75% KDR+/VE-cadherin+, while unsorted cells grown out to day 14 were greater than 95% CD31+ suggesting that endothelial growth conditions selectively enrich for purified EC populations [155]. We analyzed endothelial junction morphology of cells that were
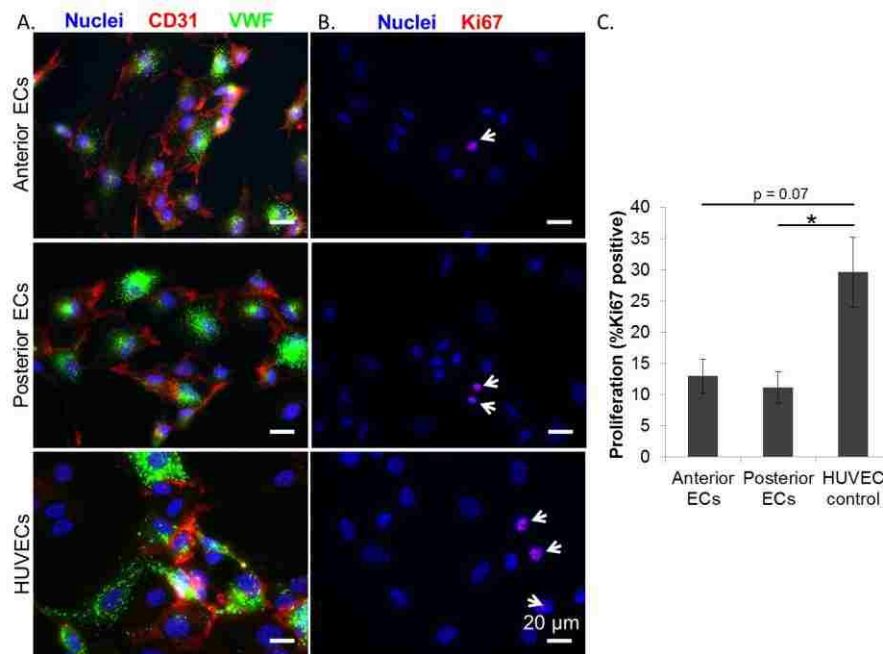

Figure 3.2 – 2D characterization of endothelial marker expression and proliferation. (A) Immunohistochemical staining of CD31 junctions (red), vWF granules (green), and Hoechst (blue). (B) Ki67 staining (red) and (C) proliferation quantitation [N: biological replicates (# of scored cells) = 3(302), 3(246), and 2(252), respectively].

differentiated and maintained in endothelial favorable conditions for two weeks and found that both anterior and posterior derived ECs expressed junctional endothelial CD31 and contained Von Willebrand Factor granules in 2D immunohistochemistry assays demonstrating morphological similarity to mature endothelial cells, such as HUVECs (Fig 3.2A). Staining for Ki67, a cellular marker for proliferation, revealed little difference between the two EC types (Fig 3.2B). Both stem cell derived ECs had fewer Ki67 positive cells compared to HUVECs although this difference is only significant for the posterior derivatives (Fig 3.2C). No significant differences between anterior and posterior ECs were observed in these assays.

3.4.2 hESC-ECs can be generated from multiple stem cell lines.

To assess the consistency of obtaining definitive endothelial cells from stem cell sources, we assessed endothelial CD31 expression of day 12 anterior and posterior derived ECs differentiated from four stem cell lines. In identical differentiation conditions, only the human embryonic stem cell line RUES2, but not Elf1, yielded proper endothelial cobblestone morphology with expression of junctional CD31 (Fig 3.3A). Likewise, of the induced pluripotent stem cell lines tested, only IMR90, but not VN1, resulted in junction formation and characteristic cobblestone phenotype (Fig 3.3B). Our success in generating both anterior and posterior ECs from IMR90 iPSCs in addition to the RUES2 hESCs confirmed that our differentiation protocol for stem cell derived endothelial cells is applicable for multiple cell lines, including induced pluripotent stem cells. However, additional modifications (i.e. factor concentrations, induction timing, etc.) will be required for robust EC generation from multiple cell lines.
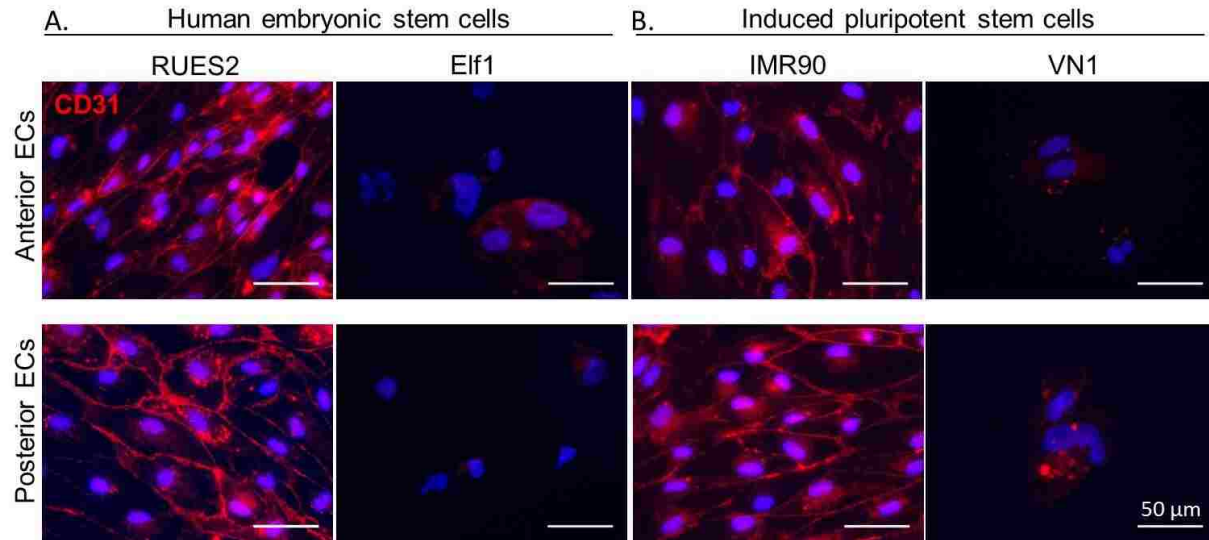
Figure 3.3 – EC generation from multiple stem cell lines. Morphological characterization of endothelial cells derived from alternative stem cell sources. CD31 junction (red) and Hoechst (blue) immunohistochemistry of ECs from (A) human embryonic stem cell lines, RUES2 and Elf1, and (B) induced pluripotent stem cell lines, IMR90 and CEM.

3.4.3 *Anterior and posterior derived hemogenic endothelium yield functionally distinct endothelial cells.*

A fundamental function of a definitive endothelial cell is its ability to undergo tubulogenesis or form lumens within 3D matrix. Tube assays are consequently a common way to assess endothelial function and study vascular phenomena such as vessel maturation, stabilization, and basement membrane deposition [160]. The tube formation proficiency of both anterior and posterior derived ECs was evaluated by culturing the cells in a 3D type I collagen matrix for two days which is sufficient for lumen formation. Both cell types formed tubular structures in the collagen matrix (Fig 3.4A). Importantly, we found that both anterior and posterior derived networks contained open lumens (Fig 3.4A, XY view) although these lumens contained limited organization with no hierarchical structure as expected.
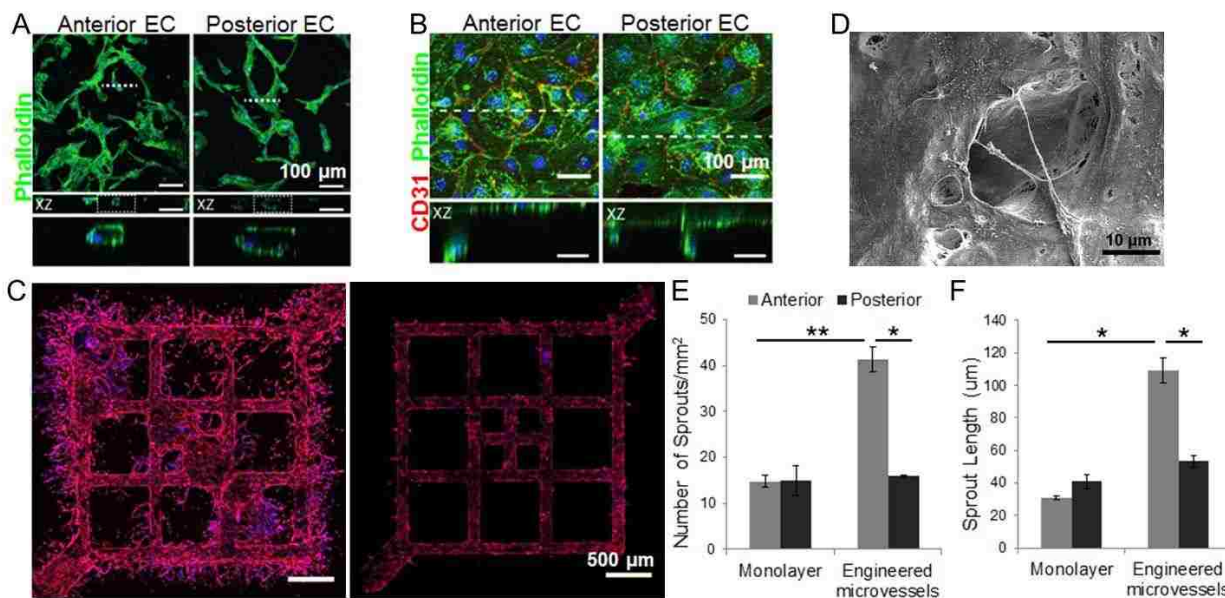
Figure 3.4 – 3D functional demonstration of hESC-ECs. (A) Tube formation assay: confocal image of Phalloidin (green) and Hoechst (blue) (top panel) with orthogonal views (middle panel) and zoomed in orthogonal view (bottom panel). (B) Monolayer angiogenesis assay with orthogonal view below: confocal images of Phalloidin (green), CD31 (red), and Hoechst (blue). (C) Engineered vessels seeded with either anterior (top) or posterior (bottom) ECs. Confocal large image z-stack projection with CD31 (red) and Hoechst (blue). (D) Scanning electron microscope image of anterior EC seeded microvessel. (E) Quantitation of number of sprouts normalized to lumen surface area (#/mm^2) and (F) the average sprout length (μm). (D-E) N: 3 biological replicates (*$p<0.05$; **$p<0.01$)

To further assess endothelial function, we performed monolayer angiogenesis assays and evaluated the number and length of sprouts extending into the collagen matrix from the monolayer. We found that both anterior and posterior derived cells have similar but mild angiogenic sprouting capacity in these static conditions (Fig 3.4B). Endothelial cells are known to respond to different environmental conditions such as matrix composition [161], shear stress [162], and biochemical factors [163], and conventional assays such as tubulogenesis and monolayer angiogenesis for assessing endothelial function, while informative, are not ideal. We therefore generated engineered μV with both anterior and posterior derived ECs to simulate a more physiological environment

with 3D lumen geometry and laminar flow. Both anterior and posterior ECs formed intact perfusable vessels in this microfluidic platform with robust expression of junctional CD31 (Fig 3.4C). Interestingly, the presence of shear stress (ranging from 0.1-10 dynes/cm^2) in the engineered microvessel platform resulted in an increase in the number and length of angiogenic sprouts in microvessels seeded with anterior ECs compared to monolayer angiogenesis assays and microvessels seeded with posterior ECs (Fig 3.4E-F). Through scanning electron microscopy, we further characterized the anterior EC µVs and detected open sprouts from the inside of the µV lumen (Fig 3.4D).
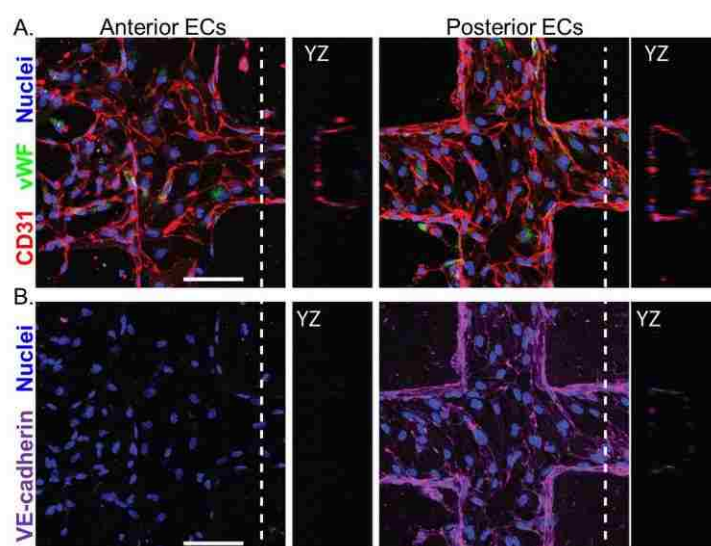
Figure 3.5 – Additional junctional staining of ECs in µVs. Confocal image of engineered microvessels with anterior EC (left) or posterior EC (right). Z-stack projections with corresponding YZ orthogonal view displayed to the right stained with (A) CD31 (red), vWF (green), and Hoechst (blue) or (B) VE-cadherin (magenta) and Hoechst (blue). Scale bar: 100 µm.

We analyzed engineered microvessels for expression of VE-cadherin in addition to CD31 junctional staining and found that only posterior derived microvessels expressed junctional VE-cadherin consistently, while both anterior and posterior ECs showed consistent CD31 expression (Fig 3.5) suggesting molecular differences between the two derivatives that contributed to their distinct flow responses. Taken together, these results demonstrated that we are able to generate definitive, functional endothelial cells from stem cell sources.

3.4.6 *Angiogenic and tubulogenic vascular remodeling in human stem cell derived engineered vasculature.*

For the remainder of this aim, we focused entirely on anterior-derived endothelial cells, abbreviated hESC-ECs for simplicity, due to their angiogenic potential. Given their high angiogenic nature human engineered µVs, we sought to utilize their functionality to promote further anastomosis and increased vascularity *in vitro* by including hESC-ECs in the surrounding interstitial collagen matrix. In order to distinguish hESC-ECs seeded in the µV from hESC-ECs seeded in the collagen, we first generated endothelial cells from a dual reporter RUES2 human stem cell line (mTmG-2a-puro RUES2 [159]) that stably express either TdTomato red fluorescent protein or GFP following Cre-mediated recombination (Fig 3.6A). Both mTm- and GFP-hESCs differentiated into day 5 progenitor populations with greater than 50% purity as seen by CD34 expression, a surface marker expressed by both hematopoietic and endothelial populations (Fig 3.6B) [164]. Importantly, long term GFP expression was observed in recombined cells after differentiation (Fig 3.6B). After an additional week in endothelial culture conditions, endothelial populations arose with greater than 98% purity by day 14 as shown by flow cytometry with endothelial junction protein, CD31 (Fig 3.6C). Engineered µV were generated with mTm-hESC-ECs comprising the channel-lining endothelium and GFP-hESC-ECs embedded in the surrounding collagen matrix (Fig 3.7A). mTm-hESC-ECs formed intact patent µVs that retained the original patterned geometry (Fig 3.7B) and exhibited high angiogenic activity (Fig. 3.7C-D). GFP-hESC-ECs underwent tubulogenesis to form self-assembled (SA) lumens in the surrounding collagen matrix, some of which integrated and formed anastomotic connections with sprouting mTm-

hESC-ECs (Fig 3.7E-F and SV6). In addition to anastomosis between SA lumens and the outgrowing endothelial sprouts, GFP-hESC-ECs integrated with the µV by directly connecting newly formed lumens to the patterned µV, and by migration and incorporation of single cells into the endothelial wall of sprouts and µV pattern (Fig 3.7F). These data demonstrate that engineered µVs can be combined with standard
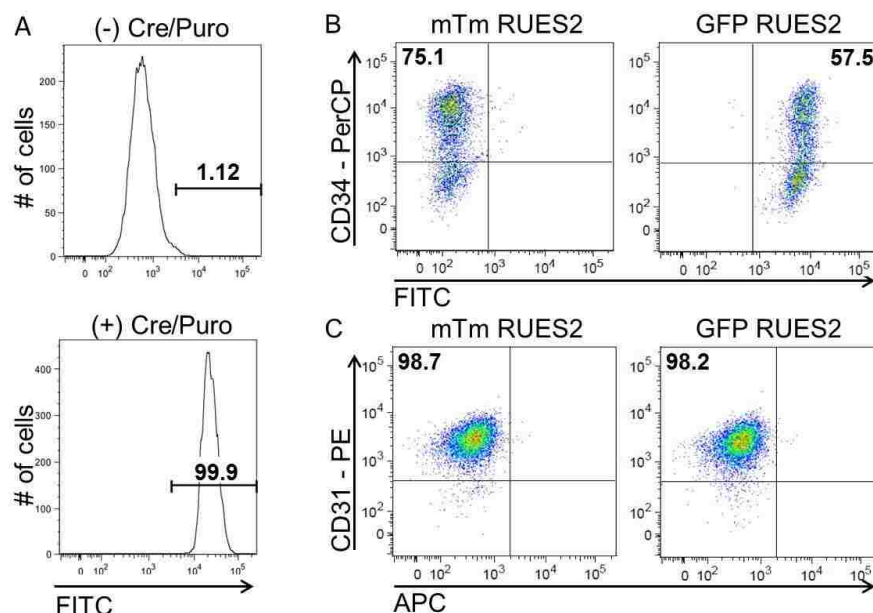
Figure 3.6 – Generation of mTm- and GFP- hESC-ECs. (A) Dual fluorescent reporter stem cells that express GFP after Cre recombinase treatment. FACs analysis of (B) CD34 expression in Day 5 progenitors and (C) CD31 expression in Day 14 endothelial cells.

endothelial tubulogenesis principles to generate highly vascularized constructs with both capillaries and small arteriole conduits. Endothelial plasticity, in particular endothelial to mesenchymal transition (EndoMT), is a hallmark of endothelial behavior that plays a large role developmentally [165], but can also result in drastic phenotypic changes in endothelial cells in 2D tissue culture that are not representative of the cells phenotype *in vivo* [166]. We evaluated expression of additional markers associated with definitive mature endothelial cells to assess hESC-EC behavior in µV culture and ensure a continued endothelial phenotype. Expression of endothelial junctional proteins, vascular endothelial cadherin (VE-cadherin) and platelet endothelial cell adhesion molecule

(PECAM-1 or CD31), as well as Von Willebrand factor (VWF) was observed (Fig 3.8A) suggesting the seeded endothelial cells maintained endothelial phenotype for the duration of the culture period.
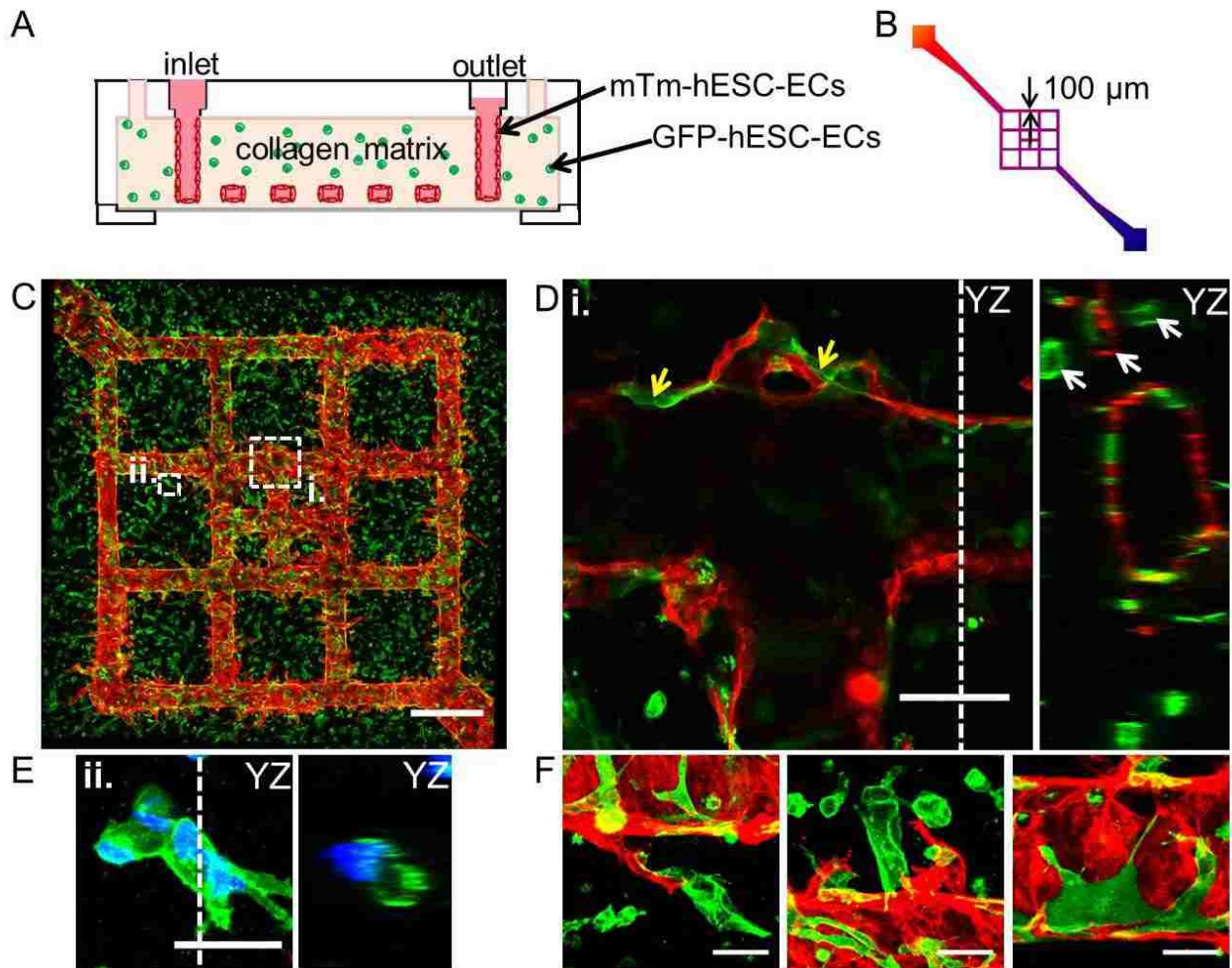
Figure 3.7 – In vitro anastomosis between mTm-hESC-EC engineered microvessels and GFP-hESC-EC self-assembled (SA) lumens (µV + SA). Staining: dsRed (red) and GFP (green) to detect mTm- and GFP- expressing hESC-ECs, respectively. (A) Device schematic. (B) Network structure. (C) Confocal large image and maximum intensity projection (MIP) of a µV + SA construct cultured for 4 days. Scale bar: 500 µm. (D) High magnification view of region (i) from panel C at a single z location (left) and a YZ orthogonal view (right) at the section depicted by the dotted white line. The arrows depict open GFP+ lumens (white) and sites of GFP-hESC-EC integration with the vessel wall (yellow). Scale bar: 100 µm. (E) High magnification MIP (left) of GFP-hESC-EC lumen from region (ii) in panel C with corresponding orthogonal view (right). Scale bar: 50 µm (nuclei, blue) (F) High magnification MIP images of GFP-hESC-ECs associated with mTm-hESC-EC patterned vessel. Scale bar: 50 µm.
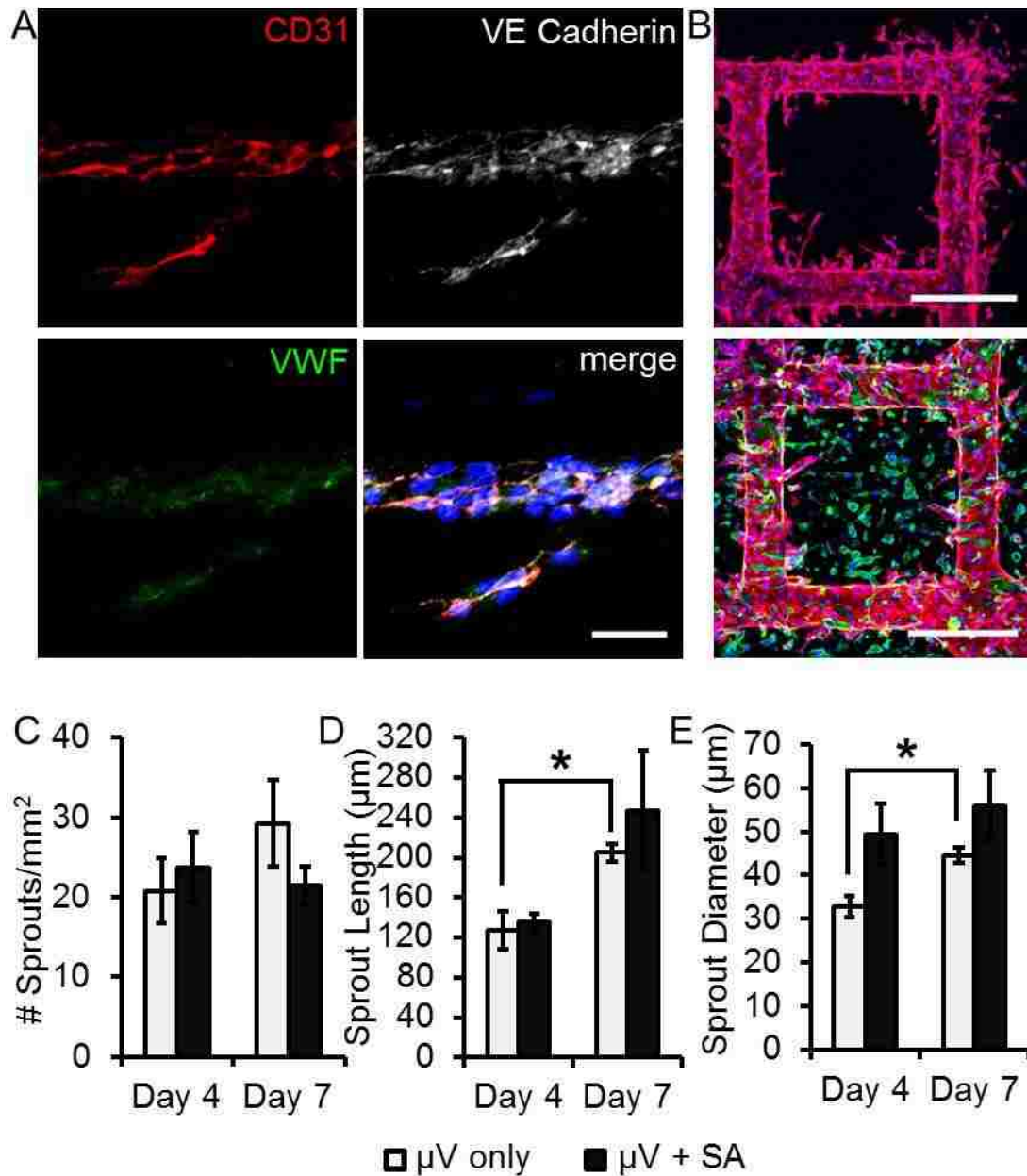
Figure 3.8 – Assessment of endothelial sprouting in patterned µVs with and without surrounding GFP-hESC-ECs. (A) MIP image from a µV only device of an endothelial sprout expressing CD31 (red), VE Cadherin (white), and von Willebrand factor (VWF) (green). Hoechst-stained nuclei are shown in blue. Scale bar: 50 µm. (B) Maximum intensity projection (MIP) image of immunofluorescent confocal z-stacks of day 4 (top panel) µV only and (bottom panel) µV + SA devices stained for DsRed and GFP to detect mTm- and GFP-hESC-ECs, respectively. Hoechst-stained nuclei are shown in blue. Scale bar: 500 µm. (C-D) Quantitation of sprouts from patterned microchannels at day 4 and 7 of µV only (N = 6, 4) and µV + SA (N = 7, 3). (C) The number of sprouts per vessel surface area. (D) Average sprout length. (E) Average sprout diameter.

To assess how hESC-ECs in engineered µVs remodel over time and to determine if the presence of surrounding SA lumens induces functional changes in the seeded hESC-ECs, we generated mTm-hESC-EC-seeded µVs fabricated with acellular collagen (µV only) and compared them to mTm-hESC-EC-seeded µVs with surrounding GFP-hESC-ECs (µV + SA) (Fig 3.8B). While hESC-ECs remodel extensively and sprout into the collagen matrix, the overall number of sprouts per vessel surface area was not found to be significantly different between µV only and µV + SA groups or from day 4 to day 7 in culture (Fig 3.8C). The sprout length and diameter, however, increased over time between 4 and 7 days of culture in µV only devices, with an overall increasing trend in both sprout length and diameter in the µV + SA devices over time and compared to µV only (Fig 3.8D-E). This suggests that the surrounding GFP-hESC-ECs may help establish and stabilize endothelial sprouts.

By analyzing SA lumen density as a percentage of occupied area and average lumen size, we found that GFP-hESC-EC morphology declined with increasing distance from the µV wall in µV + SA devices (Fig 3.9A–C). GFP-hESC-ECs were analyzed in three defined regions: from 0 to 300 µm, 300 to 600 µm, and 600 to 900 µm from the vessel wall. SA lumen density significantly decreased with increased distance from the µV after 7 days in culture with a clear decreasing trend after just 4 days (Fig 3.9F). The average size of SA lumens that were near the vessel wall (within 300 µm) was significantly larger than lumens greater than 600 µm from the wall after 4 and 7 days of culture (Fig 3.9B). These findings suggest that the patterned µV helps sustain the survival and promotes better formation of SA lumens within a certain distance that is compatible with known diffusion limits in collagen.
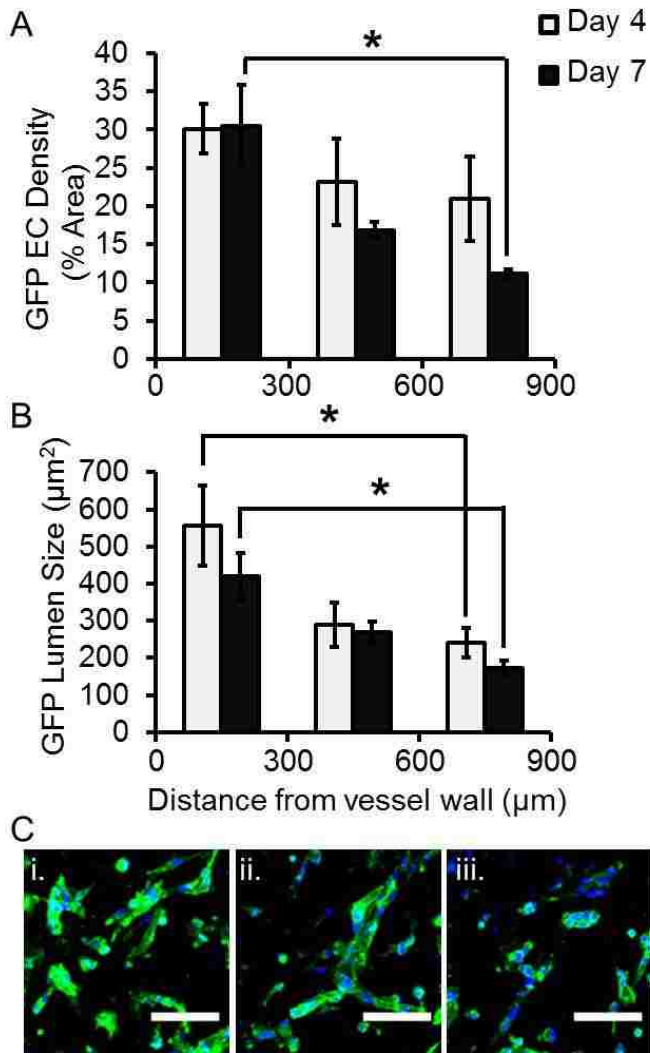
Figure 3.9 – Engineered µV influence on surrounding lumens. (A-B) Quantification of (A) GFP EC density expressed as percent area and (B) GFP lumen size in relation to proximity to the patterned vessel in day 4 and day 7 µV + SA devices. Data was quantified in at least three replicates at three distances from the vessel wall: 0 – 300 µm, 300 – 600 µm, and 600 – 900 µm (x-axis). (C) MIP images of GFP tubulogenesis (i) within 300 µm (ii) between 300 µm and 600 µm and (iii) between 600 µm and 900 µm from the vessel wall (GFP, green; nuclei, blue; scale bar: 100 µm). (statistical significance: * $p < 0.05$).

3.4.7 *In vitro perfusion analysis of engineered microvessels and angiogenic sprouts*.

We analyzed the patency of engineered µVs and endothelial sprouts by performing fluorescent bead perfusion experiments on µV only and µV + SA devices. Perfused beads immediately filled the endothelial-lined patterned microchannels and began to fill endothelial sprouts (Fig 3.10A and SV7). To better characterize the perfusion dynamics of the µVs, the beads were manually tracked and the velocity calculated for flow in endothelial sprouts and in the main µV channel (Fig. 3.10A–C). Bead velocity
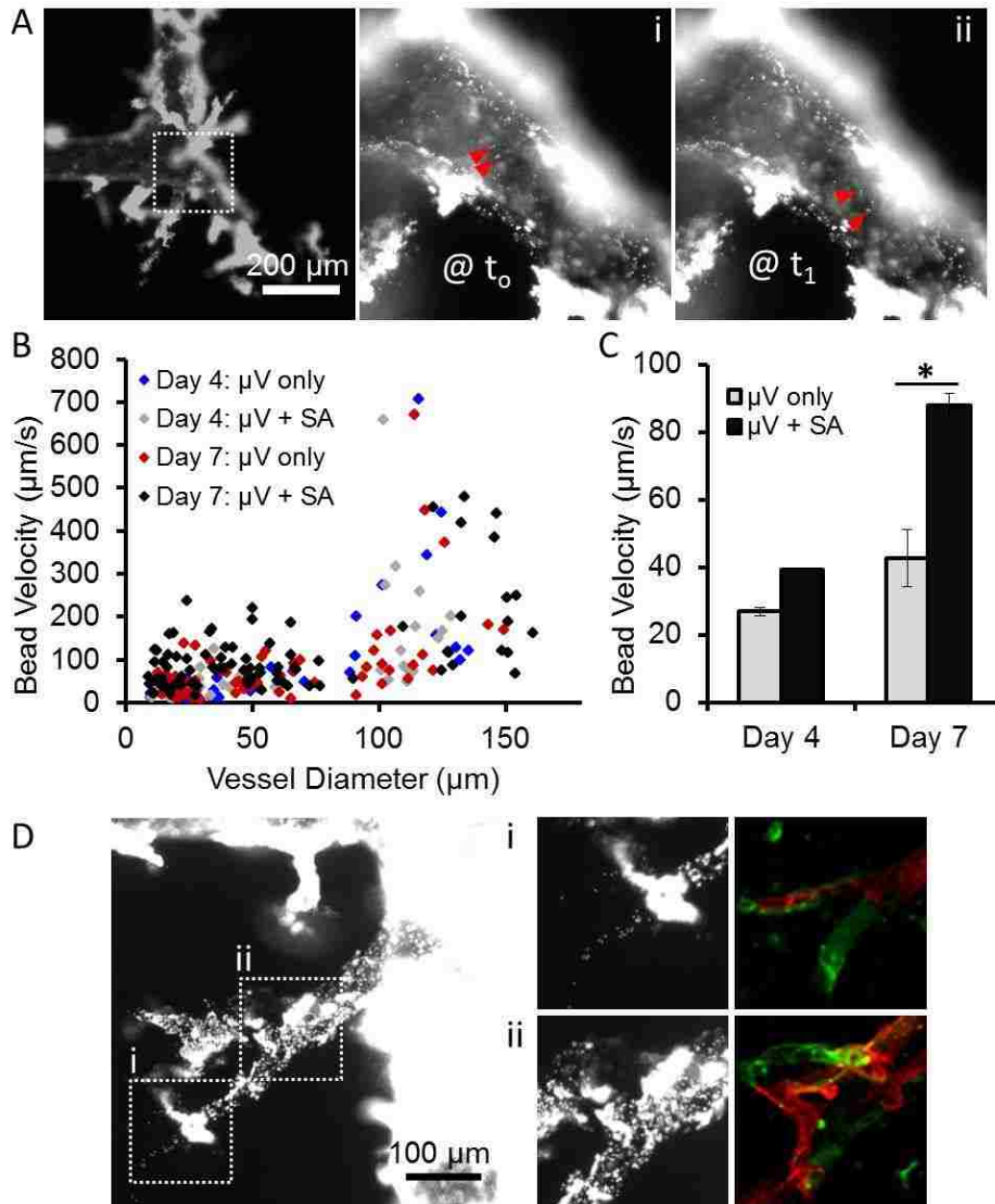
Figure 3.10 – Bead perfusion analysis of µVs with (µV + SA) and without (µV only) self-assembled GFP ECs. (A) Example image of sprouts filled with the perfused fluorescent beads within µV only device. An enlarged view of the outlined region in panel A is shown at two timepoints, t_o (i) and t_1 (ii), 0.27 seconds apart. Red arrows track the movement of fluorescent beads used to calculate velocities. (B) Quantification of bead velocity distribution shown in relation to vessel diameter. (C) Average bead velocity for sprouts with diameter less than 50 µm at day 4 and day 7 for both groups. (D) Example image of perfused sprouts/vascular connections in a µV + SA device. High magnification views of regions (i) and (ii) of panel D with corresponding in situ staining for mTm hESC-ECs (DsRed +, red) and GFP hESC-ECs (GFP +, green). N = 2-4 per group. (statistical significance: * $p < 0.05$).

was plotted in relation to vessel diameter to display the overall increase in velocity with increased velocity diameter although the spread of this data was quite high. The high variation in the velocity of the µV channel is likely due to differences in the diameter of the µV channel (diameter > 100 µm) which can be attributed to experimental variation during microvessel fabrication and endothelial remodeling of the collagen. For sprouts with diameter less than 50 µm, the average bead velocity was significantly higher in day 7 µV + SA devices which was measured at 87.9 ± 5.6 µm/s compared to 42.6 ± 8.4 µm/s in day 7 µV only devices (Fig 3.10C). Velocities in the main µV channel of day 7 µV + SA and µV only devices were not statistically different at 259.9 ± 59.3 µm/s and 215.1 ± 91.33 µm/s, respectively. In subsequent immunofluorescent imaging, perfused
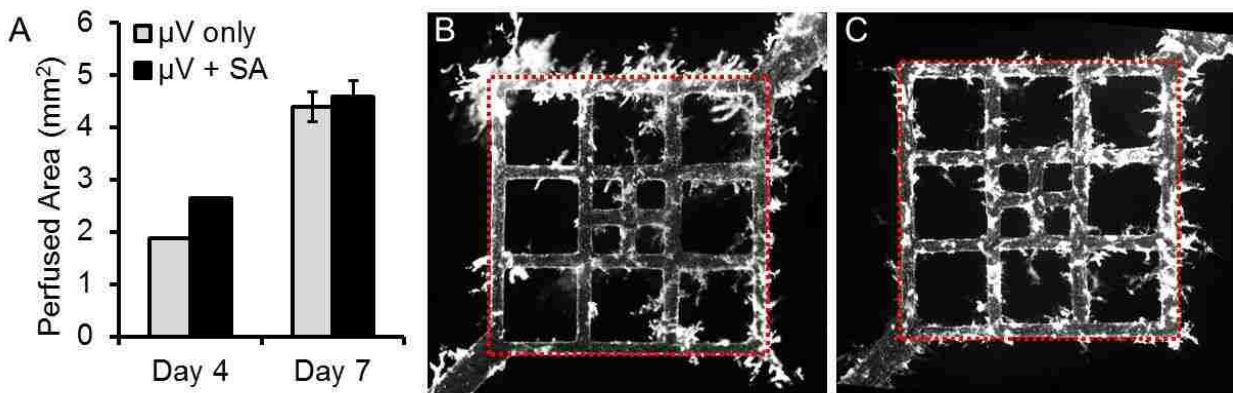
Figure 3.11 – Total perfused area with and without anastomosis. (A) Quantification of perfused area (mm^2) in bead perfusion experiments for µV only and µV + SA constructs at day 4 (N = 1,1 respectively) and day 7 (N = 3,2). Large images were manually stitched together with ImageJ software using smaller 10X images of each vessel for both (B) µV only and (C) µV + SA groups. For each vessel, the stitched image encompassed a field of view twice the area of the original pattern boundary (shown in red) or 40% greater in each direction.

sprouts that composed both GFP positive SA lumens and mTm positive µV sprouts were identified suggesting that sites of anastomosis between the SA lumens and the patterned µV were patent and perfusable (Fig 3.10D). Despite these perfusable

connections, the overall perfused area of the constructs was not significantly different in µV + SA devices compared to µV only devices (Fig 3.11A-C) suggesting that the anastomotic events between SA lumens and the patterned µV were not yet sufficient to create an overall more perfused tissue.

3.4.8 *Human stem cell-derived engineered microvessels are non-thrombogenic.* To investigate the interaction between blood and hESC-EC-derived engineered µVs, we perfused citrate-stabilized whole blood. The perfused blood immediately filled the patterned µV with subsequent perfusion of the endothelial sprouts (SV8 and SV9). In cases where sprouts connected two different regions of the patterned vessel, usually near corners, individual red blood cells were seen flowing through (Fig 3.12A and SV9). Importantly, red blood cells did not clump or adhere to the vessel and could be completely washed out of the vessel without obstructing flow (Fig 3.13A). Labeled platelets (platelet-specific glycoprotein IIb, or integrin αIIb (CD41a) positive) were used to visually track thrombi formation and platelet adhesion on the vessel wall. We found that platelets did adhere to the vessel wall of engineered µVs but thrombosis did not occur (Fig 3.12B and SV10). The average platelet adhesion in three µVs during the first three minutes of perfusion was quantified and found to be 1.07 ± 0.33 %, 1.14 ± 0.30 %, and 1.12 ± 0.11% at 1, 2, and 3 minutes, respectively which suggests that no significant increase in platelet accumulation and aggregation occurred (Fig 3.13B). Furthermore, the extent of platelet accumulation remained low (around 2 - 3% of the vessel wall surface area) in vessels perfused for longer than 10 minutes (Fig 3.12B-C). In a separate device, blood was perfused for an additional 8 minutes to demonstrate the
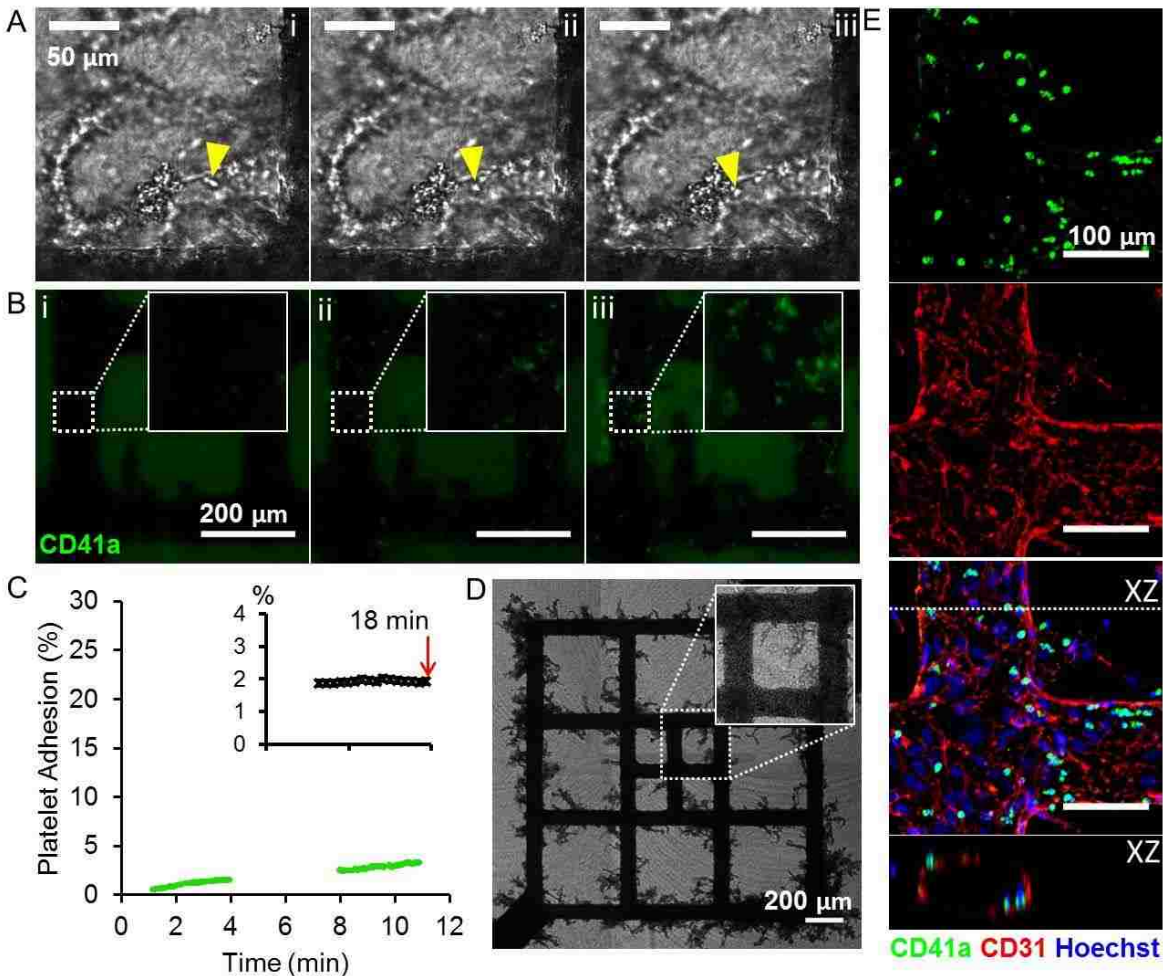
Figure 3.12 – Whole blood perfusion of hESC-EC µVs. (Ai-Aiii) Time sequence of red blood cell movement inside sprout. Total time difference between (i) and (iii): Δt = 2.88 s. Yellow arrowheads tracks the movement of a single red blood cell. (B) Time sequence of CD41a-labeled platelet (green) accumulation over time at (i) 1 min (60 s) (ii) 3 min (180 s) and (iii) 10 min (600 s). Insets show magnified regions of the vessel wall are shown (C) Quantification of platelet adhesion. Data is expressed as % of the vessel wall surface area. Inset: quantification of platelet adhesion in a separate device with longer time scale. (D) Brightfield stitched large image of patterned vessel perfused with red blood cells. (E) Maximum intensity projection of a confocal z-stack image of endothelium and adhered platelets after 30 minutes of perfusion. Immunofluorescent staining for endothelial junctions (CD31, red), integrin αIIb, (CD41a, green), and nuclei (Hoechst, blue).

continued low platelet accumulation which stabilizes at around 1.9% (Fig 3.12C, inset).

Overall, red blood cells moved through the patterned µVs freely, perfusing into sprouts

and filling the entire microvascular area demonstrating that the observed platelet

adhesion was minimal and not sufficient to induce thrombi formation (Fig 3.12D). Although platelets do not normally interact with quiescent endothelial cells at all, they have been shown to play a role in preventing hemorrhage in angiogenic vessels [167]. Indeed, subsequent immunofluorescent staining of blood-perfused µVs revealed that adhered platelets (CD41a, green) were localized to endothelial junctions (CD31, red) (Fig 3.12E) suggesting they may be facilitating junction repair of the actively remodeling and sprouting µV.
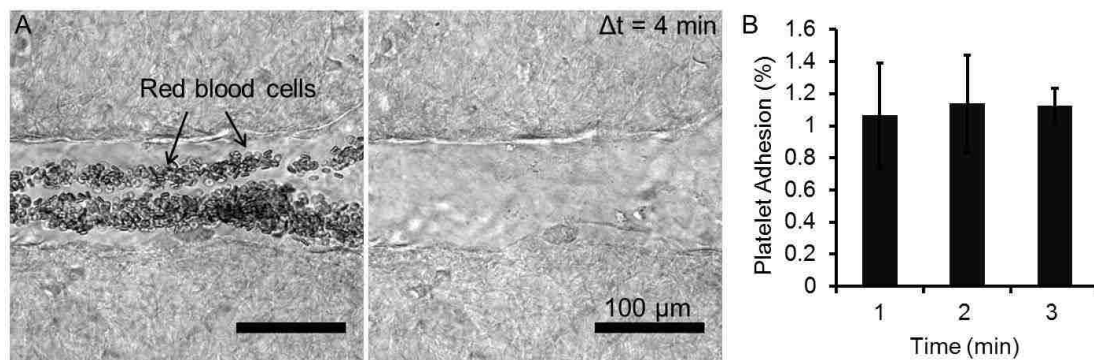
Figure 3.13 – Whole blood perfusion and washout. (A) Red blood cell perfusion through microvascular network (left) and red blood cell clearance after 4 minutes (right). (B) Average platelet accumulation as a percentage of the vessel wall surface area at 1, 2, and 3 min (N=3).

3.5 Discussion

Human pluripotent stem cells are a promising cell source for therapeutic applications, yet achieving efficient and specific cell fate specification is a major challenge. While robust cardiomyocyte differentiation has been achieved at high purities with comprehensive functional characterization [168–171], endothelial differentiation is less well established. Endothelial cells have previously been generated from pluripotent stem cells [172,173], but their characterization has been largely limited to FACs analysis of marker expression and basic tubulogenesis assays in matrigel. Furthermore, the

original paradigm that all endothelial cells are the same has gradually shifted as it's become clear that organ-specific and lineage-specific heterogeneity results in vast differences in endothelial morphology and their interactions with the tissue microenvironment [174–176]. Moving forward, the ability to differentiate endothelial cells with organ-specific phenotypes would have many implications in vascular regeneration therapies as well as in the study of vascular disease which are also known to be affected by endothelial heterogeneity [176].

Our findings that anterior and posterior derived hESC-ECs expressed key endothelial proteins (von Willebrand factor (VWF), VE-Cadherin, and PECAM-1/CD31) and displayed important functions such as tubulogenesis and angiogenesis provided substantial evidence that endothelial cells can be generated from specific mesoderm lineages with mature endothelial cell characteristics. In traditional tube assays, mature endothelial cells, such as HUVECs, rarely form networks with hierarchical structure or complete connectivity in the absence of additional physiological cues or guidance [100]. Although the formation of self-assembled tubes with the beginnings of hierarchical structure has been achieved by applying physiological pressure drops and interstitial flow [89], the lack of hierarchical structure formation in static conditions continues to hinder efforts to study endothelial behavior in 3D and in response to flow. To better characterize endothelial function, we fabricated engineered 3D microvascular networks with hESC-ECs and found that anterior- and posterior- derived cells formed patent endothelium with strong junction formation and robust angiogenic behavior. A key finding of this study was that when exposed to shear stress in engineered microvessels, anterior-derived and posterior-derived endothelial cells displayed functionally distinct

characteristics in terms of their angiogenic potential. Flow induced sprouting is consistent with a recent study that demonstrated increased angiogenesis in response to fluid shear stress [177], but the drastic difference between sprouting in anterior versus posterior derived microvessels was surprising. The idea that endothelial cellular response to shear is governed by an internal "set point" or threshold is an emerging theory [177] that could explain in part the differences observed here. Additionally, VE-cadherin is thought to be a part of a mechanosensory complex along with CD31 and VEFGR2 that modulates endothelial response to flow [162]. Further evidence that VE-cadherin junctions may play a role in suppressing angiogenic sprouting [178] is consistent with our findings that anterior-derived hESC-EC microvessels express VE-cadherin to a lesser degree.

To utilize the increased angiogenic nature of anterior-derived hESC-ECs, we generated engineered vasculature with high vascularity by incorporating interstitial tubulogenic hESC-ECs. This resulted in constructs containing large conduits for facilitating vascular perfusion, as well as capillaries to increase the overall vascular density of the grafts. Our finding that the interstitial hESC-ECs formed perfusable anastomotic connections with the patterned vasculature demonstrated the success of this approach, although the anastomotic connections were not sufficient to increase the overall perfused area yet. Further strategies to encourage additional remodeling could be employed such as continuous flow conditions, incorporation of perivascular cells, etc. In addition to connections between newly formed tubes and microvessel sprouts, some interstitial hESC-ECs were found to integrate directly into the vessel wall. Interestingly, endothelial progenitor cells have been shown to incorporate into active sites of

angiogenesis in animal models of ischemia [179], a mechanism which may have been at play in our experiments.

In normal healthy vasculature, the endothelium is non-adhesive and anti-thrombotic allowing blood to flow unobstructed throughout the body. Activated endothelial cells secrete adhesion proteins which initiate thrombosis [180] and are associated with the progression of many vascular diseases [43]. One of the early clinical concerns with vascular grafts, and in particular small diameter vessels, is the tendency for thrombosis to occlude the implant resulting in graft failure [181,182]. Endothelialization [183,184] and other chemical-based modifications [185,186] have been employed to prevent blood clot occlusion by rendering the surface non-thrombogenic, an essential characteristic of any graft intended to connect with host blood flow. Our studies to evaluate endothelial interactions with whole blood demonstrated that hESC-ECs are non-thrombogenic when exposed to direct contact with blood. We found that while some platelet adhesion did occur, the accumulation stabilizes over time at about 2% of the vessel wall area. This data is consistent with observed platelet adhesion in non-activated HUVEC-seeded µVs, which remained below 3% after 15 minutes of perfusion, whereas significant platelet adhesion was observed in PMA-activated HUVECs within the first few minutes of perfusion [102]. Collectively, this data demonstrates that anterior derived hESC-ECs form functional vascular networks *in vitro* with high vascularity, robust junction formation, sprouting angiogenesis and anastomosis, and important physiologic platelet interactions that render the endothelium non- thrombogenic. Moving forward, hESC-ECs may have great potential for successful application in vascular engineering and regenerative strategies.

Chapter 4.

Host integration of patterned vasculature with real time assessment of vascular perfusion using optical microangiography (OMAG)

Parts of this chapter were published in the following co-first authored manuscript: [187]

Note: maiden name – Roberts

- Qin, W.*, **Roberts, M.A.***, et. al. Depth-resolved 3D visualization of coronary microvasculature with optical microangiography. *Physics in Medicine and Biology* 61(21): 7536-7550. PMID: 27716639.

4.1 Abstract

Treatments that utilize regenerative strategies to replace damaged myocardial tissue have been the focus of many pre-clinical studies in small and large animal models. Progress in this area is hindered by the lack of revascularization of the scar and the slow and ineffectual vascular infiltration of implanted tissue grafts. Furthermore, while some efforts to assess vascular integration in this context have been made, dynamic graft perfusion analysis has not been done. Here, we developed a novel application of optical microangiography (OMAG) to image and quantitate vascular flow in tissue-engineered epicardial patches in a Langendorff perfused rat heart. OMAG is a Doppler based technique that distinguishes between moving and stationary particles and has previously been used extensively to visualize blood flow *in vivo.* We performed OMAG image acquisition during retrograde aortic perfusion of Intralipid to visualize coronary

vasculature with high resolution in hearts arrested in diastole and perfusion fixed. Increased perfusion pressure correlated to both an increase in the area density of perfused vessels and to an increase in signal intensity, which correlates to flux. To assess vascular perfusion and integration of vascular grafts, we implanted patterned and unpatterned microvascular constructs in a rat model of myocardial infarction. At day 5 post implantation, patterned microvessels had increased perfusion area and vessel area density compared to unpatterned controls, as well as an increase in flow velocities that were comparable to those in healthy myocardial regions. Histological detection of the grafts revealed that implanted human cells survived implantation and formed vascular lumens that contributed to the overall perfusion of the grafts. To our knowledge, this is the first demonstration of improved graft perfusion dynamics through the use of patterned vasculature in an injured heart model.

4.2 Rationale

Vascular integration is a vital aspect in the treatment of myocardial infarction with engineered tissues. Historically, efforts to vascularize tissue grafts have relied on angiogenesis from the host and the vasculogenesis of endothelial cells seeded alongside engrafted myocytes. Several studies have shown that while vessels originating from the host do infiltrate these cardiac grafts [70,78,116,123], hierarchical vasculature capable of efficiently transporting blood does not develop [107]. The process of arteriogenic remodeling from *de novo* lumens into a hierarchical connected network requires pre-existing vessels and is a complicated process that can take several weeks—much too long to satisfy the relative immediate perfusion needs of tissue grafts

[188]. To combat this problem, efforts to pre-fabricate perfusable arteriole-scale vasculature within tissue constructs have been extensively investigated in our lab and in others [105,189]. In addition to construct pre-vascularization, the feasibility and importance of direct anastomosis between the engineered vessels and host blood vessels has been demonstrated in two recent seminal studies, one that implanted vascularized cardiac tissue in the rat neck [189], and one in the hind-limb [190]. The beating heart, however, poses a major technical challenge and as such direct anastomosis with coronary vasculature has not been achieved. Although direct anastomosis would be ideal, there is some evidence that in the absence of establishing an immediate physical connection to host vessels, prior vascular organization in grafts can promote better overall integration [87,191]. Presumably, this effect may in part be owed to topographical cues that provide guidance to penetrating host blood vessels [83,101,192].

To further compound the difficulties of coronary vascular integration, most of the work that has been done in this field did not directly assess graft perfusion rates in real time. Rather, the degree of integration was evaluated in histological sections by the presence of red blood cells or the detection of perfused lectins or other dyes. While informative, these analyses were not able to determine whether the integrated vessels could effectively transport blood at physiological levels. Indeed, although blood has been detected in grafts vessels, some evidence suggests that perfusion rates in grafts of this nature are sluggish presumably due to a lack of hierarchical structure [107]. As vascular engineering strategies advance, it is essential that perfusion dynamics are assessed to extract more meaningful comparisons of relative effectiveness. Towards this end, we developed a novel application of optical coherence tomography (OCT)-

based optical microangiography (OMAG) to image real-time coronary perfusion in Langendorff- perfused and fixed rat hearts. With this technique, hearts fixed in diastole and perfused with Intralipid at physiologic pressures were used to obtain detailed images and flow dynamics of perfused vasculature. We further used this technique to demonstrate the vascular integration of hESC-EC microvessels with infarcted rat myocardium. Specifically, we show that patterned vasculature was able to more efficiently integrate with the rat host compared to unpatterned controls, and hESC-ECs survived implantation and connected to invading host vessels.

4.3 Methods

4.3.1 *Rat ischemia/reperfusion and vascular implantation.* All animal procedures in this study were approved by the University of Washington Institutional Animal Care and Use Committee (IACUC, protocol #2225-04) and performed in accordance with US NIH Policy on Humane Care and Use of Laboratory Animals. Male athymic Sprague-Dawley rats (approximately 250 g – 300 g) underwent two thoracotomy surgeries for ischemia/reperfusion injury (I/R) and implantation of vascular grafts (4 days post I/R). Subcutaneous administration of sustained release buprenorphine (1 mg/kg) provided analgesia for at least 2 days after all surgeries. The animals were closely monitored for 48 hours to provide post-operative care to ensure and maintain animal health and comfort as outlined in the IACUC protocol. Cyclosporine A (5 mg/kg) was administered subcutaneously for a total of 7 days beginning the day before implant surgery to prevent immune rejection. *Ischemia/reperfusion surgery*: The rats were anesthetized with an intraperitoneal (IP) injection of 68.2 mg/kg ketamine and 4.4 mg/kg xylazine. A second

dose of full strength ketamine/xylazine followed by additional ketamine boosts (20 mg/kg, administered as needed) were used to maintain a surgical plane of anesthesia. During the procedure, the rats were intubated, mechanically ventilated, and maintained on a water-circulating head pad. Core body temperature was monitored at regular intervals and maintained at 37°C. To induce myocardial infarction, the heart was exposed, and the left anterior descending (LAD) coronary artery was ligated and occluded for 60 minutes, followed by reperfusion and aseptic chest closure. *Vascular construct implantation*: patterned vascular constructs were made with anterior derived mTm-hESC-ECs in both the bulk collagen matrix (3 x 10^6 per mL) and seeded in the microchannel (µV + SA) as described in chapter 3. Control non-patterned constructs (SA) were made by mTm-hESC-EC suspension in 6 mg/mL collagen (3 x 10^6 per mL) followed by gelation in an 8 mm diameter x 1 mm height PDMS well. Constructs were cultured for 4 days *in vitro* to allow initial remodeling and anastomosis of angiogenic sprouts from the channels to de novo tubules from the bulk-seeded endothelial cells. On the day of implant surgery, the rats were anesthetized via inhalation of isofluorane at 5%. The rats were intubated and mechanically ventilated with continued isofluorane supplementation (3%) to maintain a surgical plane of anesthesia. Core body temperature was monitored at regular intervals and maintained with a water-circulating head pad at 37°C. Immediately prior to implantation, the constructs were carefully removed from their housing devices and placed in warm media bath. For µV + SA constructs, an 8 mm diameter biopsy punch was used to remove the 1 mm thick patterned region of the collagen gel from excess surrounding collagen. Additional 2 mm biopsy punches were created at the inlet and outlet to create structural conduits from

the network to the underside of the construct. The constructs were implanted on the epicardial surface of the left ventricle with 8-0 surgical suture at 3 to 4 points of contact. Once the implant was secured, excess blood was dabbed clean followed by aseptic chest closure.

4.3.2 Tissue harvest and retrograde perfusion fixation. At their experimental endpoint, the rats were euthanized with a chemical overdose of pentobarbital/phenytoin solution (Beuthanasia; 1.5 mL IP injection). Once the animals achieved deep anesthesia but while the heart was still beating, the chest was opened and 50U Heparin was intravenously infused via the inferior vena cava and allowed to circulate for 1-2 minutes to prevent thrombosis in the coronary vessels. Intravenous infusion with supersaturated potassium chloride (KCl) was then used to arrest the heart in diastole followed immediately with excision of the heart. The aorta was cannulated and attached to pressure perfusion apparatus (Fig 4.1A) followed by retrograde perfusion with a vasodilator buffer (PBS containing 4 mg/L Papaverin and 1 g/L adenosine) followed by 4% paraformaldehyde perfusion for 10 minutes. Perfusion pressure was maintained at ~100 mmHg. After perfusion fixation, the hearts were transferred to fresh fixative O/N at 4°C. After overnight fixation, the cannulated hearts were transferred to PBS buffer and transferred on ice for optical microangiography (OMAG) assessment of coronary flow.

4.3.3 OMAG assessment of vascular flow in grafts and normal healthy heart. To image vascular flow, the hearts were retrograde perfused with 10% Intralipid (Sigma) and imaged with optical coherence tomography- (OCT) based technology as previously

described [193,194]. During imaging, the hearts were placed on a custom-built imaging platform with rotational control and secured cannula to prevent tissue movement (Fig 4.1B). For optimization of the imaging protocol, perfusion pressures of 80 and 110 mmHg were used. For assessment of vascular grafts, perfusion pressure was maintained at a diastolic pressure of 90 mmHg throughout image acquisition. Two scanning protocols that covered the same 1.5 mm × 1.5 mm field of view were used to acquire data for both OMAG and OMAG based capillary velocimetry (OMAG-V). Both protocols shared the same system setup with conventional fiber-based spectral domain optical coherence tomography (OCT), which has been described in detail in a previous publication [109] (Fig 4.1C). Briefly, this section will describe the specific parameters that determined the system performance for imaging rat coronary vessels *ex vivo*. The light source was a super-luminescent diode (LS2000B, Thorlabs Inc.) with a spectral bandwidth of 110 nm at 3 dB, and operated at a center wavelength of 1340 nm. A 10X telecentric objective lens was adopted to focus the beam spot onto the heart sample with an incident light power of ~1.9 mW. The axial resolution was ~7 μm and the lateral resolution was ~ 7 μm in air. The maximal imaging speed of the system reached 92,000 A-lines per second, and the corresponding system sensitivity was ~100 dB in focus positioned at ~600 μm below the zero delay line. The system ranging depth was measured to be 3.5 mm in air.

For OMAG, raster beam scanning was performed to capture 250 A-lines within each B-frame (2D cross-section), 4,000 B-frames for each C-scan (3D volume), and 16 frame repetitions at each of the 250 A-line locations to achieve high vasculature contrast. A single 3D dataset was obtained in 15 seconds by using a frame rate of 280
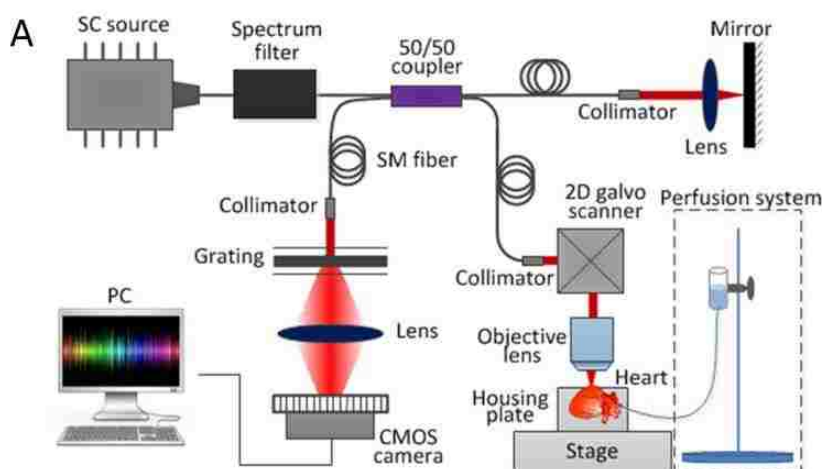
Figure 4.1 – OMAG schematic with Langendorff perfusion schematic. (A) Optical configuration. (B) Custom designed housing plate. (C) Pressure perfusion system.
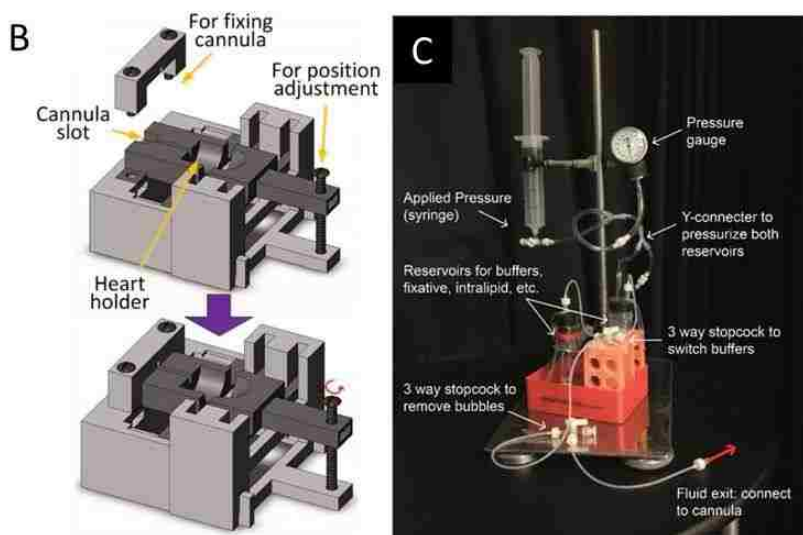
frames per second. Maximum intensity projections of the volumetric vasculature were used to calculate vessel density as a percentage of the imaging field of view.

For OMAG-V, 200 B-frames were captured in each C-scan. Within each frame, 10,000 A-lines were obtained that were comprised of 50 repeated A-lines at 200 positions. By utilizing a defined system speed of 20,000 A-lines per second, the 3D velocimetry data were acquired in 2.5 minutes. An inter-frame ultrahigh-sensitive OMAG algorithm [195] was utilized to extract 3D vasculatures from heart tissue structure images. By maximum intensity projection (MIP) of the volumetric vasculature, morphological

information of the microvascular network can be visualized from the top view. In order to quantitatively analyze the flow velocity in capillaries, Eigen decomposition (ED) statistical analysis was applied to the repeated A-lines as described in [196]. In brief, the repeated A-line ensembles were firstly stacked into a covariance matrix, and then this matrix was represented in terms of its eigenvalues and eigenvectors through diagonal factorization. Therefore, the frequency of flowing Intralipid particles can be calculated by the first lag-one autocorrelation of the eigenvectors [197]. Finally, the velocity of flow in vessels with diameters between 20 µm and 40 µm was assessed according to its linear correlation with the measured frequency [112]. Graft perfusion rates for the imaging field of view were calculated by multiplying the velocities with the perfused area and normalizing to the perfusion rates of the corresponding healthy region.

4.3.4 *Histological assessment of vascular grafts and lumen quantification.* Following OMAG imaging, the hearts were perfused with PBS to wash out remaining Intralipid solution followed by perfusion for 10 minutes with a 1:1 mixture of fluorescein labeled *Griffonia simplicifolia* lectin I (GSL I) isolectin IB4 (Vector Labs, 8 µg/mL) and rhodamine labeled *Ulex europaeus* agglutinin I (UEA 1) (Vector Labs, 8 µg/mL) in order to label the endothelial cells of perfused rat (GSL I positive) and human (UEA 1 positive) vessels. The hearts were flushed with PBS, and then sliced into 2 mm-thick sections for paraffin processing and embedding as previously described [58,115]. 4 µm sections were cut and stained for picrosirius red/fast green (to assess infarct size) or subjected to immunohistochemistry as described previously [58,59]. Briefly, slides were de-paraffinized and rehydrated followed by enzymatic antigen retrieval (EAR) with proteinase k (Roche,

15 µg/mL in 10 mM Tris/HCl) at 37°C for 20 minutes or heat induced epitope retrieval (HIER) for 20 minutes in boiling Tris/EDTA buffer, pH 9.0. The samples were blocked and permeablized with natural donkey serum (NDS) (Jackson, 10%) and 0.5% Triton X-100 followed by overnight incubation with primary antibodies: rabbit pAb to DsRed (Clontech, 1:75, EAR) to detect TdTomato reporter in mTm-hESC-ECs, rabbit pAb to hCD31 (abcam 28364, 1:50, HIER) to detect hESC-ECs, mouse mAb to smooth muscle actin (SMA) (abcam 7817, 1:100), goat Ab to GSL I (Vector AS-2105, 1:200), mouse mAb to rhodamine (ab 9093, 1:150), and mouse Ab to rat CD68 (Serotec, 1:100, EAR) to detect macrophages. For stains that required confocal microscopy, Alexa Fluor-conjugated secondary antibodies (Invitrogen) were used along with Hoechst (Sigma, 1:250) nuclei counterstain. For brightfield peroxidase detection of macrophages, a biotintylated goat anti mouse secondary antibody (Jackson, 1:00) was used in conjunction with Vectastain avidin/biotin complex (ABC) kit (Vector labs) and 3,3'-diaminobenzidine (Sigma) followed by routine hematoxylin counterstain to detect nuclei. The density and size of perfused lumens in vascular grafts were quantitated with custom Matlab code to analyze 20X confocal microscopy images of slides stained for DsRed, GSL I, or UEA I. Please note that while the lectins GSL I and UEA I are species specific in their endothelial binding affinity, the antibodies against them were not. Thus, anti GSL I stains were used to evaluate perfused lumens of both species, while stains for anti-rhodamine were used to detect perfused human vessels.

4.3.5 *Statistical analysis.* Unless otherwise noted, single variable analysis with student's t-test assuming unequal variance was used to determine statistical significance between

two samples. All results are presented as mean ± standard error. For *in vitro* microvessels, the sample number represents the number of devices analyzed. For *in vivo* experiments, the sample number per group represents the number of animals. Significance was defined as *p < 0.05 and ** p<0.01.
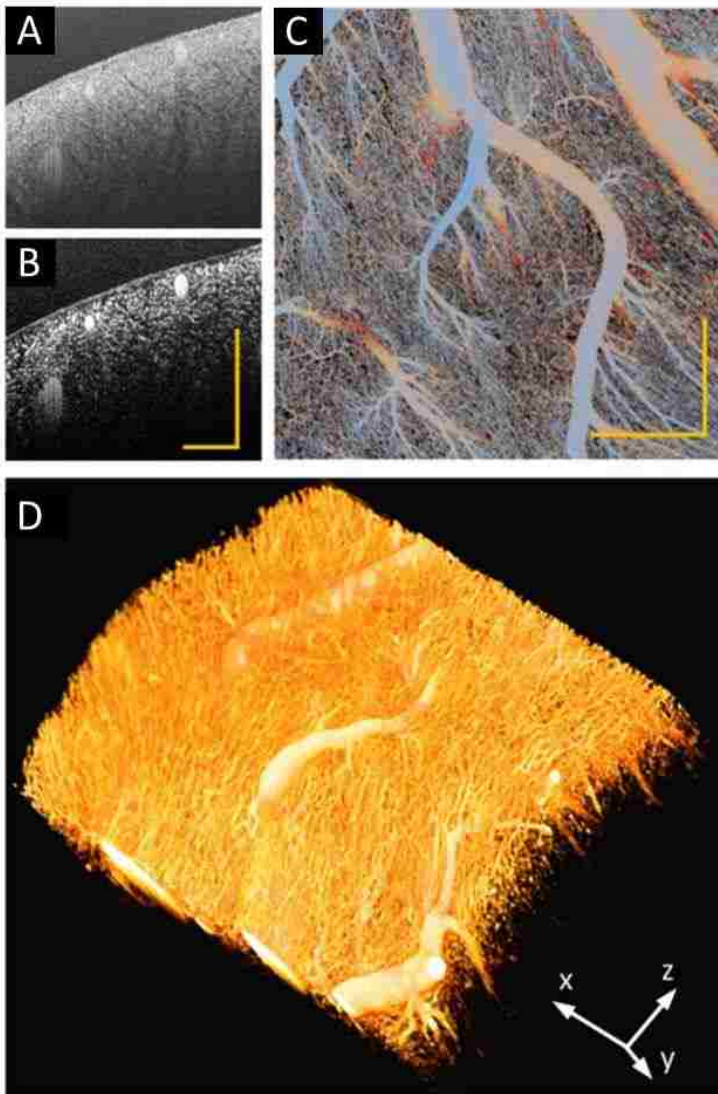
Figure 4.2 – OMAG imaging of coronary microvessels. Cross sectional images of OMAG (A) structure and (B) flow data. (C) Maximum intensity projection of OMAG flow with color coded depth – blue represents towards with heart surface and orange/red color represents increasing myocardial depth.(D) 3D reconstruction of OMAG flow data. Scale bars: 500 µm.

4.4 Results

4.4.1 Optical microangiography (OMAG) for coronary flow visualization.

Visualization of 3D coronary microvasculature is essential for coronary circulation research and will aid in the evaluation of revascularization strategies. To test OMAG imaging on *ex vivo*

hearts, we used fixed healthy rat hearts and retrograde perfused 10% Intralipid at a constant pressure of 110 mmHg. By utilizing custom OMAG data processing algorithms developed by Dr. Ruikang Wang and the members of his lab, the raw OCT data were separated into structural (heart tissue) and functional images (vascular flow) of the heart region (Fig 4.2A-B). Three dimensional processing of this data allowed us to visualize the depth from the heart surface of the vasculature (Fig 4.2C). Large arteries as well as expansive capillary beds were visualized near the surface (blue) as well deeper within the myocardium (orange/red). Additional 3D rendering of the OMAG data further illustrates the detailed morphological views that were obtained with this setup (Fig 4.2D). As expected from known myocardial structure, the coronary vasculature displayed a high degree of organization and alignment. Since coronary pressure drives coronary blood flow, we sought to determine how changes in pressure perfusion would affect vascular structures and signal intensity in OMAG images. OMAG data was collected at 80 and 110 mmHg for the same region of the myocardium. Qualitatively, densely-packed vasculature was observed at both pressures (Fig 4.3A-B), with
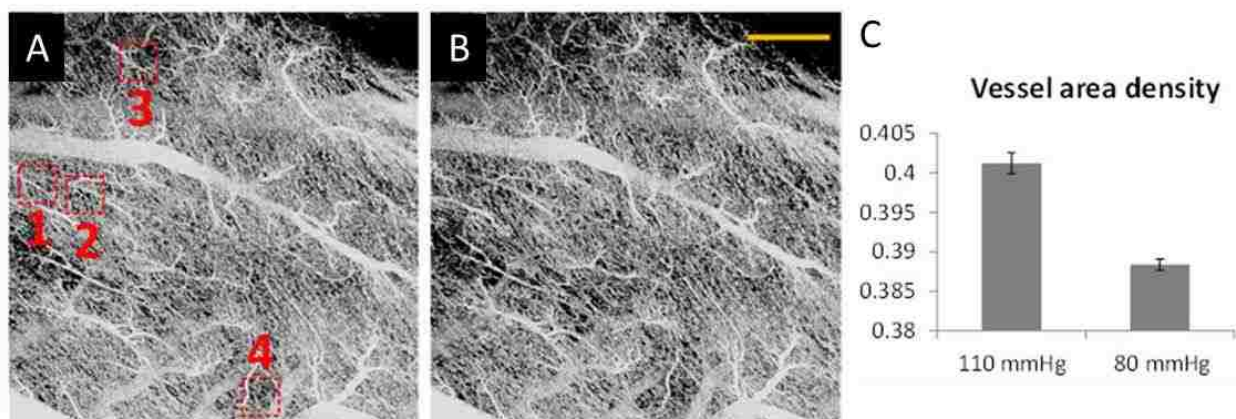
Figure 4.3 – Effect of perfusion pressure on OMAG imaging. Maximum intensity projections of OMAG flow data at (A) 110 mmHg and (B) 80 mmHg. Scale bars: 500 µm. Red outlined regions designate ROIs of interest in Figure 4.4. (C) Quantification of vessel area density presented as a percentage of the imaging field.

the biggest differences observed at the level of the microvasculature. By selecting four regions of interests (ROIs) outlined in red in Figure 4.3A that contain capillary-scale vasculature, we were able to better observe the effects of perfusion pressure. The average vessel area density in these regions was 0.401 ± 0.001 (110 mmHg) and 0.388 ± 0.001 (80 mmHg) (Fig 4.3C) suggesting that increased applied pressure led to better perfusion through a greater density of vessels. Upon closer inspection of enlarged views of the four ROIs, pressure-dependent recruitment of new microvascular branches was observed (Fig 4.4A, yellow arrows), likely due to an increase in flow in vessels that had non-detectable flow at the lower pressure. These data demonstrated that high resolution images of coronary vasculature can be obtained with OMAG imaging on Langendorff perfused hearts.
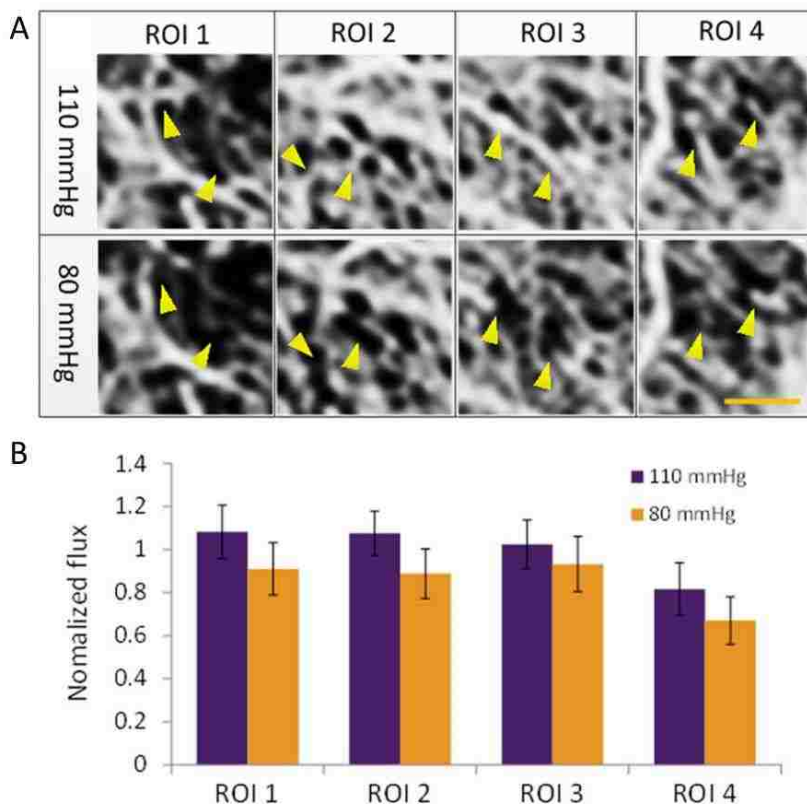
Figure 4.4 – OMAG correlation to flux. (A) Magnified projection images of ROIs from Figure 4.3, panel A. Yellow arrows depict regions where observed flow differed between the two pressures. (B) Quantification of flux at each ROI for both pressures.

4.4.2 *OMAG signal intensity correlates to velocity*

Cross-sectional OMAG signals have been reported to be proportional to flux, or the total number of particles flowing through a cross section per unit time [112,198]. We sought to determine if increased flow rates could be detected in our OMAG data sets. Specifically, a higher perfusion pressure should result in increased flow rates in the vasculature corresponding to increased flux. The pixel intensities for each ROI were summed and normalized to the vessel area. The values were further normalized to average OMAG flux at 110 mmHg pressure. We observed a decrease in flux in all four ROIs at 80 mmHg perfusion pressure compared to flux in the same region at 110 mmHg perfusion pressures (Fig 4.4B). This comparison, however, is only an estimate of flux and these values cannot be converted to units that have more physiological relevance such as velocity and flow rate. Concurrent with the development of Langendorff-based imaging of coronary vasculature, the Wang lab developed a more robust method for acquiring velocimetry data from OCT data sets (OMAG-V). To determine the exact relationship between OMAG signal (mean frequency) and velocity, Dr. Qinqin Zhang performed a series of phantom experiments with controlled flow rates through microfluidic channels of varied diameters. Mean frequency was plotted against the known velocities in the
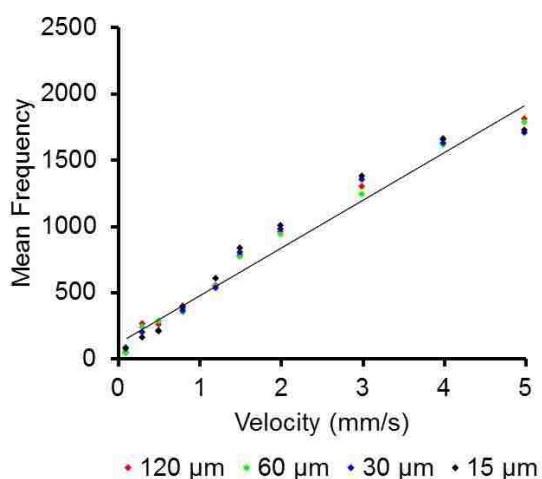
Figure 4.5 – OMAG-V mean frequency correlation to velocity. Data were generated by acquiring velocimetry data for microfluidic channels perfused at a range of velocities. The slope of the linearly correlated data was used to convert mean frequency to velocity for the Langendorff perfused rat hearts.

 channels and determined to have a linear relationship independent of the channel diameter (Fig 4.5). Collectively, these data demonstrate that the combination of high resolution OMAG plus 3D mapping and OMAG velocimetry data could be used to quantitatively assess myocardial perfusion dynamics.

4.4.3 *Patterned vascular graft implantation in rat model of myocardial infarction.*

To test the hypothesis that the presence of a patterned vascular network would promote better spontaneous vascular host integration with increased perfusion dynamics, we implanted collagen gels containing engineered µVs onto the epicardial surfaces of injured rat hearts 4 days post ischemia/reperfusion (I/R) injury. We used a large grid pattern with 125 µm feature height (Fig 4.6Ai) to generate constructs with a large vascular surface area. The engineered µVs were generated with mTm-hESC-ECs seeded in the bulk collagen (where they self-assemble into lumen-containing microvessels) and on the inner surfaces of the patterned network (µV + SA). These were compared to control constructs containing only bulk-phase, self-assembled networks formed from seeding mTm-hESC-ECs in collagen gel (SA) (Fig 4.6Aii-iii). The vascular constructs were cultured for 4 days to allow for tubulogenesis and vascular remodeling and then sutured onto the epicardium of the left ventricle (Fig 4.6Bi). After five days, the rats were euthanized, and their hearts were arrested in diastole and excised followed by perfusion fixation at physiological pressure (~100 mmHg). We chose 5 days post implantation as our experimental timepoint based on previous studies that found substantial vascular infiltration in collagen gels 3 – 4 days post-implantation [87]. The grafts were easily identifiable on the epicardial surface of intact
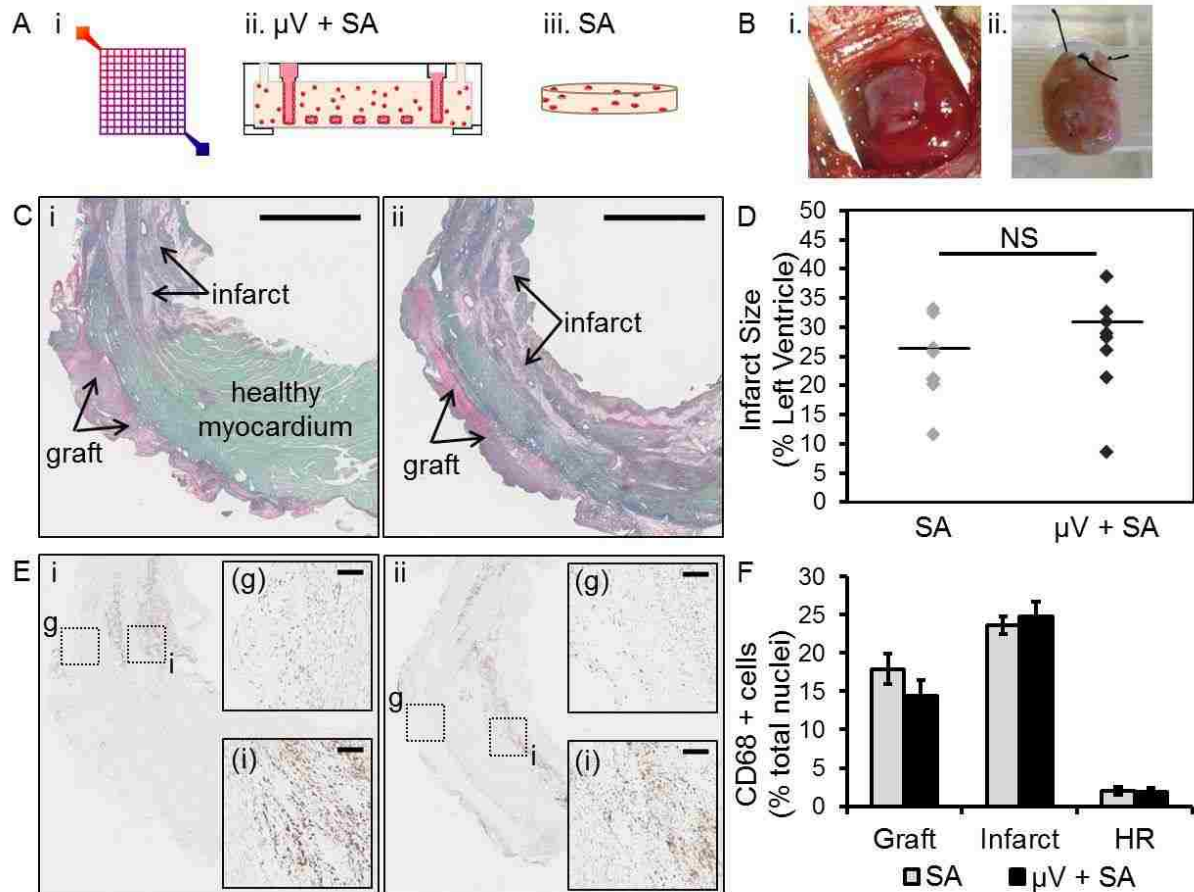
Figure 4.6 – Vascular implantation: I/R injury and inflammation. (A) Schematic of vascular constructs (i) network geometry of patterned constructs. Schematics of (ii) µV+SA and (iii) SA vascular constructs. (B) Pictures of vascular grafts sutured onto epicardial surface of the rat heart (i) at the time of implantation surgery and (ii) after heart excision, cannulation, and perfusion fixation. (C) Picrosirius red/fast green stain to (i) µV+SA grafts and (ii) SA grafts. Collagenous regions, such as the infarct and grafts, stain red/purple and healthy tissue regions stain green (scale bar: 2 mm). (D) Quantification of infarct size as a percentage of left ventricle area. (E) CD68 (brown) immunohistochemistry with hematoxylin (blue) counterstain to detect nuclei in (i) µV+SA grafts and (ii) SA grafts. Insets show zoomed in regions of the grafts (g) and infarcts (i) (scale bar: 100µm). (F) Quantification of CD68 + cells as a percentage of total nuclei in the grafts, infarcts and healthy regions (HR). N = 8, 9 for µV+SA and SA groups, respectively.

hearts as well as in post-processed histological sections (Fig 4.6Bii-C). Importantly, the

extent of I/R injury was comparable between groups, and to previous rat I/R studies in

our lab [58,199], as demonstrated by similar infarct sizes (Fig 4.6D) and similar

inflammatory response evaluated by macrophage (CD68+) infiltration to injured and graft regions (Fig 4.6E-F).

4.4.4 *Optical microangiography (OMAG) for the assessment of graft vascular perfusion.*
To determine the extent of vascular integration between the rat myocardium and the implanted vascular grafts, we used two OMAG imaging protocols, OMAG and OMAG-V (see *methods*), in order to acquire both high resolution images of vascular flow and to quantify velocities within the grafts. In normal healthy regions, OMAG and OMAG-V images revealed dense vasculature with hierarchical branching structure and high flow rates in large arteries compared to smaller vessels (Fig 4.7A). Vascular flow was observed in patterned vascular grafts (µV + SA), and like the healthy regions, flow velocities were higher in larger diameter vessels. In sharp contrast, unpatterned grafts (SA) had few visible perfused vessels (Fig 4.7B-C). In some cases, the vasculature of the underlying host region was detected in graft OMAG images, so to distinguish between these two regions, we generated three-dimensional images of OMAG flow (Fig 4.7Di. and Diii.) overlaid with structural information extracted from the same OMAG data acquisition (Fig 4.7Dii. and Div.). In 3D, the improvement in vascular perfusion of µV + SA compared to SA grafts was apparent (SV11 and SV12). Quantitation of vessel area density (VAD) revealed that the µV + SA grafts had ~6 fold greater perfused vascular density (33.75 ± 5.65 %) compared to the SA grafts (5.32 ± 1.7 %). The vascular area density in healthy regions of both groups was comparable at 63.48 ± 9.16% and 64.54 ± 5.11% for SA and µV+SA grafts, respectively (Fig 4.7E). Velocities were measured in 20 - 40 µm vessels using the linear correlation between velocity and OMAG-V signal
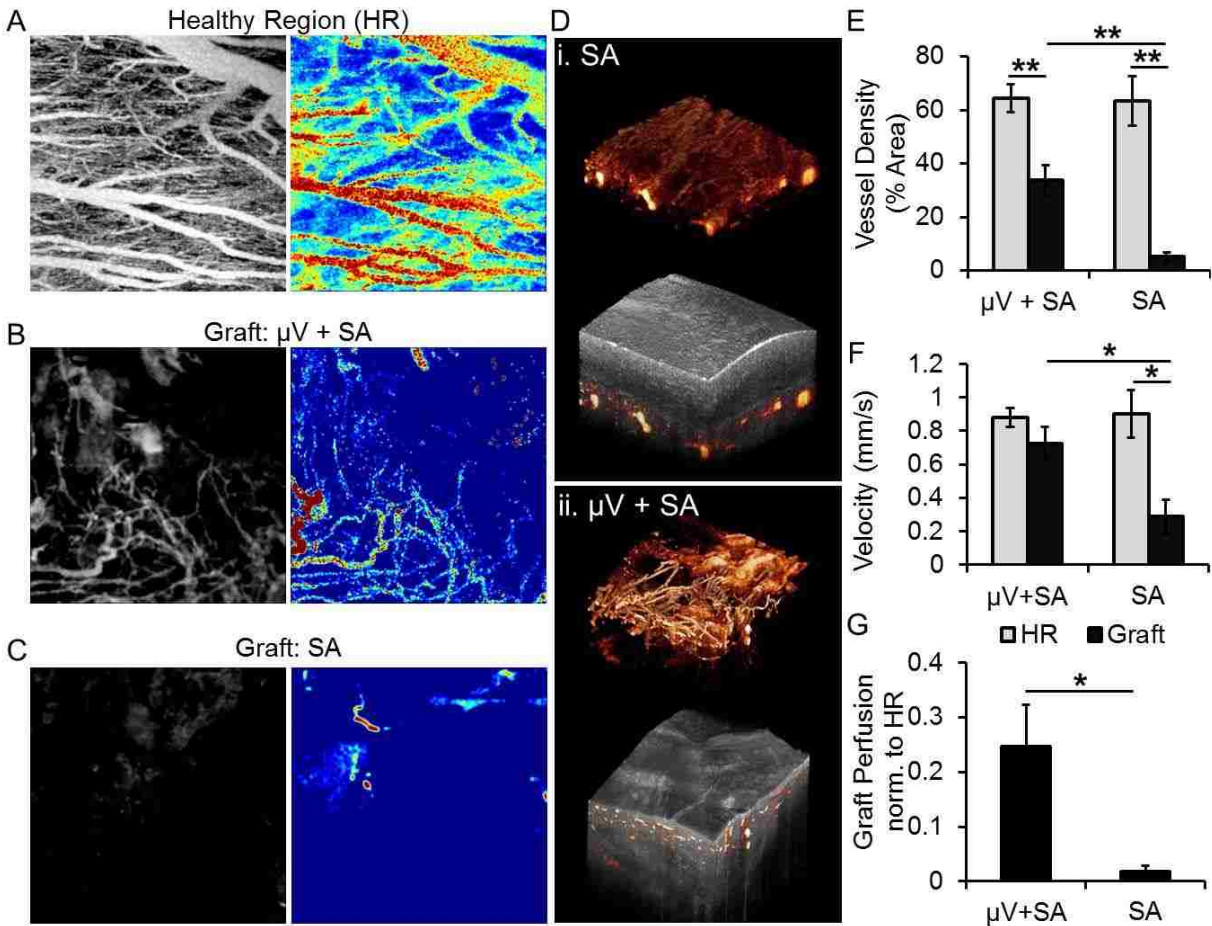
Figure 4.7 – Graft perfusion analysis with OMAG-V 5 days post implantation. (A-C) Doppler-based images of vascular flow in Langendorff perfused hearts: (A) representative healthy region (B) μV+SA graft and (C) SA graft. Left panels in black and white are high resolution, non-quantitative OMAG images of coronary flow. The right panels are OMAG-V images with linear correlation between intensity and velocity. Heat map denotes signal intensity (red – high, dark blue – low). (D) 3D reconstructions of vascular flow in i. SA grafts and ii. μV+SA grafts. OMAG flow data is shown in orange (top panels) and overlaid with gray OMAG structure (bottom panels). (E) Vascular density (percent of imaged region) of perfused vessels in graft and healthy regions (HR) of both groups. Values were calculated from the high resolution OMAG images (N = 8 (μV+SA) and 9 (SA)). (F) Velocimetry measurements of flow in small arterioles (diameter between 20 μm and 40 μm) of graft and healthy regions of μV+SA and SA groups. (G) Volumetric perfusion rate in μV+SA and SA grafts normalized to the perfusion rate in healthy regions. For velocimetry data (panels F-G), N = 6 (μV+SA) and 5 (SA). (statistical significance: * p < 0.05; ** p< 0.01).

intensity. The average velocity was significantly higher in µV + SA grafts (0.72 ± 0.10 mm/s) compared to SA grafts (0.29 ± 0.10 mm/s). The average velocities in similar sized vessels of the rat myocardium were comparable between µV + SA and SA groups at 0.88 ± 0.06 mm/s and 0.90 ± 0.14 mm/s, respectively (Fig 4.7F). The volumetric perfusion rate for the field of view (1.5 mm x 1.5 mm) was calculated for the grafts and healthy regions of µV + SA (Graft: 0.41 ± 0.15 mm^3/s; HR: 1.90 ± 0.28 mm^3/s) and SA (Graft: 0.02 ± 0.01 mm^3/s; HR: 1.96 ± 0.54 mm^3/s) groups. To account for physiological differences on a heart to heart basis as well as to account for the fixed nature of the hearts at the time of perfusion assessment, these values were normalized to that of the healthy regions and found to be significantly higher in µV + SA grafts at 24.73 ± 7.5 % compared to 1.74 ± 1.0 % in SA grafts (Fig 4.7G). Taken together, these findings demonstrate that engineered vascular constructs are able to integrate functionally with host vasculature and specifically that patterned µV improved graft perfusion dynamics.

4.4.5 Patterned engineered human microvessels survive implantation and are perfused. Graft perfusion was confirmed histologically by staining for lectins that were retrograde perfused prior to sectioning and histological processing. Rat hearts were perfused with both fluorescein-conjugated *Griffonia simplicifolia* lectin I (GSL I) isolectin IB4 to label rat endothelium and rhodamine-conjugated *Ulex europaeus* agglutinin I (UEA 1) to label human endothelium. Although these lectins were species specific, the antibodies against them are not. Therefore, to detect perfused lumens originating from both rat and human ECs, sections were stained with antibodies binding to GSL I and UEA 1, and to specifically detect perfused human endothelium, we stained sections with anti-
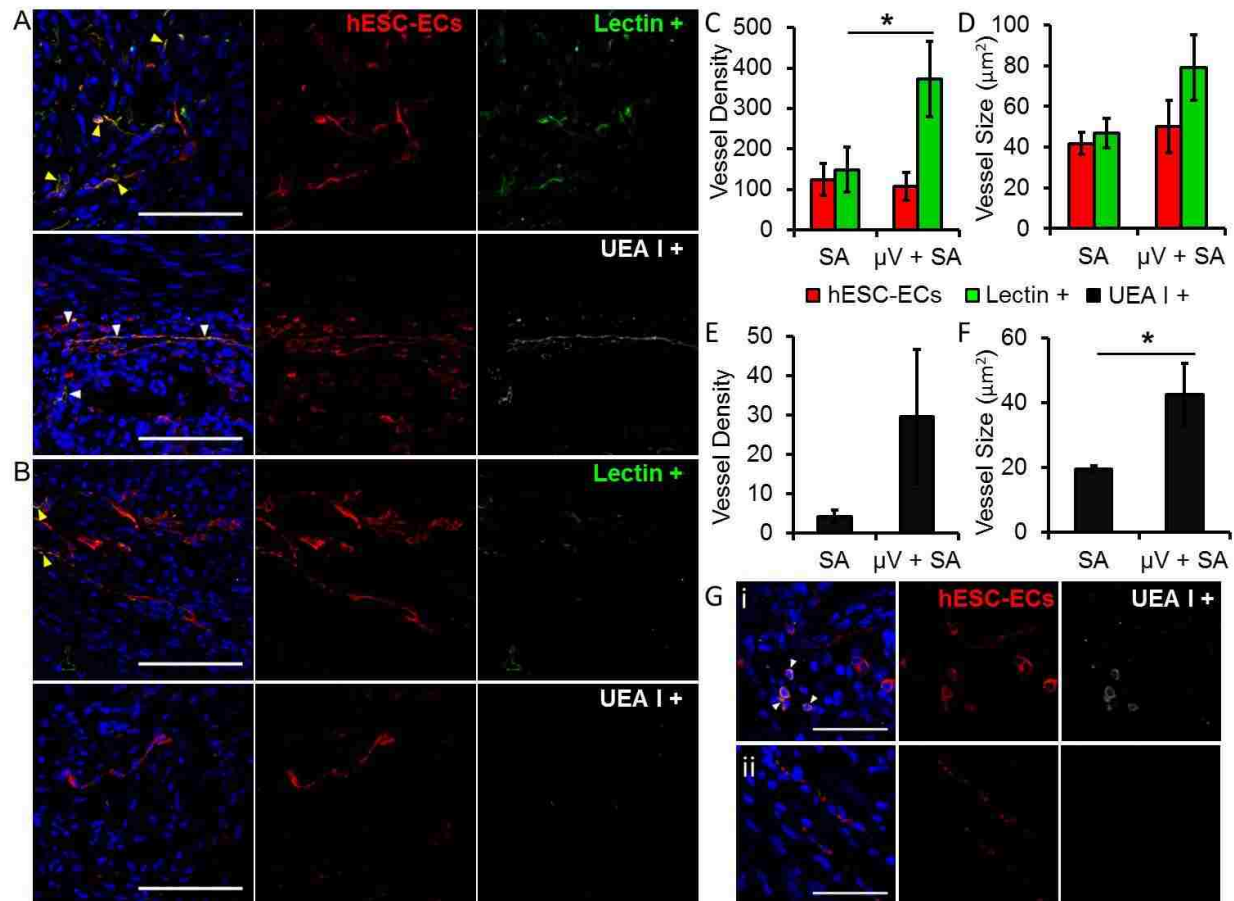
Figure 4.8 – Detection of human ECs and perfused vessels in grafts. (A-B) Immunofluorescent stained paraffin sections of (A) μV+SA grafts and (B) SA grafts. Scale bar: 100 μm. (top panels) hESC-ECs (DsRed +, red) and perfused rat and human endothelium (Lectin +, green). Yellow arrows in merged images denote double positive cells. (bottom panels) hESC-ECs (DsRed +, red) and perfused human endothelium (UEA I +, white). White arrows in merges images denote double positive cells. (C-D) Quantification of (C) vessel density (number of vessels per mm^2), and (D) average vessel size for hESC-EC lumens (DsRed +) and perfused vessels (Lectin +). (E-F) Quantification of (E) vessel density (number of vessels per mm^2), and (D) average vessel size of perfused human lumens (UEA I +). (G) High magnification views of UEA I (white) positive hESC-ECs (DsRed +, red) in (i) μV+SA grafts and (ii) SA grafts. Scale bar: 50 μm. N = 6, 6 for each group. (statistical significance: * $p < 0.05$).

rhodamine antibodies which selectively detected UEA 1 bound human ECs and not

GSL I bound rat endothelium. Human endothelial cells, along with lectin positive (GSL I

+) and rhodamine positive (UEA I +) lumens, were detected in both μV + SA and SA

grafts (Fig 4.8A-B). Quantitation of these results demonstrated that although the density

and size of human vessels in both grafts was the same, a significant increase in

perfused lumen density was observed in µV + SA constructs (Fig 4.8C), along with an

increasing trend in the size of perfused lumens (Fig 4.8D). The density and size of

perfused human lumens were also higher in µV + SA grafts compared to SA grafts,

although only the lumen size was statistically significant (Fig 4.8E-F). Overall, the

density of perfused human vessels (UEA I+) was markedly lower than the total density

of perfused vessels (Lectin +) suggesting that invading rat endothelial cells were a

major contributing factor in the integration of the grafts. High magnification views of
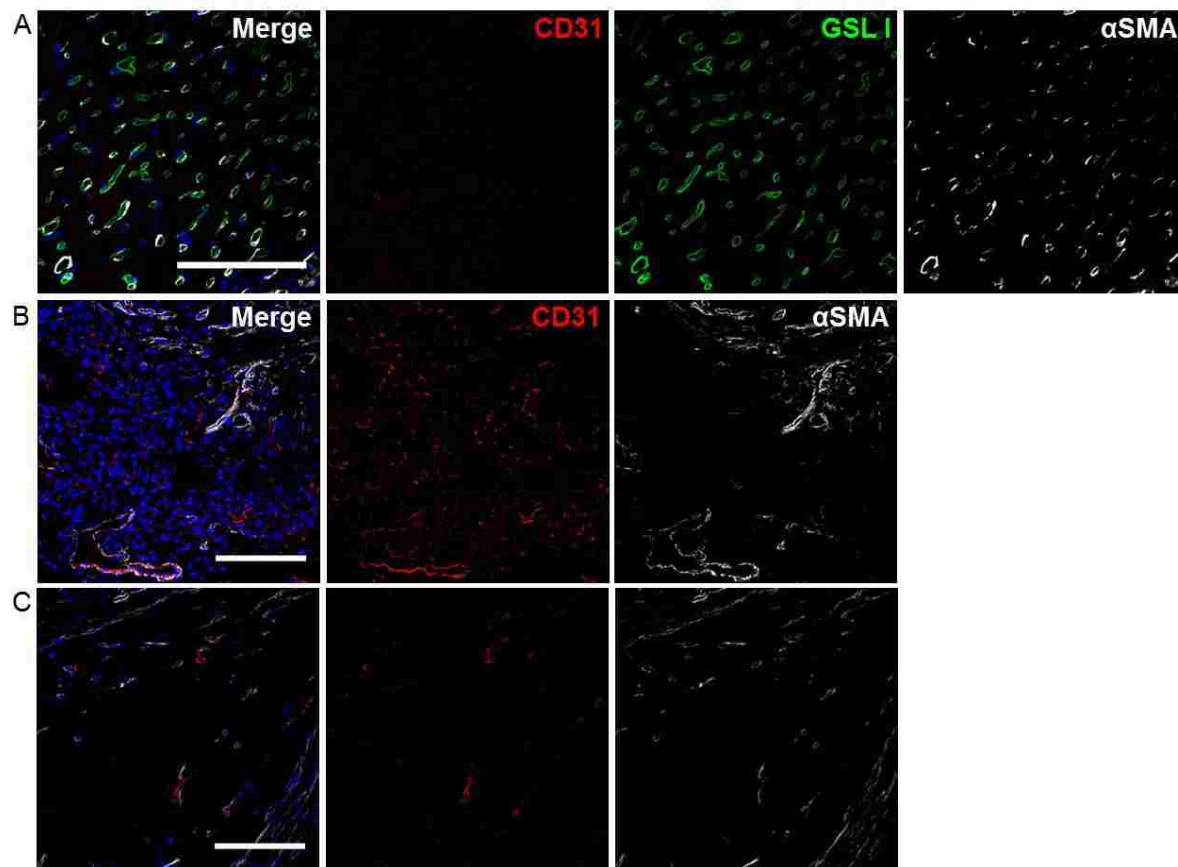
Figure 4.9 – Human CD31 and αSMA histological assessment of grafts. (A) rat myocardium stained for GSL I lectin (green), human CD31 (red), αSMA (white), and nuclei counterstain in blue. (B-C) Immunofluorescent staining for human CD31 (red), αSMA (white), and nuclei counterstain (blue) in (B) µV + SA grafts and (C) SA grafts. Scale bar: 100µm.

perfused human lumens are shown in Figure 4.8G. The presence of human vessels was confirmed with additional staining for human endothelial junction protein, CD31, which stains human ECs and not rat myocardial ECs (Fig 4.9A). Perivascular infiltration of grafts was also investigated to assess if patterned µVs promoted vascular maturation and stabilization and while αSMA coated human vessels were observed in vascular grafts, these events were rare and qualitatively not observed to be different between groups (Fig 4.9B-C). These findings confirm histologically that µV + SA grafts are better perfused than SA grafts and that implanted human endothelial cells contributed to this effect.

4.5 Discussion

Vascular integration is essential for the successful application of engineered tissues, and has presented a major challenge, particularly in the field of cardiac regeneration. While efforts to generate pre-vascularized tissues, such as the one described in chapter 2 of this dissertation, have made considerable progress, the ability to integrate efficiently with the injured myocardium and receive systemic perfusion has not been achieved and/or assessed. In this study, we demonstrated that patterned vascular grafts integrated with host circulation and we used a novel application of OCT-based imaging to assess the dynamics of graft perfusion.

To assess the perfusion dynamics of coronary vasculature, we used optical microangiography (OMAG), which utilizes Doppler principles to distinguish moving from stationary particles to generate images of vascular flow [112]. A common application of OCT-based technologies is to image the flow of red blood cells in live animals which

allows for multiple image acquisitions of the same animal over time. In this way, researchers have assessed vascular flow in response to physiological phenomena such as the effect of inflammation over time [193], recovery after ischemic stroke [200], or to study acute changes in vascular flow due to real time modulation of vascular tone [201]. While this has been done extensively in the brain, mouse ear, skin, etc., motion artifacts from the pumping heart present a major challenge for *in vivo* assessment of coronary flow.

Here, we used retrograde perfusion of formaldehyde-fixed, Langendorff-perfused hearts to generate vascular angiograms. Since these data were collected *ex vivo*, we utilized Intralipid to generate the OCT signal rather than red blood cells. The use of fixed hearts allowed for precise control of the applied perfused pressure to ensure vascular measurements are taken at the same pressure. In the body, most coronary blood flow occurs during diastole: as the heart relaxes, the coronaries dilate and are at their most open state [34]. We therefore arrested the heart in diastole prior to its excision, after inducing maximal vasodilation, fixed the microvasculature in this structural state with formaldehyde. We then performed OMAG graft perfusion studies at 90 mmHg, which is within the diastolic perfusion pressure range for both healthy murine and human hearts [202,203]. Initial studies on healthy hearts were performed with wider perfusion pressure ranges (80 and 110 mmHg) in order to develop the method and determine the effect of pressure on coronary structure and OMAG signal intensity, which correlates to flux. Our findings that higher perfusion pressure caused increased vessel density at the microcirculation level could be attributed to vessel widening or to increased velocities within those regions which were previously not detectable. The increased flux calculated in these regions at the higher perfusion pressure is consistent with this interpretation.

In addition to the high resolution angiograms obtained from OMAG imaging, the ability to co-register structure and flow images from the same field of view allowed for greater synthesis of 3D information than conventional angiographic techniques. Specifically, in our implantation studies, we showed that by overlapping OMAG flow images with their corresponding structural data, we could distinguish host tissue from graft tissue to better determine the perfusion characteristics of the grafts.

At 5 days post implantation, the perfusion velocities in 20 - 30 μm sized vessels within patterned vascular grafts were found to be 1.28 mm/s, which was comparable to the perfusion velocities in the healthy myocardium, as well as comparable to previously measured linear velocities of arterioles which ranged between 1 and 3 mm/s for similar sized venules and arterioles [204–206]. Taken together, these data provide substantial evidence that pre-patterned vascular networks on the small-arteriole scale are able to more efficiently integrate with coronary vasculature and conduct blood flow at physiologically relevant speeds.

The ability to quantify the perfusion dynamics of implanted vascular grafts *ex vivo* could have profound effects in the future development of vascular engineering techniques. Specifically, measurement of flow velocities will provide a much better metric for comparing different strategies. However, one limitation to this approach is the inability to distinguish human vessels from rat vessels during the real-time OMAG data acquisition. In this study, we relied on subsequent histological detection to confirm the role of implanted human cells. Since a majority of the three dimensional and morphological information of the graft vasculature is indistinguishable in histology, we were unable to determine to what extent the cells within the patterned network

contributed to the increased perfusion dynamics. A system which has duel imaging capabilities with both OCT and fluorescent-based imaging could potentially be used to overcome this challenge.

Despite a normal range of velocities displayed in vessels within patterned vascular grafts, structurally, these newly integrated vessels do not yet resemble proper coronary structure. The graft vessels are more sparsely distributed with tortuous and unorganized structures compared to the dense, aligned vasculature displayed by their healthy counterparts. The overall structure of perfused vessels in the grafts did not seem to retain the original geometry of the network pattern. This is likely attributed to several factors. Our histological assessment suggested that although the implanted human endothelial cells did contribute to the newly connected and perfused vessels in the graft, the majority of perfused vessels originated from the host. This suggests that despite pre-patterning efforts, substantial remodeling still occurred as the host vessels infiltrated the graft which is consistent with a previous study that demonstrated dynamic interactions between host and implanted vessels during the process of anastomosis [207]. An interesting follow up experiment could be performed to determine if the increased host infiltration observed in patterned grafts is due mostly to structural cues provided by the patterned channel or from paracrine signals between the pre-perfused vasculature and adjacent host cells. This would help elucidate whether endothelialization is required to promote pattern-facilitated host integration.

Given the extensive remodeling of the grafts, it would be interesting to evaluate whether the precise geometry of the vasculature affects its ability to integrate. In this study, we used a grid-like pattern to fabricate the microvessels in order to maximize the

perfusion area with multiple vascular branches. In future applications, the network structure could be generated with aligned parallel vessels to better mimic coronary structure. Juhas et. al. recently demonstrated that in implanted bioengineered muscle fibers, the ingrown capillaries were randomly oriented at the periphery but within the interior of the construct, they were aligned with the myofibers suggesting that structural cues from the surrounding tissue may help guide the structure of infiltrating vasculature [208]. In the context of the heart, it is possible that the presence of oriented cardiomyocytes along with patterned parallel vasculature could help guide coronary infiltration to better mimic myocardial structure.

Chapter 5.

Summary and Future Directions

The above work addressed several of the key challenges associated with cardiovascular tissue engineering, namely vascularization and host integration. In chapter 2, we used co-culture with stromal cells to facilitate cardiomyocyte culture in dense collagen which allowed for the incorporation of engineered microvessels. In chapter 3, we demonstrated that stem cell derived endothelial cells are functional and are suitable cell source for physiological engineered vasculature. Finally, in chapter 4, we implanted patterned vascular grafts seeded with stem cell derived endothelial cells and demonstrated physiological perfusion dynamics using a novel application of optical coherence tomography.

The research presented in this dissertation sets the stage for two potential immediate future directions that would have vast implications in the field of cardiac regeneration. The most exciting next step in this work would be to combine the knowledge from all three chapters presented here to study the therapeutic effect and functional integration of an all stem cell derived pre-vascularized cardiac construct. The generation of engineered tissues with therapeutically relevant thickness could potentially be used to achieve functional improvement in injured hearts. Our data suggests that the patterned vasculature will be able to integrate with coronary circulation to a greater degree than previously achieved, and potentially sustain graft viability well enough for therapeutic effect. However, one remaining question is whether the vascularized tissue will integrate fast enough to benefit the survival of the graft. This

leads to a second exciting potential follow up study – facilitating direct anastomosis between the engineered constructs and the coronary arteries. For this to be successful, technical challenges associated with establishing surgical connections to coronary arteries while the heart is beating would have to be overcome. One possible approach to start with would be to connect the construct to a vascular supply outside of the heart. Given the tight association with myofibril structure and vascular patterning in the myocardium, however, it is possible that this approach may have functional consequences such as a decreased ability for the construct to electromechanically integrate with host myocardium. Furthermore, additional characterization, such as burst pressure assessment, would have to be done to ensure engineered microvessels could withstand immediate systemic perfusion.

References

1.   Wang, Z. *et al.* Specific metabolic rates of major organs and tissues across adulthood: evaluation by mechanistic model of resting energy expenditure. *Am. J. Clin. Nutr.* **92,** 1369–77 (2010).

2.   Hsieh, P. C. H., Davis, M. E., Lisowski, L. K. & Lee, R. T. Endothelial-cardiomyocyte interactions in cardiac development and repair. *Annu. Rev. Physiol.* **68,** 51–66 (2006).

3.   Lesman, A., Gepstein, L. & Levenberg, S. Vascularization shaping the heart. *Ann. N. Y. Acad. Sci.* **1188,** 46–51 (2010).

4.   Brutsaert, D. L. Cardiac Endothelial-Myocardial Signaling: Its Role in Cardiac Growth, Contractile Performance, and Rhythmicity. *Physiol. Rev.* **83,** 59–115 (2003).

5.   Reese, D. E., Mikawa, T. & Bader, D. M. Development of the coronary vessel system. *Circ. Res.* **91,** 761–768 (2002).

6.   Mikawa, T. & Fischman, D. a. Retroviral analysis of cardiac morphogenesis: discontinuous formation of coronary vessels. *Proc. Natl. Acad. Sci. U. S. A.* **89,** 9504–9508 (1992).

7.   Zhou, B. *et al.* Epicardial progenitors contribute to the cardiomyocyte lineage in the developing heart. *Nature* **454,** 109–113 (2008).

8.   Majesky, M. W. Development of Coronary Vessels. *Curr. Top. Dev. Biol.* **62,** 225–259 (2004).

9.   Katz, T. C. *et al.* Distinct Compartments of the Proepicardial Organ Give Rise to Coronary Vascular Endothelial Cells. *Dev. Cell* **22,** 639–650 (2012).

10. Männer, J., Pérez-Pomares, J. M., Macías, D. & Muñoz-Chápuli, R. The origin, formation and developmental significance of the epicardium: a review. *Cells. Tissues. Organs* **169,** 89–103 (2001).

11. Mikawa, T. & Gourdie, R. G. Pericardial mesoderm generates a population of coronary smooth muscle cells migrating into the heart along with ingrowth of the epicardial organ. *Dev. Biol.* **174,** 221–232 (1996).

12. Matthew Velkey, J. & Bernanke, D. H. Apoptosis during coronary artery orifice development in the chick embryo. *Anat. Rec.* **262,** 310–317 (2001).

13. Red-Horse, K., Ueno, H., Weissman, I. L. & Krasnow, M. a. Coronary arteries form by developmental reprogramming of venous cells. *Nature* **464,** 549–553 (2010).

14. Wu, B. *et al.* Endocardial cells form the coronary arteries by angiogenesis through myocardial-endocardial VEGF signaling. *Cell* **151,** 1083–1096 (2012).

15. Tevosian, S. G. *et al.* FOG-2, a cofactor for GATA transcription factors, is essential for heart morphogenesis and development of coronary vessels from epicardium. *Cell* **101,** 729–739 (2000).

16. Armulik, A. Endothelial/Pericyte Interactions. *Circ. Res.* **97,** 512–523 (2005).

17. Chen, Q. *et al.* Endothelial cells are progenitors of cardiac pericytes and vascular smooth muscle cells. *Nat. Commun.* **7,** 12422 (2016).

18. Gimbrone, M. a., Nagel, T. & Topper, J. N. Biomechanical activation: An emerging paradigm in endothelial adhesion biology. *J. Clin. Invest.* **99,** 1809–1813 (1997).

19. Dejana, E. Endothelial cell-cell junctions: happy together. *Nat. Rev. Mol. Cell Biol.* **5,** 261–270 (2004).

20. Bernardo, A. Effects of inflammatory cytokines on the release and cleavage of the endothelial cell-derived ultralarge von Willebrand factor multimers under flow. *Blood* **104,** 100–106 (2004).

21. Deanfield, J. E., Halcox, J. P. & Rabelink, T. J. Endothelial Function and Dysfunction. *Circulation* **115,** (2007).

22. Weber, C., Fraemohs, L. & Dejana, E. The role of junctional adhesion molecules in vascular inflammation. *Nat. Rev. Immunol.* **7,** 467–477 (2007).

23. Messner, B. & Bernhard, D. Smoking and cardiovascular disease: Mechanisms of endothelial dysfunction and early atherogenesis. *Arterioscler. Thromb. Vasc. Biol.* **34,** 509–515 (2014).

24. Szocs, K. Endothelial Dysfunction and Reactive Oxygen Species Production in Ischemia/Reperfusion and Nitrate Tolerance. *Gen. Physiol. Biophys* **23,** 265–295 (2004).

25. Bevilacqua, M., Stengelin, S., Gimbrone, M. & Seed, B. Endothelial leukocyte adhesion molecule 1: an inducible receptor for neutrophils related to complement regulatory proteins and lectins. *Science (80-.).* **243,** (1989).

26. Cybulsky, M. & Gimbrone, M. Endothelial expression of a mononuclear leukocyte adhesion molecule during atherogenesis. *Science (80-.).* **251,** (1991).

27. Pober, J. S. Endothelial activation: intracellular signaling pathways. *Arthritis Res.* **4,** S109–S116 (2002).

28. Ando, J. & Yamamoto, K. Vascular mechanobiology: endothelial cell responses to fluid shear stress. *Circ. J.* **73,** 1983–92 (2009).

29. Yanagisawa, M. *et al.* A novel potent vasoconstrictor peptide produced by

vascular endothelial cells. *Nature* **332,** 411–415 (1988).

30. Davies, P. F. Flow-mediated endothelial mechanotransduction. *Physiol. Rev.* **75,** (1995).

31. Munson, B., Young, D. & Okiishi, T. *The Fundamentals of Fluid Mechanics. 5th ed.* (John Wiley & Sons, Ltd., 2006).

32. Malek, A. M., Alper, S. L. & Izumo, S. Hemodynamic Shear Stress and Its Role in Atherosclerosis. *J. Am. Med. Assoc.* **282,** 2035–2042 (1999).

33. Lee, J. J., Tyml, K., Menkis, A. H., Novick, R. J. & McKenzie, F. N. Evaluation of Pulsatile and Nonpulsatile Flow in Capillaries of Goat Skeletal Muscle Using Intravital Microscopy. *Microvasc. Res.* **48,** 316–327 (1994).

34. Ramanathan, T. & Skinner, H. Coronary blood flow. *Contin. Educ. Anaesthesia, Crit. Care Pain* **5,** 61–64 (2005).

35. DePaola, N., \mboxGimbrone Jr, M. A., Davies, P. F. & \mboxDewey Jr, C. F. Vascular endothelium responds to fluid shear stress gradients. *Arterioscler. Thromb. Vasc. Biol.* **12,** 1254–1257 (1992).

36. Conway, D. E. *et al.* Fluid shear stress on endothelial cells modulates mechanical tension across VE-cadherin and PECAM-1. *Curr. Biol.* **23,** 1024–30 (2013).

37. Chiu, J.-J. & Chien, S. Effects of Disturbed Flow on Vascular Endothelium: Pathophysiological Basis and Clinical Perspectives. *Physiol. Rev.* **91,** 327–387 (2011).

38. Baeyens, N. & Schwartz, M. A. Biomechanics of vascular mechanosensation and remodeling. *Mol. Biol. Cell* **27,** 7–11 (2016).

39. Baeyens, N. *et al.* Vascular remodeling is governed by a VEGFR3-dependent

fluid shear stress set point. *Elife* **4,** 3982–3992 (2015).

40.   Franco, C. A. *et al.* Non-canonical Wnt signalling modulates the endothelial shear stress flow sensor in vascular remodelling. *Elife* **5,** e07727 (2016).

41.   Mozaffarian, D. *et al.* Executive Summary: Heart Disease and Stroke Statistics—2015 Update. *Circulation* **131,** (2015).

42.   Rasmussen, T. L., Raveendran, G., Zhang, J. & Garry, D. J. Getting to the heart of myocardial stem cells and cell therapy. *Circulation* **123,** 1771–1779 (2011).

43.   Sima, A. V., Stancu, C. S. & Simionescu, M. Vascular endothelium in atherosclerosis. *Cell Tissue Res.* **335,** 191–203 (2009).

44.   Laflamme, M. a & Murry, C. E. Heart regeneration. *Nature* **473,** 326–335 (2011).

45.   Virag, J. I. & Murry, C. E. Myofibroblast and endothelial cell proliferation during murine myocardial infarct repair. *Am. J. Pathol.* **163,** 2433–40 (2003).

46.   van den Borne, S. W. M. *et al.* Myocardial remodeling after infarction: the role of myofibroblasts. *Nat. Rev. Cardiol.* **7,** 30–37 (2010).

47.   Wong, S. & Bernstein, H. Cardiac regeneration using human embryonic stem cells: producing cells for future therapy. *Regen. Med.* **5,** 763–775 (2010).

48.   Katritsis, D. G. *et al.* Transcoronary transplantation of autologous mesenchymal stem cells and endothelial progenitors into infarcted human myocardium. *Catheter. Cardiovasc. Interv.* **65,** 321–329 (2005).

49.   Cho, H.-J. *et al.* Role of host tissues for sustained humoral effects after endothelial progenitor cell transplantation into the ischemic heart. *J. Exp. Med.* **204,** 3257–69 (2007).

50.   Strauer, B. E. *et al.* Repair of infarcted myocardium by autologous intracoronary

mononuclear bone marrow cell transplantation in humans. *Circulation* **106,** 1913–
8 (2002).

51.   Perin, E. C. *et al.* Transendocardial, autologous bone marrow cell transplantation
for severe, chronic ischemic heart failure. *Circulation* **107,** 2294–302 (2003).

52.   Dib, N. *et al.* Safety and feasibility of autologous myoblast transplantation in
patients with ischemic cardiomyopathy: four-year follow-up. *Circulation* **112,**
1748–55 (2005).

53.   Siminiak, T. *et al.* Percutaneous trans-coronary-venous transplantation of
autologous skeletal myoblasts in the treatment of post-infarction myocardial
contractility impairment: the POZNAN trial. *Eur. Heart J.* **26,** 1188–95 (2005).

54.   Boyle, A. J., McNiece, I. K. & Hare, J. M. in *Methods in molecular biology (Clifton,
N.J.)* **660,** 65–84 (2010).

55.   van Laake, L. W. *et al.* Human embryonic stem cell-derived cardiomyocytes
survive and mature in the mouse heart and transiently improve function after
myocardial infarction. *Stem Cell Res.* **1,** 9–24 (2007).

56.   Laflamme, M. A. *et al.* Formation of Human Myocardium in the Rat Heart from
Human Embryonic Stem Cells. *Am. J. Pathol.* **167,** 663–671 (2005).

57.   Kofidis, T. *et al.* Allopurinol/uricase and ibuprofen enhance engraftment of
cardiomyocyte-enriched human embryonic stem cells and improve cardiac
function following myocardial injury. *Eur. J. Cardiothorac. Surg.* **29,** 50–5 (2006).

58.   Gerbin, K. A., Yang, X., Murry, C. E. & Coulombe, K. L. K. Enhanced Electrical
Integration of Engineered Human Myocardium via Intramyocardial versus
Epicardial Delivery in Infarcted Rat Hearts. *PLoS One* **10,** e0131446 (2015).

59. Chong, J. J. H. *et al.* Human embryonic-stem-cell-derived cardiomyocytes regenerate non-human primate hearts. *Nature* **510,** 273–7 (2014).

60. Müller-Ehmsen, J. *et al.* Survival and Development of Neonatal Rat Cardiomyocytes Transplanted into Adult Myocardium. *J. Mol. Cell. Cardiol.* **34,** 107–116 (2002).

61. Zhang, M. *et al.* Cardiomyocyte grafting for cardiac repair: graft cell death and anti-death strategies. *J. Mol. Cell. Cardiol.* **33,** 907–21 (2001).

62. Lieu, D. K. *et al.* Mechanism-based facilitated maturation of human pluripotent stem cell-derived cardiomyocytes. *Circ. Arrhythm. Electrophysiol.* **6,** 191–201 (2013).

63. Robertson, C., Tran, D. D. & George, S. C. Concise review: maturation phases of human pluripotent stem cell-derived cardiomyocytes. *Stem Cells* **31,** 829–37 (2013).

64. Kim, C. *et al.* Non-cardiomyocytes influence the electrophysiological maturation of human embryonic stem cell-derived cardiomyocytes during differentiation. *Stem Cells Dev.* **19,** 783–795 (2010).

65. Lundy, S. D., Zhu, W.-Z., Regnier, M. & Laflamme, M. A. Structural and functional maturation of cardiomyocytes derived from human pluripotent stem cells. *Stem Cells Dev.* **22,** 1991–2002 (2013).

66. Jacot, J. G. *et al.* Cardiac Myocyte Force Dvelpoment during Differentiation and maturation. *Ann. N. Y. Acad. Sci.* **1188,** 121–127 (2010).

67. Kawaguchi, N., Hatta, K. & Nakanishi, T. 3D-culture system for heart regeneration and cardiac medicine. *Biomed Res. Int.* **2013,** 895967 (2013).

68. Akins, R. E. *et al.* Three-dimensional culture alters primary cardiac cell phenotype. *Tissue Eng. Part A* **16,** 629–41 (2010).

69. Zimmermann, W. H. *et al.* Tissue engineering of a differentiated cardiac muscle construct. *Circ. Res.* **90,** 223–230 (2002).

70. Tulloch, N. L. *et al.* Growth of Engineered Human Myocardium With Mechanical Loading and Vascular Coculture. *Circ. Res.* **109,** 47–59 (2011).

71. Caspi, O. *et al.* Transplantation of human embryonic stem cell-derived cardiomyocytes improves myocardial performance in infarcted rat hearts. *J. Am. Coll. Cardiol.* **50,** 1884–93 (2007).

72. Lesman, A. *et al.* Transplantation of a tissue-engineered human vascularized cardiac muscle. *Tissue Eng. Part A* **16,** 115–25 (2010).

73. Mihic, A. *et al.* The effect of cyclic stretch on maturation and 3D tissue formation of human embryonic stem cell-derived cardiomyocytes. *Biomaterials* **35,** 2798–808 (2014).

74. Xiao, Y. *et al.* Microfabricated perfusable cardiac biowire: a platform that mimics native cardiac bundle. *Lab Chip* **14,** 869–82 (2014).

75. Nunes, S. S. *et al.* Biowire: a platform for maturation of human pluripotent stem cell–derived cardiomyocytes. *Nat. Methods* **10,** 781–787 (2013).

76. Iyer, R. K., Chiu, L. L. Y., Reis, L. a. & Radisic, M. Engineered cardiac tissues. *Curr. Opin. Biotechnol.* **22,** 706–714 (2011).

77. Caspi, O. *et al.* Tissue engineering of vascularized cardiac muscle from human embryonic stem cells. *Circ. Res.* **100,** 263–272 (2007).

78. Sekine, H. *et al.* Endothelial cell coculture within tissue-engineered cardiomyocyte

sheets enhances neovascularization and improves cardiac function of ischemic hearts. *Circulation* **118,** (2008).

79. Sasagawa, T. *et al.* Design of prevascularized three-dimensional cell-dense tissues using a cell sheet stacking manipulation technology. *Biomaterials* **31,** 1646–1654 (2010).

80. Kreutziger, K. L. *et al.* Developing vasculature and stroma in engineered human myocardium. *Tissue Eng. Part A* **17,** 1219–1228 (2011).

81. Huang, N. F., Yu, J., Sievers, R., Li, S. & Lee, R. J. Injectable biopolymers enhance angiogenesis after myocardial infarction. *Tissue Eng.* **11,** 1860–1866 (2005).

82. Abdalla, S., Makhoul, G., Duong, M., Chiu, R. C. J. & Cecere, R. Hyaluronic acid-based hydrogel induces neovascularization and improves cardiac function in a rat model of myocardial infarction. *Interact. Cardiovasc. Thorac. Surg.* **17,** 767–772 (2013).

83. Madden, L. R. *et al.* Proangiogenic scaffolds as functional templates for cardiac tissue engineering. *Proc. Natl. Acad. Sci. U. S. A.* **107,** 15211–15216 (2010).

84. Hao, X. *et al.* Angiogenic effects of sequential release of VEGF-A165 and PDGF-BB with alginate hydrogels after myocardial infarction. *Cardiovasc. Res.* **75,** 178–185 (2007).

85. Saif, J. *et al.* Combination of injectable multiple growth factor-releasing scaffolds and cell therapy as an advanced modality to enhance tissue neovascularization. *Arterioscler. Thromb. Vasc. Biol.* **30,** 1897–1904 (2010).

86. Thomson, K. S., Dupras, S. K., Murry, C. E., Scatena, M. & Regnier, M.

Proangiogenic microtemplated fibrin scaffolds containing aprotinin promote improved wound healing responses. *Angiogenesis* **17,** 195–205 (2014).

87.   Baranski, J. D. *et al.* Geometric control of vascular networks to enhance engineered tissue integration and function. *Proc. Natl. Acad. Sci.* **110,** 7586–7591 (2013).

88.   Raghavan, S., Nelson, C. M., Baranski, J. D., Lim, E. & Chen, C. S. Geometrically controlled endothelial tubulogenesis in micropatterned gels. *Tissue Eng. Part A* **16,** 2255–2263 (2010).

89.   Moya, M. L., Hsu, Y.-H., Lee, A. P., Hughes, C. C. W. & George, S. C. In vitro perfused human capillary networks. *Tissue Eng. Part C. Methods* **19,** 730–7 (2013).

90.   Egorova, A. D. *et al.* Tgfβ/Alk5 signaling is required for shear stress induced klf2 expression in embryonic endothelial cells. *Dev. Dyn.* **240,** 1670–1680 (2011).

91.   Egorova, A. D. *et al.* Lack of primary cilia primes shear-induced endothelial-to-mesenchymal transition. *Circ. Res.* **108,** 1093–101 (2011).

92.   Hedhli, N. *et al.* Endothelium-derived neuregulin protects the heart against ischemic injury. *Circulation* **123,** 2254–2262 (2011).

93.   Zhu, W. Z. *et al.* Neuregulin/ErbB signaling regulates cardiac subtype specification in differentiating human embryonic stem cells. *Circ. Res.* **107,** 776–786 (2010).

94.   Lepic, E., Burger, D., Lu, X., Song, W. & Feng, Q. Lack of endothelial nitric oxide synthase decreases cardiomyocyte proliferation and delays cardiac maturation. *Am. J. Physiol. Cell Physiol.* **291,** C1240–C1246 (2006).

95. Krämer, B. K., Smith, T. W. & Kelly, R. A. Endothelin and increased contractility in adult rat ventricular myocytes. Role of intracellular alkalosis induced by activation of the protein kinase C-dependent Na(+)-H+ exchanger. *Circ. Res.* **68,** 269–79 (1991).

96. Ceylan-Isik, A. F. *et al.* Cardiomyocyte-specific deletion of endothelin receptor A rescues aging-associated cardiac hypertrophy and contractile dysfunction: role of autophagy. *Basic Res. Cardiol.* **108,** 335 (2013).

97. Vantler, M. *et al.* PDGF-BB protects cardiomyocytes from apoptosis and improves contractile function of engineered heart tissue. *J. Mol. Cell. Cardiol.* **48,** 1316–23 (2010).

98. Glen, K. *et al.* Modulation of functional responses of endothelial cells linked to angiogenesis and inflammation by shear stress: differential effects of the mechanotransducer CD31. *J. Cell. Physiol.* **227,** 2710–21 (2012).

99. Miller, J. S. *et al.* Rapid casting of patterned vascular networks for perfusable engineered three-dimensional tissues. *Nat. Mater.* **11,** 768–774 (2012).

100. Vollert, I. *et al.* In vitro perfusion of engineered heart tissue through endothelialized channels. *Tissue Eng. Part A* **20,** 854–63 (2014).

101. Montgomery, M., Zhang, B. & Radisic, M. Cardiac Tissue Vascularization: From Angiogenesis to Microfluidic Blood Vessels. *J. Cardiovasc. Pharmacol. Ther.* **19,** 382–393 (2014).

102. Zheng, Y. *et al.* In vitro microvessels for the study of angiogenesis and thrombosis. *Proc. Natl. Acad. Sci. U. S. A.* **109,** 9342–7 (2012).

103. Roberts, M. A., Kotha, S. S., Phong, K. T. & Zheng, Y. Micropatterning and

Assembly of 3D Microvessels. *J. Vis. Exp.* e54457–e54457 (2016). doi:10.3791/54457

104.   Ligresti, G. *et al.* A Novel Three-Dimensional Human Peritubular Microvascular System. *J. Am. Soc. Nephrol.* (2015). doi:10.1681/ASN.2015070747

105.   Roberts, M. A. *et al.* Stromal Cells in Dense Collagen Promote Cardiomyocyte and Microvascular Patterning in Engineered Human Heart Tissue. *Tissue Eng. Part A* **22,** 633–44 (2016).

106.   Sooppan, R. *et al.* In Vivo Anastomosis and Perfusion of a Three-Dimensionally-Printed Construct Containing Microchannel Networks. *Tissue Eng. Part C Methods* **22,** 1–7 (2016).

107.   Coulombe, K. L. K. & Murry, C. E. Vascular Perfusion of Implanted Human Engineered Cardiac Tissue. *IEEE* 1–2 (2014).

108.   Bezerra, H. G., Costa, M. A., Guagliumi, G., Rollins, A. M. & Simon, D. I. Intracoronary Optical Coherence Tomography: A Comprehensive Review. Clinical and Research Applications. *JACC Cardiovasc. Interv.* **2,** 1035–1046 (2009).

109.   Choi, W. J., Zhi, Z. & Want, R. K. In vivo OCT microangiography of rodent iris. *Opt. Lett.* **39,** 2455–2458 (2014).

110.   Hillman, E. M. C. Optical brain imaging in vivo: techniques and applications from animal to man. *J. Biomed. Opt.* **12,** 051402 (2007).

111.   Reif, R. & Wang, R. K. Label-free imaging of blood vessel morphology with capillary resolution using optical microangiography. *Quant. Imaging Med. Surg.* **2,** 207–12 (2012).

112.   Yousefi, S. & Wang, R. K. Simultaneous estimation of bidirectional particle flow

and relative flux using MUSIC-OCT: phantom studies. *Phys. Med. Biol.* **59,** 6693–708 (2014).

113. Wei, K. *et al.* Quantification of myocardial blood flow with ultrasound-induced destruction of microbubbles administered as a constant venous infusion. *Circulation* **97,** 473–483 (1998).

114. Ritman, E. L. Current Status of Developments and Applications of Micro-CT. *Annu. Rev. Biomed. Eng.* **13,** 531–552 (2011).

115. Laflamme, M. a *et al.* Cardiomyocytes derived from human embryonic stem cells in pro-survival factors enhance function of infarcted rat hearts. *Nat. Biotechnol.* **25,** 1015–1024 (2007).

116. Shiba, Y. *et al.* Human ES-cell-derived cardiomyocytes electrically couple and suppress arrhythmias in injured hearts. *Nature* **489,** 322–325 (2012).

117. Zimmermann, W.-H. & Eschenhagen, T. Cardiac tissue engineering for replacement therapy. *Heart Fail. Rev.* **8,** 259–269 (2003).

118. Mol, A. *et al.* Fibrin as a cell carrier in cardiovascular tissue engineering applications. *Biomaterials* **26,** 3113–21 (2005).

119. Thomson, K. S. *et al.* Prevascularized microtemplated fibrin scaffolds for cardiac tissue engineering applications. *Tissue Eng. Part A* **19,** 967–77 (2013).

120. Zimmermann, W.-H. *et al.* Engineered heart tissue grafts improve systolic and diastolic function in infarcted rat hearts. *Nat. Med.* **12,** 452–458 (2006).

121. Paul, J. D. *et al.* SLIT3-ROBO4 activation promotes vascular network formation in human engineered tissue and angiogenesis in vivo. *J. Mol. Cell. Cardiol.* **64,** 124–131 (2013).

122. Duan, Y. *et al.* Hybrid gel composed of native heart matrix and collagen induces cardiac differentiation of human embryonic stem cells without supplemental growth factors. *J. Cardiovasc. Transl. Res.* **4,** 605–15 (2011).

123. Stevens, K. R. *et al.* Physiological function and transplantation of scaffold-free and vascularized human cardiac muscle tissue. *Proc. Natl. Acad. Sci. U. S. A.* **106,** 16568–16573 (2009).

124. Naito, H. *et al.* Optimizing engineered heart tissue for therapeutic applications as surrogate heart muscle. *Circulation* **114,** (2006).

125. Roecklein, B. A. & Torok-Storb, B. Functionally distinct human marrow stromal cell lines immortalized by transduction with the human papilloma virus E6/E7 genes. *Blood* **85,** 997–1005 (1995).

126. Cross, V. L. *et al.* Dense type I collagen matrices that support cellular remodeling and microfabrication for studies of tumor angiogenesis and vasculogenesis in vitro. *Biomaterials* **31,** 8596–8607 (2010).

127. Fan, D., Takawale, A., Lee, J. & Kassiri, Z. Cardiac fibroblasts, fibrosis and extracellular matrix remodeling in heart disease. *Fibrogenesis Tissue Repair* **5,** 15 (2012).

128. Camelliti, P., Borg, T. K. & Kohl, P. Structural and functional characterisation of cardiac fibroblasts. *Cardiovasc. Res.* **65,** 40–51 (2005).

129. Kofidis, T. *et al.* In vitro engineering of heart muscle: artificial myocardial tissue. *J. Thorac. Cardiovasc. Surg.* **124,** 63–9 (2002).

130. He, J.-Q., Ma, Y., Lee, Y., Thomson, J. A. & Kamp, T. J. Human embryonic stem cells develop into multiple types of cardiac myocytes: action potential

characterization. *Circ. Res.* **93,** 32–9 (2003).

131. Dorn, T. *et al.* Direct nkx2-5 transcriptional repression of isl1 controls cardiomyocyte subtype identity. *Stem Cells* **33,** 1113–29 (2015).

132. Kizana, E. *et al.* Fibroblasts modulate cardiomyocyte excitability: implications for cardiac gene therapy. *Gene Ther.* **13,** 1611–1615 (2006).

133. Zalewski, A., Shi, Y. & Johnson, A. G. Diverse origin of intimal cells: Smooth muscle cells, myofibroblasts, fibroblasts, and beyond? *Circ. Res.* **91,** 652–655 (2002).

134. Torok-Storb, B. *et al.* Dissecting the marrow microenvironment. *Ann. N. Y. Acad. Sci.* **872,** 164–170 (1999).

135. Graf, L., Iwata, M. & Torok-Storb, B. Gene expression profiling of the functionally distinct human bone marrow stromal cell lines HS-5 and HS-27a. *Blood* **100,** 1509 (2002).

136. Carlson, M. a & Longaker, M. T. The fibroblast-populated collagen matrix as a model of wound healing: a review of the evidence. *Wound Repair Regen.* **12,** 134–147 (2004).

137. von Tell, D., Armulik, A. & Betsholtz, C. Pericytes and vascular stability. *Exp. Cell Res.* **312,** 623–9 (2006).

138. Armulik, A., Genové, G. & Betsholtz, C. Pericytes: Developmental, Physiological, and Pathological Perspectives, Problems, and Promises. *Dev. Cell* **21,** 193–215 (2011).

139. Larsen, M., Artym, V. V., Green, J. A. & Yamada, K. M. The matrix reorganized: extracellular matrix remodeling and integrin signaling. *Curr. Opin. Cell Biol.* **18,**

463–471 (2006).

140. De Jonge, N., Kanters, F. M. W., Baaijens, F. P. T. & Bouten, C. V. C. Strain-
induced collagen organization at the micro-level in fibrin-based engineered tissue
constructs. *Ann. Biomed. Eng.* **41,** 763–774 (2013).

141. Nichol, J. W., Engelmayr, G. C., Cheng, M. & Freed, L. E. Co-culture induces
alignment in engineered cardiac constructs via MMP-2 expression. *Biochem.
Biophys. Res. Commun.* **373,** 360–365 (2008).

142. Thomopoulos, S., Fomovsky, G. M. & Holmes, J. W. The development of
structural and mechanical anisotropy in fibroblast populated collagen gels. *J.
Biomech. Eng.* **127,** 742–50 (2005).

143. Wang, P. Y., Yu, J., Lin, J. H. & Tsai, W. B. Modulation of alignment, elongation
and contraction of cardiomyocytes through a combination of nanotopography and
rigidity of substrates. *Acta Biomater.* **7,** 3285–3293 (2011).

144. Grinnell, F. Fibroblast biology in three-dimensional collagen matrices. *Trends Cell
Biol.* **13,** 264–269 (2003).

145. Sassoli, C. *et al.* Mesenchymal stromal cells affect cardiomyocyte growth through
juxtacrine Notch-1/Jagged-1 signaling and paracrine mechanisms: Clues for
cardiac regeneration. *J. Mol. Cell. Cardiol.* **51,** 399–408 (2011).

146. Li, Y., Hiroi, Y. & Liao, J. K. Notch signaling as an important mediator of cardiac
repair and regeneration after myocardial infarction. *Trends Cardiovasc. Med.* **20,**
228–31 (2010).

147. Aoyagi, T. & Matsui, T. The Cardiomyocyte as a Source of Cytokines in Cardiac
Injury. *J. Cell Sci. Ther.* **01,** (2012).

148. Sano, M. *et al.* Interleukin-6 family of cytokines mediate angiotensin II-induced cardiac hypertrophy in rodent cardiomyocytes. *J. Biol. Chem.* **275,** 29717–23 (2000).

149. Hirota, H., Yoshida, K., Kishimoto, T. & Taga, T. Continuous activation of gp130, a signal-transducing receptor component for interleukin 6-related cytokines, causes myocardial hypertrophy in mice. *Proc. Natl. Acad. Sci.* **92,** 4862–4866 (1995).

150. Silver, F. H., Siperko, L. M. & Seehra, G. P. Mechanobiology of force transduction in dermal tissue. *Ski. Res. Technol.* **9,** 3–23 (2003).

151. Masuda, S. *et al.* Formation of vascular network structures within cardiac cell sheets from mouse embryonic stem cells. *Regen. Ther.* **2,** 6–16 (2015).

152. Wong, T., McGrath, J. A. & Navsaria, H. The role of fibroblasts in tissue engineering and regeneration. *Br. J. Dermatol.* **156,** 1149–55 (2007).

153. Korte, F. S. *et al.* Upregulation of cardiomyocyte ribonucleotide reductase increases intracellular 2 deoxy-ATP, contractility, and relaxation. *J. Mol. Cell. Cardiol.* **51,** 894–901 (2011).

154. Kreutziger, K. L. *et al.* Calcium binding kinetics of troponin C strongly modulate cooperative activation and tension kinetics in cardiac muscle. *J. Mol. Cell. Cardiol.* **50,** 165–174 (2011).

155. Palpant, N. J. *et al.* Inhibition of -catenin signaling respecifies anterior-like endothelium into beating human cardiomyocytes. *Development* **142,** 3198–3209 (2015).

156. Palpant, N. J. *et al.* Generating high-purity cardiac and endothelial derivatives

from patterned mesoderm using human pluripotent stem cells. *Nat. Protoc.* **12,** 15–31 (2016).

157. Baiguera, S. & Ribatti, D. Endothelialization approaches for viable engineered tissues. *Angiogenesis* **16,** 1–14 (2013).

158. Misfeldt, A. M. *et al.* Endocardial cells are a distinct endothelial lineage derived from Flk1+ multipotent cardiovascular progenitors. *Dev. Biol.* **333,** 78–89 (2009).

159. Gantz, J. a. *et al.* Targeted Genomic Integration of a Selectable Floxed Dual Fluorescence Reporter in Human Embryonic Stem Cells. *PLoS One* **7,** 1–9 (2012).

160. Davis, G. E., Stratman, A. N., Sacharidou, A. & Koh, W. Molecular Basis for Endothelial Lumen Formation and Tubulogenesis During Vasculogenesis and Angiogenic Sprouting. *Int. Rev. Cell Mol. Biol.* **288,** 101–165 (2011).

161. Alexander, J. S. & Elrod, J. W. Extracellular matrix, junctional integrity and matrix metalloproteinase interactions in endothelial permeability regulation*. *J. Anat.* **200,** 561–574 (2002).

162. Tzima, E. *et al.* A mechanosensory complex that mediates the endothelial cell response to fluid shear stress. *Nature* **437,** 426–431 (2005).

163. Andrikopoulos, P. *et al.* Angiogenic Functions of Voltage-gated Na + Channels in Human Endothelial Cells. *J. Biol. Chem.* **286,** 16846–16860 (2011).

164. Mackie, A. R. & Losordo, D. W. CD34-positive stem cells: in the treatment of heart and vascular disease in human beings. *Tex. Heart Inst. J.* **38,** 474–85 (2011).

165. Krenning, G., Barauna, V. G., Krieger, J. E., Harmsen, M. C. & Moonen, J. R. A. J. Endothelial Plasticity: Shifting Phenotypes through Force Feedback. *Stem Cells*

Int. **2016,** (2016).

166. Lacorre, D. A. *et al.* Plasticity of endothelial cells: Rapid dedifferentiation of freshly isolated high endothelial venule endothelial cells outside the lymphoid tissue microenvironment. *Blood* **103,** 4164–4172 (2004).

167. Kisucka, J. *et al.* Platelets and platelet adhesion support angiogenesis while preventing excessive hemorrhage. *Proc. Natl. Acad. Sci. U. S. A.* **103,** 855–60 (2006).

168. Lian, X. *et al.* Directed cardiomyocyte differentiation from human pluripotent stem cells by modulating Wnt/β-catenin signaling under fully defined conditions. *Nat. Protoc.* **8,** 162–75 (2013).

169. Yang, X., Pabon, L. & Murry, C. E. Engineering adolescence: maturation of human pluripotent stem cell-derived cardiomyocytes. *Circ. Res.* **114,** 511–23 (2014).

170. Peinkofer, G. *et al.* From Early Embryonic to Adult Stage: Comparative Study of Action Potentials of Native and Pluripotent Stem Cell-Derived Cardiomyocytes. *Stem Cells Dev.* **25,** 1397–1406 (2016).

171. Moreau, A. *et al.* Biophysical, Molecular, and Pharmacological Characterization of Voltage-Dependent Sodium Channels From Induced Pluripotent Stem Cell-Derived Cardiomyocytes. *Can. J. Cardiol.* **33,** 269–278 (2017).

172. Choi, K. K. *et al.* Hematopoietic and endothelial differentiation of human induced pluripotent stem cells. *Stem Cells* **27,** 559–567 (2009).

173. Levenberg, S., Golub, J. S., Amit, M., Itskovitz-Eldor, J. & Langer, R. Endothelial cells derived from human embryonic stem cells. *Proc. Natl. Acad. Sci. U. S. A.* **99,**

4391–6 (2002).

174. Ribatti, D., Nico, B., Vacca, A., Roncali, L. & Dammacco, F. Endothelial cell heterogeneity and organ specificity. *J. Hematother. Stem Cell Res.* **11,** 81–90 (2002).

175. Aird, W. C. *et al.* Vascular bed-specific expression of an endothelial cell gene is programmed by the tissue microenvironment. *J. Cell Biol.* **138,** 1117–1124 (1997).

176. Kuzu, I. *et al.* Heterogeneity of vascular endothelial cells with relevance to diagnosis of vascular tumours. *J. Clin. Pathol.* **45,** 143–148 (1992).

177. Galie, P. A. *et al.* Fluid shear stress threshold regulates angiogenic sprouting. *Proc. Natl. Acad. Sci. U. S. A.* **111,** 7968–73 (2014).

178. Abraham, S. *et al.* VE-Cadherin-Mediated Cell-Cell Interaction Suppresses Sprouting via Signaling to MLC2 Phosphorylation. *Curr. Biol.* **19,** 668–674 (2009).

179. Asahara, T. Isolation of Putative Progenitor Endothelial Cells for Angiogenesis. *Science (80-.).* **275,** 964–966 (1997).

180. Yau, J. W., Teoh, H. & Verma, S. Endothelial cell control of thrombosis. *BMC Cardiovasc. Disord.* **15,** 130 (2015).

181. Thomas, L. V., Lekshmi, V. & Nair, P. D. Tissue engineered vascular grafts - Preclinical aspects. *Int. J. Cardiol.* **167,** 1091–1100 (2013).

182. Tatterton, M., Wilshaw, S.-P., Ingham, E. & Homer-Vanniasinkam, S. The Use of Antithrombotic Therapies in Reducing Synthetic Small-Diameter Vascular Graft Thrombosis. *Vasc. Endovascular Surg.* **46,** 212–222 (2012).

183. Meinhart, J. G. *et al.* Enhanced Endothelial Cell Retention on Shear-Stressed Synthetic Vascular Grafts Precoated with RGD-Cross-Linked Fibrin. *Tissue Eng.*

11, 887–895 (2005).

184. Bastijanic, J. M. *et al.* In vivo evaluation of biomimetic fluorosurfactant polymer-coated expanded polytetrafluoroethylene vascular grafts in a porcine carotid artery bypass model. *J. Vasc. Surg.* **63,** 1620–1630.e4 (2016).

185. Hashi, C. K. *et al.* Antithrombogenic Modification of Small-Diameter Microfibrous Vascular Grafts. *Arterioscler. Thromb. Vasc. Biol.* **30,** (2010).

186. Zhu, A. P., Ming, Z. & Jian, S. Blood compatibility of chitosan/heparin complex surface modified ePTFE vascular graft. *Appl. Surf. Sci.* **241,** 485–492 (2005).

187. Qin, W. *et al.* Depth-resolved 3D visualization of coronary microvasculature with optical microangiography. *Phys. Med. Biol.* **61,** 7536–7550 (2016).

188. Weyers, J. J. *et al.* Effects of cell grafting on coronary remodeling after myocardial infarction. *J. Am. Heart Assoc.* **2,** (2013).

189. Sekine, H. *et al.* In vitro fabrication of functional three-dimensional tissues with perfusable blood vessels. *Nat. Commun.* **4,** 1399 (2013).

190. Zhang, B. *et al.* Biodegradable scaffold with built-in vasculature for organ-on-a-chip engineering and direct surgical anastomosis. *Nat. Mater.* **15,** 669–678 (2016).

191. Koffler, J. *et al.* Improved vascular organization enhances functional integration of engineered skeletal muscle grafts. *Proc. Natl. Acad. Sci. U. S. A.* **108,** 14789–94 (2011).

192. Chiu, L. L. Y., Montgomery, M., Liang, Y., Liu, H. & Radisic, M. Perfusable branching microvessel bed for vascularization of engineered tissues. *Proc. Natl. Acad. Sci. U. S. A.* **109,** E3414–23 (2012).

193. Qin, W., Baran, U. & Wang, R. Lymphatic response to depilation-induced inflammation in mouse ear assessed with label-free optical lymphangiography. *Lasers Surg. Med.* **47,** 669–676 (2015).

194. Zhi, Z., Qin, J., An, L. & Wang, R. K. Supercontinuum light source enables in vivo optical microangiography of capillary vessels within tissue beds. *Opt. Lett.* **36,** 3169–71 (2011).

195. An, L., Qin, J. & Wang, R. K. Ultrahigh sensitive optical microangiography for in vivo imaging of microcirculations within human skin tissue beds. *Opt Express* **18,** 8220–8228 (2010).

196. Yousefi, S., Zhi, Z. & Wang, R. K. Eigendecomposition-based clutter filtering technique for optical microangiography. *IEEE Trans. Biomed. Eng.* **58,** 2316–2323 (2011).

197. Kasai, C., Namekawa, K., Koyano, A. & Omoto, R. Real-time two-dimensional blood flow imaging using an autocorrelation technique. *IEEE Trans. Sonics Ultrason.* **SU-35,** 458–464 (1985).

198. Yousefi, S., Qin, J. & Wang, R. K. Super-resolution spectral estimation of optical micro-angiography for quantifying blood flow within microcirculatory tissue beds in vivo. *Biomed. Opt. Express* **4,** 1214–28 (2013).

199. Virag, J. I. & Murry, C. E. Myofibroblast and endothelial cell proliferation during murine myocardial infarct repair. *Am. J. Pathol.* **163,** 2433–2440 (2003).

200. Srinivasan, V. J. *et al.* Multiparametric, Longitudinal Optical Coherence Tomography Imaging Reveals Acute Injury and Chronic Recovery in Experimental Ischemic Stroke. *PLoS One* **8,** (2013).

201. Drouin, A. *et al.* Catechin treatment improves cerebrovascular flow-mediated dilation and learning abilities in atherosclerotic mice. *Am J Physiol Hear. Circ Physiol* **300,** H1032–43 (2011).

202. Wildemann, T. M., Mirhosseini, N., Siciliano, S. D. & Weber, L. P. Cardiovascular responses to lead are biphasic, while methylmercury, but not inorganic mercury, monotonically increases blood pressure in rats. *Toxicology* **328,** 1–11 (2015).

203. Lloyd-Jones, D. M. *et al.* Differential control of systolic and diastolic blood pressure : factors associated with lack of blood pressure control in the community. *Hypertens. (Dallas, Tex. 1979)* **36,** 594–9 (2000).

204. Ivanov, K. P., Kalinina, M. K. & Levkovich, Y. I. Blood flow velocity in capillaries of brain and muscles and its physiological significance. *Microvasc. Res.* **22,** 143–155 (1981).

205. Mayrovitz, H. N., Larnard, D. & Duda, G. Blood velocity measurement in human conjunctival vessels. *Cardiovasc. Dis.* **8,** 509–526 (1981).

206. Arfors, K. E., Bergqvist, D., Intaglietta, M. & Westergren, B. Measurements of blood flow velocity in the microcirculation. *Ups. J. Med. Sci.* **80,** 27–33 (1975).

207. Cheng, G. *et al.* Engineered blood vessel networks connect to host vasculature via wrapping-and-tapping anastomosis. *Blood* **118,** 4740–4749 (2011).

208. Juhas, M., Engelmayr, G. C. J., Fontanella, A. N., Palmer, G. M. & Bursac, N. Biomimetic engineered muscle with capacity for vascular integration and functional maturation in vivo. *Proc Natl Acad Sci U S A* **111,** 5508–13 (2014).

209. Yang, X. *et al.* Tri-iodo-l-thyronine promotes the maturation of human cardiomyocytes-derived from induced pluripotent stem cells. *J. Mol. Cell. Cardiol.*

72, 296–304 (2014).

Appendix A.

Additional Methods

Cell Culture

RUES2 hESCs (Rockefeller University, NIH 0013) were maintained in undifferentiated colonies with mouse embryonic fibroblast conditioned media (MEF-CM) supplemented with 5ng/mL human basic fibroblast growth factor (hbFGF) (Peprotech) on Matrigel (BD Biosciences) coated plates. Colony maintenance and cardiomyocyte differentiation were performed as previously described with modifications to the differentiation protocol to include biphasic activation and inhibition of wnt signaling, respectively [115,209]. Briefly, single cell hESC suspensions were re-plated on Matrigel coated plates for monolayer formation. One day prior to confluency of monolayer, the cells were treated with 1uM Chiron 99021 (Cayman) in MEF-CM. Once monolayers reached confluency, the cultures were induced with 100 ng/mL rh-Activin A (R&D) and 1X Matrigel. The time of Activin induction was designated as differentiation day 0. Cultures remained in Activin-A for 18 hours followed by treatment with 5 ng/mL rh-BMP4 (R&D) and 1uM Chiron. On day 3, monolayer were fed with RPMI-B27 (minus insulin) supplemented with 1uM XAV-939 (Tocris, 3748). Differentiation cultures were maintained in RPMI media (Invitrogen) supplemented with B27 without insulin (Life Technologies) and Pen/Strep (Invitrogen) from day 0 to day 5. On day 7, cultures were switched to RPMI with B27 containing insulin (Life Technologies). Spontaneous beating was observed starting day 9 or 10 (supplemental video 1). After 20-30 days of differentiation, cardiomyocyte cultures were enzymatically dispersed and used for construct fabrication. A small aliquot of the cells

(~500K) was used for FACs analysis to determine cardiomyocyte yield and purity. Human bone marrow derived stromal cells HS27a and HS5 (courtesy of Beverly Torok-Storb laboratory at Fred Hutchinson Cancer Research Center) [125], and human dermal fibroblasts (hDF) (Lonza) were maintained in 0.2% gelatin coated flasks with RPMI media (Invitrogen) containing 20% FBS (Invitrogen), 2mM L-glutamine (Invitrogen), 1mM sodium pyruvate (Invitrogen), and 1X pen-strep (Invitrogen). Fetal human heart pericytes were isolated from human fetal heart tissue as the cell population double positive for NG2 and PDGFRβ [104]. Briefly, the heart tissue was processed mechanically followed by enzymatic dissociation to obtain a single cell suspension. This cell suspension was then expanded by culturing them on gelatin coated plates for three to four days in endothelial cell proliferation media, and sorted for NG2+PDGFRβ+CD45- subpopulation in flow cytometry. Human umbilical vein endothelial cells (HUVECS, Lonza) were grown and maintained with EGM (Lonza) supplemented with pen-strep and used prior to passage 6. Enzymatic cleavage was used for harvest of all cell types.

Flow cytometry (FACs)

Aliquots of cardiomyocyte populations were fixed in 3.7% formaldehyde and washed in 5%FBS in PBS prior to staining. The fixed cells were then stained for cardiac troponin T (cTnT) to assess the cardiomyocyte percentage in each cell preparation. Cells were incubated with primary antibody (1:100) (mouse anti human cTnT (Fisher) or mouse IgG1 isotype control (eBiosciences) in 0.75% saponin for 30 minutes. These cells were then washed in 0.75% saponin and incubated with PE conjugated goat anti-mouse (1:200, Jackson) for 30 minutes followed by several washes in 5% FBS in PBS. Stained

cells were then sorted on a FACS Canto II cell analysis instrument and the percent cTnT positive population was determined using FlowJo Software.

Collagen gel preparation

Type I collagen extracted from rat tails as previously described [102] was dissolved in 0.1% acetic acid to a stock concentration of 15mg/mL and stored at 4°C. On the day of experiment, collagen stock was neutralized and diluted on ice to working concentrations of 2.5 or 10mg/mL with 1M NaOH (20mM final), RPMI, 10X RPMI (1X final), 30X Matrigel (1X final), and 100mM HEPES (10mM final) (Invitrogen)

Rheology

Collagen gel was prepared immediately prior to rheology measurements. Deformation measurements of acellular gel (1.25 and 6 mg/mL) were taken using an Anton Paar Physica MCR301 stress-controlled rheometer. A concentric cylinder geometry was used with cup and shaft preheated to 37°C. The hydrogel was neutralized, mixed well, and immediately loaded into the cup after which the shaft was lowered followed by a 20 minute gelation. Mechanical properties of the gel (complex modulus: G*) were determined by measuring deformation in response to shear. We used a frequency sweep oscillation method from 0.01Hz - 100Hz maintained at constant shear of 0.05 Pa.

Fluo4 and GCaMP3 calcium imaging

Fluorescent calcium transients were visualized during two weeks of culture of 3D constructs either from GCaMP3 signal or after incorporation of a calcium indicator dye

(Fluo4, Invitrogen). Constructs made with unmodified RUES2 derived CM were incubated with 1ug/mL Fluo4 diluted in modified HEPES-buffered Tyrodes (HT) solution (1.8mM $CaCl_2 \cdot 2H_2O$; 1mM $MgCl_2 \cdot 2H_2O$; 5.4mM KCl; 140mM NaCl; 0.33mM NaH_2PO_4; 10mM HEPES; 5mM D-glucose, pH 7.4) for 30 minutes at room temperature followed by 2 washes in HT solution. Samples were wrapped in foil during incubation to minimize photobleaching. Constructs were allowed to recover at 37°C for 30 minutes prior to imaging with Canon HD video camera (HF S20).

Contractile force analysis

Force measurements were carried out on constructs after two weeks of culture. Sections of length 1-2 mm were dissected from constructs and each end attached to a stainless steel hook suspending the piece between a length controller (Aurora Scientific) and a force transducer (Aurora Scientific) (Fig. 3A). Each sample was stretched in length with 5% increments and up to 20-25% of the total length. The resulting passive tension and spontaneous active force traces were recorded and analyzed using customized LabView software. The increase in passive tension at each length step over the baseline value at zero stretch was normalized to its unstrained cross sectional area to obtain specific force. The linear slope of normalized passive stress vs. strain was used to determine the Young's modulus. The amplitude of active force for each preparation was measured at each length step and then normalized to unstrained cross sectional area. The reported values for peak active force were taken at maximal stretch (25%). Linear plots of active force vs. strain were shifted by the active force at zero stretch to display the change in active force from zero to max strain. Throughout

measurement acquisition, constructs were submerged in HT solution and maintained at constant physiological temperature of 37°C using a perfusion automatic temperature controller (Warner TC-324).

Immunohistochemistry and quantitative analysis for rectangular constructs

Day 14 constructs were fixed in 3.7% formaldehyde (Sigma) for 20 minutes and washed in PBS followed by an overnight incubation in OCT (Tissue Tek). The samples were then cryoembedded in OCT and stored at -80°C. Cryosections were collected at -20°C with thickness of 7 μm. Standard Hematoxylin and Eosin, and Picro-Sirius red staining protocols were performed. For immunofluorescence staining, fixed slides underwent enzymatic antigen retrieval with Proteinase K followed by one hour block in 1.5% normal goat serum. Slides were incubated in primary antibodies overnight at 4°C followed by 1 hour incubation with secondary antibodies and Hoechst 33342 (Sigma) with standard PBS washes in between. The following primary antibodies were used: mouse anti human sarcomeric α actinin (1:300, Sigma), Rabbit anti human Collagen IV (1:100, abcam), rabbit anti human Fibronectin (1:200, Sigma), rabbit anti human Versican (1:100, abcam), mouse anti Heparan Sulfate (1:100, abcam), and rabbit anti human Laminin (1:100, abcam). Alexa Fluor goat anti mouse 488 (Invitrogen) and Alexa Fluor goat anti rabbit 647 (Invitrogen) were used as secondary antibodies. Images were acquired with Nikon A1R confocal microscope. Image post processing and quantification was done with ImageJ software. Cardiomyocyte alignment was quantified by applying the threshold and directionality macros to the immunofluorescent images of alpha actinin stained cryosections in ImageJ, and is reported as the inverse of the

dispersion angle (¬∞). In the same set of images, sarcomere length was measured on high magnification images (at least 40X objective and X3 optical zoom). Cell density and cross sectional area were quantified on H&E stained cryosections using ImageJ software (analyze particle plugin and measure tool, respectively). Cell density was determined by taking the number of nuclei in the field of view and dividing by the volume of the field of view (section area x 7μm section height). The cross sectional area was determined by measuring the width of constructs and calculating area by assuming a circular cross sectional shape. In the cardiomyocytes only constructs in 6 mg/mL, the rectangular cross-section was assumed since there was no apparent tissue compaction.

Quantitative real-time PCR

Total RNA was collected from whole day 4 constructs using RNeasy Miniprep kit (Qiagen). cDNA was synthesized using iScript cDNA synthesis kit (Bio-Rad). Quantitative PCR was performed using Power SYBR Green PCR mix (Applied Biosystems) on a 7900HT Fast-Real-time PCR system (Applied Biosystems). Expression for each primer pair is quantified relative to HPRT. The following primer pairs (5' → 3') were used: *Fibronectin* (FN1; F-TGGCTGTCAGTCAAAGCAAG; R-CGCAGTTAAAACCTCGGCTT), *Type I collagen alpha 2* (Col1A2; F-CCTGGCAATATTGGTCCCGT; R-GATGTCCAGTGCGACCATCT), *Matrix metalloproteinase-2* (MMP2; F-ATAACCTGGATGCCGTCGT, R-AGGCACCCTTGAAGAAGTAGC), *Myosin heavy chain α subunit* (MHCα; F-CAAGTTGGAAGACGAGTGCT, R-ATGGGCCTCTTGTAGAGCTT), *Myosin heave*

chain β subunit (MHCβ; F-AGAACACCAGCCTCATCAAC, R-GCTCCTTCTTCAGCTCCTCT).

Appendix B.

List of supplemental video (SV) files:

SV1. Video of beating day 9 differentiated human stem cell-derived cardiomyocytes

SV2. Fluorescent Ca^{2+} transients of D14 hESC-CMs only constructs in 1.25mg/mL collagen

SV3. Fluorescent Ca^{2+} transients of D14 hESC-CMs only constructs in 6 mg/mL collagen

SV4. Fluorescent Ca^{2+} transients of D14 hESC-CMs + HS27a co-culture: 6 mg/mL collagen

SV5. Fluorescent Ca^{2+} transients of D14 co-cultured hESC-CMs+HS27a constructs with patterned microvessels.

SV6. Confocal z-stack of mTm engineered µV with interstitial GFP-hESC-ECs

SV7. Fluorescent bead perfusion of day 4 engineered microvessel

SV8. Whole blood perfusion through day 4 engineered microvessel

SV9. Whole blood perfusion through sprouting connection in day 4 engineered microvessel

SV10. CD41a-labeled platelets during whole blood perfusion of day 4 engineered microvessel

SV11. Cross sectional animation of OMAG flow overlaid with structural data: SA graft

SV12. Cross sectional animation of OMAG flow overlaid with structural data: µV + SA graft